Aus dem Bereich Physiologie
Theoretische Medizin und Biowissenschaften
der Medizinischen Fakultät
der Universität des Saarlandes, Homburg/Saar

GLIAL CA^{2+} SIGNALING IN THE SPINAL CORD AND THE MYELIN-PROTECTIVE EFFECT OF THE $GABA_B$ RECEPTOR IN OLIGODENDROCYTE PRECURSOR CELLS

DISSERTATION

ZUR ERLANGUNG DES GRADES EINES DOKTORS DER NATURWISSENSCHAFTEN

DER MEDIZINISCHEN FAKULTÄT
DER UNIVERSITÄT DES SAARLANDES

2023

vorgelegt von: Phillip Rieder
geboren am: 28. September 1990 in Pirmasens

Date of oral examination: **06. November 2023**

Dean of the faculty: **Univ.-Prof. Dr. med. Michael D. Menger**

1st reviewer: **Univ.-Prof. Dr. rer. nat. Frank Kirchhoff**

2nd reviewer: **Univ.-Prof. Dr. med. Frank Schmitz**

Hoc opus dedicatum est memoriae parentum.

TABLE OF CONTENTS

LIST OF ABBREVIATIONS

2P	2 Photon
(a)CSF	(artificial) cerebrospinal fluid
ADP	adenosine diphosphate
AQP4	aquaporin 4
ATP	adenosine triphosphate
Bp	base pair
BSA	bovine serum albumin
bw	body weight
cAMP	cyclic adenosine monophosphate
cKO	conditional knock out
CNS	central nervous system
Cre	Cre-DNA recombinase
ctl	control
DAPI	4′,6-Diamidin-2-phenylindol
DNA	deoxyribonucleic acid
dpi	days post injection
EDTA	ethylenediaminetetraacetic acid
ER	endoplasmic reticulum
ERT2	mutant human estrogen receptor ligand binding domain
fl	flanked by loxP sites (floxed)
FOV	field of view
GABA	γ-amino butyric acid
$GABA_BR$	$GABA_B$ receptor
GCaMP	GFP-calmodulin-M13 peptide fusion protein
GFP	green fluorescent protein
HBSS	Hank´s balanced sodium solution
HEPES	4-(2-hydroxyethyl)-1-piperazineethanesulfonic acid
i.p.	intraperitoneal
IHC	immunohistochemistry
IQR	interquartile range
KI	knock in
LoxP	locus of crossover of the bacteriophage P1
LSM	laser-scanning microscopy
mRNA	messenger ribonucleic acid
OL	oligodendrocyte lineage
OPC	oligodendrocyte precursor cell or NG2 glia (Neural/glial antigen 2)
p	p-value
PBS	phosphate-buffered saline
PCR	polymerase chain reaction
ROA	region of activity
RT	room temperature
SC	spinal cord
SEM	standard error of the mean
TAE	Tris-acetate-EDTA buffer
TAq	Thermophilus aquaticus
Tris	tris(hydroxymethyl)aminoethane
UV	ultraviolet light
WPRE	woodchuck hepatitis Virus posttranscriptional regulatory element
wt	wild type

LIST OF FIGURES

LIST OF TABLES

LIST OF SUPPLEMENTARY MATERIALS

SUPPLEMENTARY FIGURES

SUPPLEMENTARY TABLES

1 ABSTRACT

The highly complex network of glial cells in the central nervous system relies intracellularly and intercellularly on multilayered communication through the secondary messenger Ca^{2+} and is fundamentally different in its characteristics from the communication system of neurons, which is more rapidly timed. The Ca^{2+}-based communication system is inherent in all glial cells, whether astroglia, microglia, or the cells of oligodendroglial lineage. Eech cell receives, processes, and sends signals through Ca^{2+} concentration changes and, embedded in a syncytium of cells, provides information about its activity. If a cellular stress response occurs, Ca^{2+} concentration is an important indicator of the switch in cellular function, from gene activity to protein turnover and integrity to targeted cell death. Such steps are cell type-specific and task-related, as well as controllable by surrounding cells or disease. This cellular Ca^{2+} activity can be visualized under cell type-specific promotors using the genetically encoded Ca^{2+} sensor GCaMP3 and has been comparatively analyzed in this study in spinal glial cells using two-photon microscopy *in vivo* and *ex vivo*.

In the development and maintenance of myelin by oligodendrocytes, finely tuned Ca^{2+} signals are crucial for functional myelin quality. These mature oligodendrocytes arise throughout life from their precursors, NG2 glia, also a sensitive Ca^{2+} dependent process. The inhibitory neurotransmitter γ-aminobutyric acid (GABA) has a depolarizing effect on these cells via its ionotropic receptor ($GABA_A$) on one hand and leads to an increase of intracellular Ca^{2+} via the metabotropic receptor ($GABA_B$), presumably involving G proteins and phospholipase C, on the other hand. Already in clinical therapy of spasticity in multiple sclerosis, receptor agonists against GABA receptors are used to provide relief to patients. Conditional receptor loss in oligodendroglial precursor cells (OPCs) and its effect on Ca^{2+} homeostasis, as well as its combination with a toxic demyelination model by a cuprizone diet, were investigated in mouse spinal cord in this study. Because the peripheral arrangement of lipid-rich white matter in the spinal cord is readily accessible, two-photon microscopy *in vivo* was used.

This study revealed cell type-specific and regionally dependent Ca^{2+} activity for microglia, astroglia as well as oligodendroglial precursor cells. Furthermore, loss of the metabotropic $GABA_B$ receptor in oligodendroglial precursor cells showed reduced Ca^{2+} activity and altered myelin structure and, at a later time point, a myelin protective effect with hardly altered Ca^{2+} signaling activity after toxic demyelination.

2 ZUSAMMENFASSUNG

Das hoch komplexe Netzwerk aus Gliazellen im Zentralnervensystem stützt sich intra- und interzellulär auf die vielschichtige Kommunikation durch den sekundären Botenstoff Ca^{2+} und ist grundlegend anders in seiner Charakteristik als das Kommunikationssystem der Neurone, das zeitlich schneller getaktet ist. Die auf Ca^{2+} basierende Kommunikation ist allen Gliazellen eigen, ob Astroglia, Mikroglia oder Zellen der oligodendroglialen Linie. Jede dieser Zellen erhält, verarbeitet und sendet durch Ca^{2+} Konzentrationsänderungen Signale aus und gibt, eingebettet in einem Synzytium aus Zellen, Aufschluss über seine Aktivität. Kommt es zur zellulären Stressantwort ist die Ca^{2+} Konzentration ein wichtiger Indikator für die Umstellung der Zellfunktionen, von der Genaktivität über den Proteinumsatz und -integrität bis hin zum gezielten Zelltod. Solche Schritte sind zelltypspezifisch und aufgabenbezogen sowie durch umliegende Zellen oder Krankheiten manipulierbar. Diese zelleigene Ca^{2+} Aktivität kann unter zelltypspezifischen Promotoren mittels dem genetisch kodierten Kalziumsensor GCaMP3 visualisiert werden und ist in dieser Studie in spinalen Gliazellen mittels Zwei-Photonen Mikroskopie *in vivo* und *ex vivo* vergleichend analysiert worden.

Bei der Entwicklung und Aufrechterhaltung des Myelins durch Oligodendrozyten sind fein abgestimmte Ca^{2+} Signale ausschlaggebend für funktionales Myelin. Reife Oligodendrozyten entstehen zeitlebens aus ihren Vorläufern, den NG2-Glia unter anderem durch einen sensiblen, Ca^{2+} abhängigen Prozess. Der inhibitorische Neurotransmitter γ-Aminobuttersäure (GABA) wirkt an diesen Zellen zum einen depolarisierend über seinen ionotropen Rezeptor ($GABA_A$) und zum anderen positiv auf die Erhöhung des intrazellulären Ca^{2+} über den metabotropen Rezeptor ($GABA_B$), vermutlich G-Proteine und Phospholipase C involvierend. Bereits in der klinischen Therapie von Spastiken bei Multipler Sklerose werden Agonisten gegen GABA Rezeptoren eingesetzt um den Patienten Linderung zu verschaffen. Der konditionelle Rezeptorverlust in oligodendroglialen Vorläuferzellen und dessen Auswirkung auf die Ca^{2+} Homöostase, sowie dessen Kombination mit einem toxischen Demyelinisierungsmodell durch eine Cuprizon Diät wurden in dieser Studie im Rückenmark von Mäusen untersucht. Da die periphere Anordnung der lipidreichen weißen Substanz im Rückenmark leicht zugänglich ist, konnte hier ebenfalls die Zwei-Photonen Mikroskopie *in vivo* eingesetzt werden.

In dieser Studie zeigten sich zelltypspezifische und für Mikro- und Astroglia sowie oligodendrogliale Vorläuferzellen regional abhängige Ca^{2+} Aktivitäten. Des Weiteren führte der Verlust des metabotropen $GABA_B$ Rezeptors in oligodendroglialen Vorläuferzellen zu einer reduzierten Ca^{2+} Aktivität und veränderter Myelin Struktur sowie zu einem späteren Untersuchungszeitpunkt zu einem Myelin protektiven Effekt mit kaum veränderter Ca^{2+} Signalaktivität nach toxischer Demyelinisierung.

3 INTRODUCTION

Our human central nervous system from brain to spinal cord consists mainly of two classes of cell types and is composed of approximately equal proportions of about 86 billion neurons and glial cells. While neurons transmit stimuli and information via fast electrical action potentials, for glial cells it is mainly a comparatively slower change in the intracellular Ca^{2+} level that enables information transmission. This dissertation is mainly concerned with spinal glial cells and their Ca^{2+} activity in physiology and pathophysiology.

3.1 INTRACELLULAR CA^{2+}: A KEY READ-OUT OF GLIAL CELL ACTIVITY

Variations in intracellular Ca^{2+} concentration are considered to be one of the most important and elaborate signaling pathways in glial cells. These changes can be triggered by various pathways, e.g. electrical, mechanical or chemical stimuli (e.g. involving neurotransmitters and neuromodulators or hormones) leading to intricate alterations of cytosolic Ca^{2+} concentrations mainly store-dependent from the endoplasmic reticulum (Charles et al., 1991; Clapham, 2007; Bagur and Hajnóczky, 2017). The impulse of these Ca^{2+} changes can be of intracellular and extracellular origin and involves a variety of receptors and Ca^{2+} permeable channels. It was recognized early on and is still valid that the manifold temporal and spatial manifestations of Ca^{2+} complexity are the basis for a sophisticated information system including downstream activity of protein kinases, phospholipases up to gene expression regulation, cell metabolism and development (**Figure 1**) (Finkbeiner, 1993; Berridge, 2016) and that underlying Ca^{2+} fluctuation varies in strength across glial cells (Rieder et al., 2022).

A signal information is first encoded than subsequently processed and transmitted through the glial network and can be influenced and or triggered by bidirectional communication with neuronal activity (Charles, 1994; Verkhratsky and Kettenmann, 1996; Deitmer et al., 1998). It is therefore considered a translation system between extracellular milieu and intracellular processes (Verkhratsky and Parpura, 2014); especially to detect and respond to synaptic activity (Araque and Navarrete, 2010; Perea et al., 2014). However, these changes in Ca^{2+} concentration are not to be understood as purely passive, but rather as a form of glial excitability, an active mechanism in the interaction between cells within brain and spinal cord (Verkhratsky and Kettenmann, 1996; Vernadakis, 1996; Bazargani and Attwell, 2016). Versatile actions of Ca^{2+}-dependent channels and receptors on glial cells have been identified as associated proteins responsible for maintaining physiological homeostasis (e.g. plasma membrane Ca^{2+} transport ATPase (PMCA) and Na^{+}/Ca^{2+}

exchanger (NCX) for maintenance, sarcoendoplasmic reticulum Ca^{2+}-ATPase (SERCA) for remediation, inositol-1,4,5-triphosphate receptor (IP_3R), purinergic P2 (ATP) receptors, ryanodine receptor (RyR), voltage-gated Ca^{2+} channels (CaV), transient receptor potential channels (TRP) and Ca^{2+} release-activated channel (CRAC) (Bagur and Hajnóczky, 2017; Enders et al., 2020; Lim et al., 2021)). In most cases, the signaling cascade is mediated by Ca^{2+} or IP_3 and is transmitted, for example, in astrocytes within a syncytium by means of gap junctions (Berridge, 2016) but also other second messengers as cyclic ADP-ribose (cADPR) like cAMP and Nicotinic acid adenine dinucleotide phosphate (NAADP) which may be responsible for intracellular Ca^{2+} recruitment (Franco et al., 2006). Most of the signaling molecules that bind to the above-mentioned receptors and are mostly excitatory in origin have also been largely associated with astroglial Ca^{2+} homeostasis, gliotransmission and general Ca^{2+} elevations in the forebrain (Guerra-Gomes et al., 2017). This includes the excitatory transmitters glutamate (Sherwood et al., 2017), ATP (Perea and Araque, 2007), acetylcholine (Papouin et al., 2017), endocannabinoids (Gómez-Gonzalo et al., 2015) but also the inhibitory neurotransmitter GABA (Serrano et al., 2006; Mariotti et al., 2016; Perea et al., 2016).

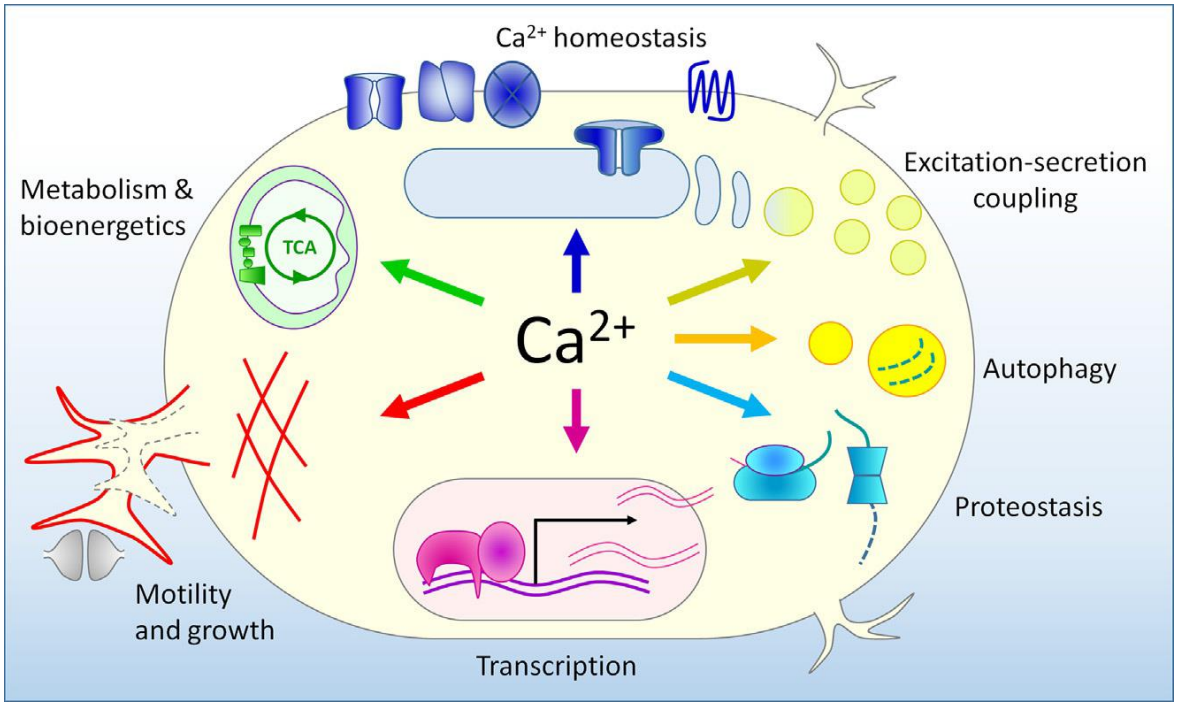

Figure 1: The impact of intracellular Ca^{2+} on glial cell function.

Intracellular Ca^{2+} and its homeostasis affect metabolism, motility, gene transcription, protein biosynthesis, autophagy, and extracellular signal transduction. Modified from (Lim et al., 2021).

If Ca^{2+} homeostasis is disturbed in a neurodegenerative disease, even small changes can lead to an accumulation of intracellular Ca^{2+}, resulting in severe cell dysfunction. Thus, fine-tuning of the Ca^{2+} balance for glial cells has a prominent role in the maintenance of molecular, cellular and systemic functions (Mizoguchi and Monji, 2017; Di Benedetto et al., 2022). The shift in neuro-/gliotransmitter recycling and altered release of gliotransmitters caused by disruption of the Ca^{2+} homeostasis leads to a wide variety of cellular changes. A resulting slightly changed or overdriven glutamate release leads to excitotoxicity, which has been demonstrated in neurodegenerative diseases such as Alzheimer's, Parkinson's or Huntington's disease and multiple sclerosis (Beal, 1992; Mattson, 2007; Pchitskaya et al., 2018; Enders et al., 2020). This also affects decreased ATP production, activation of reactive oxygen species and calmodulin-dependent kinases for nitric oxide production, all leading to neuronal cell death and gliosis (Beal, 1992; Pitt et al., 2000; Sattler and Tymianski, 2000; Szydlowska and Tymianski, 2010).

3.2 Ca^{2+} INDICATORS, THE TOOL OF CHOICE FOR *IN VIVO* STUDIES IN GLIAL CELLS

The complexity of glial Ca^{2+} signaling is summarized in detail and vividly in (Lim et al., 2021), and the clarification of the function of these signals by the scientific community in recent decades is discussed. The literature describes heterogeneous Ca^{2+} signals in the best-studied astrocytes, which are neuronally inducible, appear short and highly frequent in their processes and long-range but less frequent in their soma (Lia et al., 2021). The disposition of these signals is from the already known sources: the ER, the extracellular space or mitochondria. The Ca^{2+} signals of oligodendrocytes are much less characterized but also derived from extracellular or intracellular stores, whereas microglia express purinergic receptors and transient receptor potential channels and derive their potential to generate Ca^{2+} signals from the ER, respectively (Lim et al., 2021).

To be able to study this complexity in living tissue including network and single cell activity, genetically encoded Ca^{2+} indicators (GECIs) are the tool of choice. GCaMP (**Figure 2**) has been widely used, although it is not a ratiometric Ca^{2+} indicator and thus does not provide direct information about Ca^{2+} concentrations by fluorescence intensity measurements. It is a fusion protein consisting of enhanced GFP bound to the Ca^{2+}-binding protein calmodulin and the calmodulin-binding M13 peptide, which undergoes a conformational change upon binding by Ca^{2+} ions, resulting in fluorescent emission (Nakai et al., 2001; Akerboom et al., 2009).

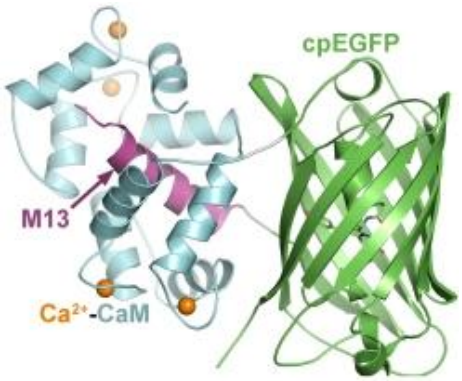

Figure 2: Crystal-like structure of the fusion protein GCaMP.

Fusion protein of circularly permuted enhanced GFP and calmodulin with the Ca^{2+} binding motif M13 as a crystallographic illustration. Modified from (Akerboom et al., 2009).

3.3 MULTIPLE SCLEROSIS AND THE ASSOCIATED ROLE OF GLIAL CELLS

Multiple sclerosis (MS) is a progressively worsening neurodegenerative disease affecting prevalently young adults, in which oligodendrocytes and neuronal axons die and symptoms alternate in severity. In recent years, there has been a deeper understanding of the cellular and molecular background of MS, which is mainly caused by an exaggerated immune response. And this hallmark of MS is recurrent progression with expansion of lesions in the white matter, leading to infiltration of peripheral immune cells and gliosis (Healy et al., 2022). It has been debated for years whether a primary loss of oligodendrocytes and loss of myelin triggers a secondary immune response or whether the mechanism behind the disease is a primary, exaggerated immune response which is causing the demyelination (Lubetzki and Stankoff, 2014). Nevertheless, in the alternating phases of MS and the appearing lesions in the white matter, a rupture of the blood-brain barrier leads to a facilitated entry of B and T cells into the CNS, myelin degeneration and a death of oligodendrocytes, culminating in the loss of axons (Saxena et al., 2008; Lassmann, 2018). A MS lesion in its early stage is characterized by an accumulation of microglia and macrophages that contain myelin degradation products, the proteins 2',3'-Cyclic nucleotide 3'-phosphodiesterase (CNP), myelin-associated glycoprotein (MAG), myelin-basic protein (MBP) and proteolipid protein (PLP) (Kuhlmann et al., 2017). This state may change to an inactive mode characterized by fewer immune cells but more dead oligodendrocytes and axon loss (Guerrero and Sicotte, 2020). In addition to the microglial response, there is a change in astrocytes in the area of the MS lesion to a hypertrophic morphology with overexpression of glial fibrillary acidic protein (GFAP) and chemokines that should drive remyelination but are responsible for the well-known glial scar in inactive lesion. (Rawji et al., 2020). For the oligodendrocytes mainly involved in myelin formation and their

precursors, the oligodendrocyte precursor cells (OPCs) also referred to as NG2 glia, a certain fluctuation by apoptosis is already known and very important for neuronal plasticity, as well as lifelong learning (McTigue and Tripathi, 2008; McKenzie et al., 2014; Sampaio-Baptista and Johansen-Berg, 2017; Kuhn et al., 2019). However, the oligodendrocyte lineage is particularly vulnerable to oxidative stress, glutamate and ATP-induced excitotoxicity or injury, especially during the myelination process (Matute et al., 1997; Juurlink et al., 1998; Matute et al., 2007). So, it stands to reason that the loss of myelin that occurs during MS is associated with the death of oligodendrocytes and, in the case of demyelination in this clinical picture, is immune-driven (Love, 2006; Traka et al., 2016). Thus, if myelin sheath death results in exposed axons and subsequent neurodegeneration (Bradl and Lassmann, 2010; Duncan and Radcliff, 2016), OPCs, which make up 6 % of the cell population in the central nervous system (Dawson et al., 2003), serve as a starting point for remyelination and the formation of new, mature oligodendrocytes (Hesp et al., 2015). The exact mechanism underlying the replacement of myelin in the case of previous demyelination is not yet fully understood. However, some key points are already known. After demyelination, OPCs are guided to migrate into the white matter lesion by microglia and astrocytes releasing fibroblast growth factor and brain-derived neurotrophic factor (Arai and Lo, 2009; Hammond et al., 2014). OPCs, expressing transcription factors such as SOX2, thus remain capable of proliferation, driven by microglia, are activated in their cell cycle leading to maturation into oligodendrocytes, which are initially only capable of forming thinner myelin sheaths (Blakemore, 1974; Casaccia-Bonnefil et al., 1997; Levine and Reynolds, 1999; Fancy et al., 2004; Miron et al., 2013; Franklin and Ffrench-Constant, 2017). However, remyelination, important for combating MS symptoms, is not only dependent on OPCs; surviving oligodendrocytes are also able to compensate for the loss of myelin (Duncan et al., 2018; Yeung et al., 2019). The major problem, remains the recruitment of OPCs to proliferate into mature oligodendrocytes, which has been demonstrated to a high degree in the active lesion but does not occur adequately in the inactive, chronic lesions (Chang et al., 2002; Kuhlmann et al., 2008).

3.4 EPIDEMIOLOGY, ETIOLOGY AND CLINICAL INSIGHTS INTO MULTIPLE SCLEROSIS

The important triggers for the development of multiple sclerosis (MS), a growing global disease (Browne et al., 2014), are now reasonably well known, including the Epstein-Barr virus, smoking, vitamin D deficiency, UVB light from the sun and personal genetic risk factors and can be negatively favored by environmental influences (Ramagopalan et al., 2010; Kurtzke, 2013). As latitude increases, so does the prevalence of MS. This has been

shown by measurements of vitamin D levels produced in the skin by UVB light and is dependent on the sun exposure of the population (Koch-Henriksen and Sørensen, 2010; Sintzel et al., 2018). Since the 1990s, the number of women with MS has increased substantially compared with men, by a factor of 3:1 (Orton et al., 2006). Another facilitating factor is smoking, which has increased sharply in women over the last century, and the organic ingredients of tobacco smoke appear to support post-translational modifications and the development of MS (Handel et al., 2011; Palacios et al., 2011; Napier et al., 2016). Genetic predisposition also appears to contribute to the disease development, with one in eight patients having a family history of MS and genome-wide studies showed more than 150 single nucleotide polymorphisms associated with MS (Beecham et al., 2013; Harirchian et al., 2018).

Classical for the pathology are the perivenular inflammatory lesions and the thereby clinically relevant demyelinating plaques (Dobson and Giovannoni, 2019). The expression of these plaques or white matter lesions is important and valuable for diagnosis, as they lead to clinically and radiologically isolated syndromes of acute disseminated encephalomyelitis (ADEM) (Karussis, 2014). Only by appropriate treatment of the syndromes and classification of MS based on immunological biomarkers, a targeted therapy can be successfully initiated since patients' daily lives are severely affected by sensory disturbance or tingling in the legs or arms, severe fatigue and rapid exhaustion, problems with bowel or bladder emptying, ataxia, visual disturbances and paresis.

3.5 CUPRIZONE: AN ANIMAL MODEL FOR DEMYELINATION

The cuprizone model, which is a toxin-induced model of demyelination by the copper chelator cuprizone (biscyclohexanone oxalyldihydrazone), leads to apoptosis of oligodendrocytes (**Figure 3**) and subsequent activation and recruitment of innate immune cells (microglia and astrocytes) as well as damage to the blood-brain barrier within a few days after oral ingestion (Kipp et al., 2009; Praet et al., 2014; Berghoff et al., 2017). With the help of this model, the characteristic progressive course of multiple sclerosis can be reproduced very well. This allows the study of two major components of the disease, namely the cellular response of immune-associated cells such as astrocytes and microglia, leading to myelin and axon loss (1), and the remyelination of axons and the role of oligodendrocyte lineage cells involved (2; (Zhan et al., 2020)). It has been known since the 1960s that cuprizone fed as a diet leads to demyelination in mice (Carlton, 1966). In most cases, a concentration of 0.2 % was added to the diet for four to six weeks (Hiremath et al., 1998). In our case, a modified protocol was used in which 0.3 % was first fed as a diet for one

week and then 0.2 % was fed as a diet for two weeks in the form of powdered chow, after which we returned to normal pellet chow. Already in the first days, the high affinity of cuprizone for copper, a metabolic cofactor of oxidative phosphorylation in mitochondria, leads to the targeted death of myelinating oligodendrocytes (**Figure 3**) due to their high metabolic rate (Bradl and Lassmann, 2010; Bénardais et al., 2013). The first modifications of gene regulation have also been detected after only a few days of intoxication. Thus, already 48 hours after onset, 22 of the top 25 downregulated mRNAs were found expressed in oligodendrocytes (e.g. *Mog*, *Klk6*, *Gjc*). In contrast, the top 25 upregulated mRNAs were associated with astrocytes and microglia (e.g. *Slc7a11*, *Myc*) (Zhang et al., 2014; Krauspe et al., 2015; Fischbach et al., 2019). During the three-week diet, myelin loss (PLP, MAG and CNPase protein level reduction), as well as strong astro- and microglial reactivity (GFAP and Iba1 protein upregulation) in the different areas of the central nervous system (Zhan et al., 2020), and weight loss in the animals occur (Steelman et al., 2012; Toomey et al., 2021). Although forebrain regions are more affected by cuprizone, only a diminished response was detected in the spinal cord so far (Herder et al., 2011).

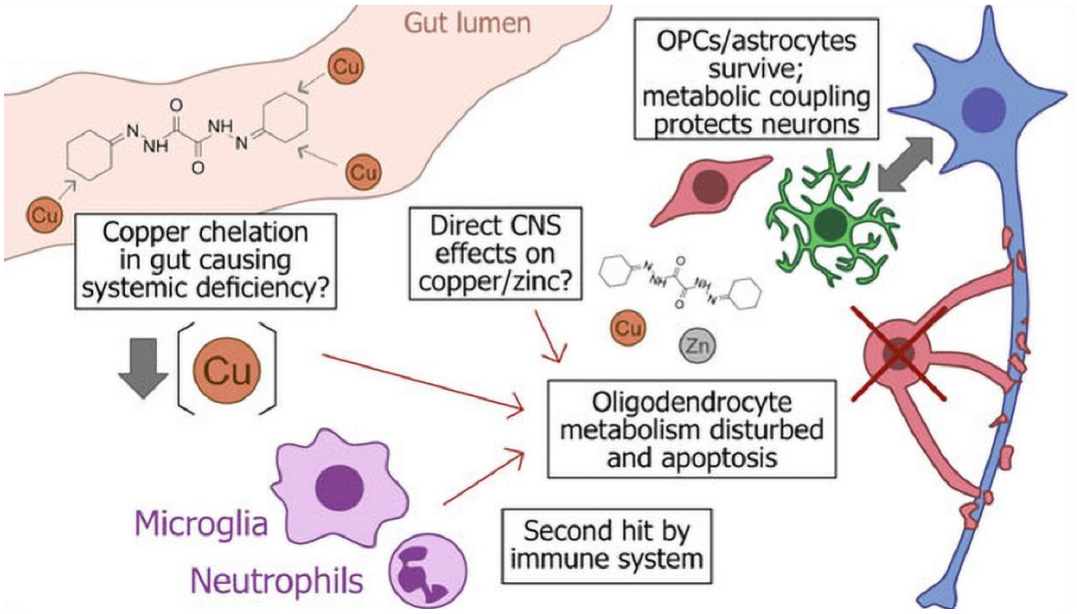

Figure 3: Mechanism of action of the demyelinating cuprizone model.

Enteral ingestion causes a direct system-wide failure of oligodendroglial metabolism, causing them to die. Secondary reaction results in the recruitment of cells from the immune system. Modified from (McMurran et al., 2019).

3.6 Ca^{2+} AND FATE OF THE OLIGODENDROCYTE LINEAGE, THE NEW TARGET TO UNDERSTAND MULTIPLE SCLEROSIS?

The most important function of oligodendrocytes to date is their ability to produce myelin (**Figure 4**). This is achieved by the production of multilayered lipid sheets that surround the axons, providing metabolic support, and thus guarantee highly efficient and ultrafast saltatory excitation conduction (Moore et al., 2020).

But what happens in a demyelinating disease? Are there signs of cell signaling processes that may already be disturbed before the manifestation of disease symptoms? To answer this, one must understand how mature myelinating oligodendrocytes are generated and what the cell signals involved in their important function are.

The possibility of transforming mature oligodendrocytes from oligodendrocyte precursor cells (OPCs/NG2 glia; 3-10 % of all cells in the central nervous system (Stadelmann et al., 2019)) originating from the ventricular zone of the central nervous system into the adjacent areas (Richardson et al., 2006), from child- to adulthood is the target of many studies dealing with de- and remyelination (**Figure 4**). As a specialty in differentiation in the spinal cord, OPCs generating from a second wave transdifferentiate to radial glia. Then serving as a pool for astrocytes from the central canal to the pia, some of them remain as OPCs and express typical markers such as oligodendrocyte transcription factor (Olig2), Sox10 and platelet-derived growth factor receptor α (PDGFRα; (Fogarty et al., 2005; Bergles and Richardson, 2016; Huang et al., 2018). This transformation and lineage are manifold regulated; intracellular transcriptional variations by chromatin and histone modifications, as well as differentially influenced RNA activity, are important (Emery, 2010; Emery and Lu, 2015; Galloway and Moore, 2016; Berry et al., 2020). But also the function and maintenance of the extracellular milieu seems to be crucial for a smooth transformation and differentiation during remyelination (Wheeler and Fuss, 2016).

The countless roles, origins, and signaling pathways of Ca^{2+} for a cell are also reflected in OPCs. OPCs form glutamatergic and GABAergic synaptic connections with neurons in the white and gray matter (**Figure 5**) (Bergles et al., 2000; Lin and Bergles, 2004; Kukley et al., 2007; Ziskin et al., 2007; Gallo et al., 2008; Bergles and Richardson, 2015; Zonouzi et al., 2015), which is especially interesting because both lead to increased intracellular Ca^{2+} in OPCs (Káradóttir and Attwell, 2007; Tanaka et al., 2009). The synaptic interplay is underpinned by the fact that OPCs primarily express postsynaptic proteins (Zhang et al., 2014), yet these are down-regulated with development toward the oligodendrocyte but it is also clear that Ca^{2+} activity is regulating myelination (**Figure 5**) (De Biase et al., 2011; Miller, 2018). The neuronal influence and thereby shifts in the intracellular Ca^{2+} of OPCs may

regulate proliferation in a subset of them (Marisca et al., 2020). The importance of Ca^{2+} for the maintenance or degradation of freshly built myelin and in particular how this is controlled in microdomains and influenced by neuronal activity *in vivo* is a promising approach to the molecular control of myelination (Baraban et al., 2018; Krasnow et al., 2018).

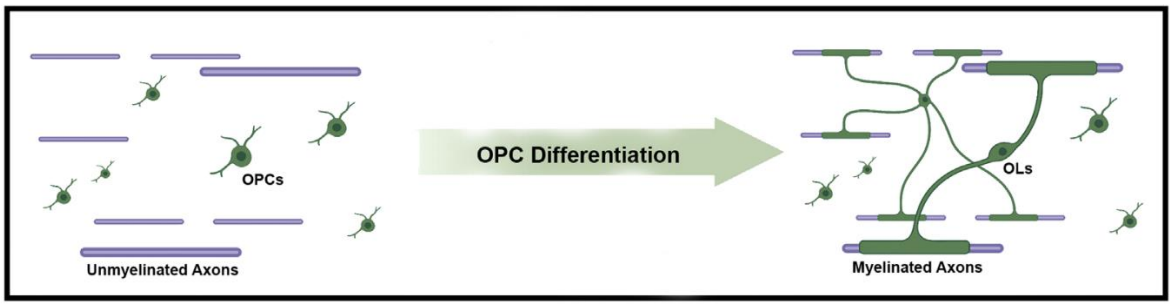

Figure 4: Oligodendroglial differentiation physiology.

From unmyelinated axons to myelinated axons for physiological stimulus transmission, oligodendroglial precursor cells must differentiate into mature, myelinating oligodendrocytes that coat multiple axons in a multilayered manner. In addition, precursor cells remain as a reserve throughout life. Modified from (Clayton and Tesar, 2021).

The highly developed and excellently tuned regulation of intracellular Ca^{2+} makes it all the more susceptible to pathologies and out balanced can lead to the exacerbation of pathologies. Thus, specifically concerning demyelination, it was discovered that the breakdown of myelin structures is related to Ca^{2+} dysregulation and promotes its vesicularization; in the case of a neuromyelitis model, increased Ca^{2+} concentration breaks down the polymer structure of myelin basic proteins (Weil et al., 2016). In the context of neonatal hypoxia and concomitant dysregulation of OPC proliferation (Salmaso et al., 2014), this has been associated mainly with GABAergic signaling, which is Ca^{2+} regulated as previously described (Zonouzi et al., 2015).

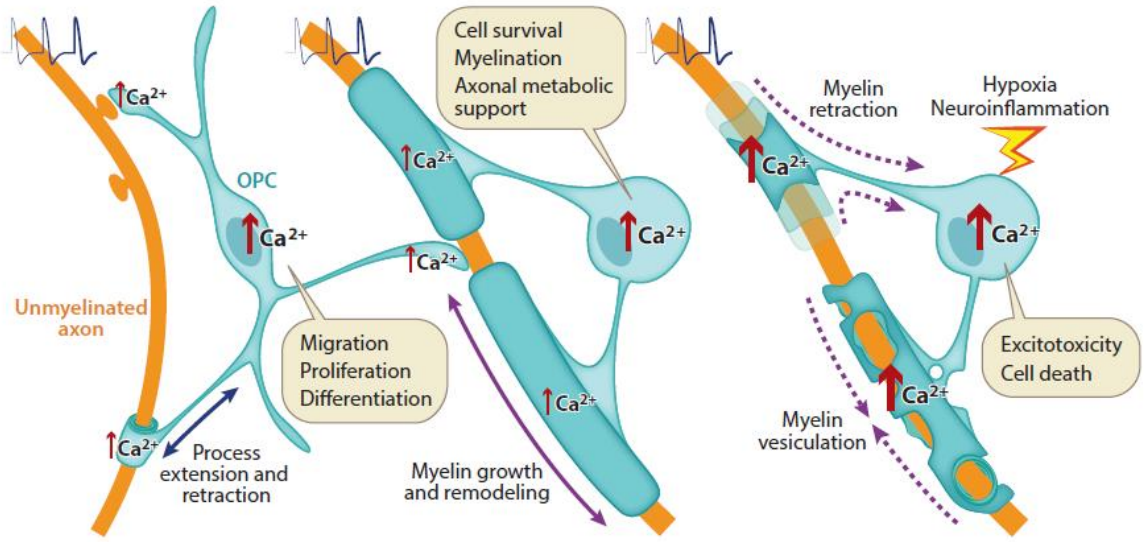

Figure 5: The influence of Ca^{2+} during the development of oligodendroglial precursor cells into oligodendrocytes and during demyelination.

Balanced and nuanced Ca^{2+} is essential for synaptic activity, migration, proliferation and differentiation towards the myelinating oligodendrocyte and its unrestricted, healthy and axon metabolically supporting existence. In case of hypoxia or neuroinflammation, unbalanced Ca^{2+} becomes toxic and leads to apoptosis. Modified from (Paez and Lyons, 2020).

The functional presence of the ionotropic $GABA_A$ receptor in cells of the oligodendrocyte lineage has been known since the 1980s (Gilbert et al., 1984) and its activation leads to depolarization by Cl^- efflux, shown in mouse hippocampal slices (Von Blankenfeld et al., 1991; Berger et al., 1992; Steinhäuser et al., 1994). Furthermore, expression of the metabotropic $GABA_B$ receptor with its two subunits B1 and B2 was detected in the oligodendrocyte lineage already from the stage of the precursor cells (Calver et al., 2000; Zhang et al., 2014; Serrano-Regal et al., 2019). And $GABA_B$ receptor activation performed with the agonist baclofen leads to increased proliferation of OPCs in culture (Luyt et al., 2007), as well as a myelin protective effect in the lysolecithin model for demyelination *in vivo* (Serrano-Regal et al., 2022). Promisingly, $GABA_B$ receptor activated lowering of intracellular cAMP in OPCs and reduced protein kinase A activity leads to the remaining question in how far downstream $G_{i/o}$ or G_q are involved in the signaling pathways of cAMP and Ca^{2+} (Luyt et al., 2007; Bai et al., 2021).

4 AIMS OF THE STUDY

Cell-cell communication is one of the first interfaces in physiology to change and is plastically modulated in the event of disease. It is therefore all the more important to understand glial cell functions, which regulate their own cell activity and those of their surrounding cells almost exclusively via the second messenger Ca^{2+}. Especially the cells of the spinal cord, a high-performance connection between brain and periphery, are significantly affected by demyelination. Evidence for the influence on myelination by modification of the metabotropic $GABA_B$ receptor in oligodendroglial precursor cells in combination with intracellular Ca^{2+} could be key players in the understanding of multifactorial degenerative diseases. Therefore, using transgenic mouse lines to visualize intracellular Ca^{2+} and receptor loss, physiological and pathophysiological conditions (by toxic demyelination) in Ca^{2+} variations and cell changes will be investigated here to answer the following three main questions:

- **How do spinal glial cells differ in their temporal and spatial Ca^{2+} signaling properties?**
  To be achieved by: *In vivo* and *ex vivo* two-photon laser-scanning microscopy of GCaMP3 expressing astrocytes, microglia and oligodendrocyte precursor cells using a novel software tool.

- **Does the $GABA_B$ receptor loss influence Ca^{2+} signaling parameters and cell fate in oligodendrocyte precursor cells?**
  To be reached through: $GABA_B$ receptor loss in oligodendrocyte precursor cells *in vivo* combined with live Ca^{2+} imaging and final immunohistochemical analysis of cell, myelin and proliferation markers.

- **Do Ca^{2+} signaling characteristics in oligodendrocyte precursor cells change after toxic demyelination by cuprizone and how could this be influenced by a $GABA_B$ receptor deficit?**
  To access through: Analyzing *in vivo* Ca^{2+} recordings in oligodendrocyte precursor cells with $GABA_B$ receptor loss after toxic demyelination by cuprizone.

5 MATERIALS AND METHODS

5.1 MATERIALS

5.1.1 CHEMICALS, CONSUMABLES & KITS

Standard chemicals were obtained from manufacturers like Abcam (Cambridge, United Kingdom), Axon Labortechnik (Kaiserslautern, Germany), Bio-Rad (Hercules, USA), Biozol (Eching, Germany), Carl Roth (Karlsruhe, Germany), Eppendorf (Hamburg, Germany), Merck (Darmstadt, Germany), Millipore (Burlington, USA), R&D Systems (Minneapolis, USA), Roche (Basel, Switzerland), Sigma-Aldrich (St. Louis, USA), Thermo Fisher Scientific (Waltham, USA).

Consumables and kits have been supplied as standard by suppliers such as B. Braun (Melsungen, Germany), Greiner Bio-One (Frickenhausen, Germany), Qiagen (Hilden, Germany), Sarstedt (Nümbrecht, Germany), VWR International (Radnor, USA).

Utensils from further providers are mentioned at the respective place where they were used.

5.1.2 BUFFERS & AQUEOUS SOLUTIONS

The following listed solutions were prepared with deionized and RNAse-free H_2O from an ultrapure water system Milli-Q (Merck; Darmstadt, Germany) and used in the indicated concentration to perform the experiments: 10x PBS (1.37 M NaCl; 27 mM KCl; 100 mM Na_2HPO_4; 18 mM KH_2PO_4 (pH 7.4)) for dilution and washing steps (1x), Formaldehyde in 0.1 M PB (4 % (v/v) Paraformaldehyde; 0.2 M NaH_2PO_4; 0.2 M Na_2HPO_4; a few drops of 10 M NaOH to dissolve PFA (pH 7.4)) was used for transcardial perfusion, 50x TAE (1 M Tris-Base; 1 mM Acetic Acid; 1 mM EDTA (pH 8)) as buffer for gel electrophoresis (1x), DNA extraction solution (0.25 KCl; 0.01 M EDTA; 0.1 M Tris-HCl (pH 9.5)) and neutralization solution (3 % BSA; 10 ppm Kathon) for genotyping, spinal cord buffer (125 mM NaCl; 5 mM KCl; 10 mM Glucose; 10 mM HEPES; 2 mM $CaCl_2$; 2 mM $MgSO_4$ (pH 7.4)) for *in vivo* surgeries, aCSF (118 mM NaCl; 3 mM KCl; 1 mM NaH_2PO_4 x $2H_2O$; 25 mM $NaHCO_3$; 30 mM Glucose; 1 mM $MgCl_2$; 1.5 mM $CaCl_2$ (pH 7.4)) for acute slice preparation, blocking/first antibody permeabilization buffer (5 % horse serum; 0.3 % Triton-X-100) and secondary antibody buffer (5 % horse serum) in 1x PBS for immunohistochemical staining.

5.1.3 DEVICES

All experiments were carried out using the following equipment: AxioScan.Z1 (Zeiss; Oberkochen, Germany), Centrifuges (Eppendorf; Hamburg, Germany), cLSM 880 (Zeiss; Oberkochen, Germany), Isoflurane vaporizer (Harvard Apparatus; Holliston, USA), peqSTAR Thermo Cycler (peqlab Biotechnologie; Erlangen, Germany), Perfusion pump (Pharmacia Biotech; Uppsala, Sweden), Pipettes (Brand; Wertheim, Germany), Quantum gel documentation system (peqlab Biotechnologie; Erlangen, Germany), Scales CPA 8201/CPA 2245 (Sartorius; Göttingen, Germany), Shaker DRS-12 (neoLab; Heidelberg, Germany), Surgical instruments (Fine Science Tools; Heidelberg, Germany), Vibratome VT1000S/VT1200S (Leica; Wetzlar, Germany).

5.1.4 ENZYMES

REDTaq™ DNA Polymerase was purchased from Sigma-Aldrich (St. Louis, USA) and DreamTag™ Hot Start Green DNA Polymerase from Thermo Fisher Scientific (Waltham, USA) for DNA amplification during genotyping.

5.1.5 DRUGS AND DYES

Specific pharmaceuticals were used in the indicated concentrations: 10 mg/ml Tamoxifen (Caesar & Loretz; Hilden, Germany) in Miglyol for induction of a time-dependent reporter and cKO expression, 100 mg/ml Ketaminhydrochlorid (Serumwerk Bernburg; Bernburg, Germany) and 20 mg/ml Xylazinhydrochlorid (WDT; Garbsen, Germany) as lethal anesthesia for transcardial perfusion, Isoflurane (cp-pharma; Burgdorf, Germany), Bis(cyclohexanone)oxaldihydrazone ((Cuprizone) Carbolution Chemicals; St. Ingbert, Germany), 0.025 µg/ml 4’,6-Diamidin-2-phenylindol ((DAPI) Sigma-Aldrich; St. Louis, USA), 0.015 % Ethidum bromide (Carl Roth; Karlsruhe, Germany) and Easy ladder (Meridian Life Science; Memphis, USA).

5.1.6 ANTIBODIES

Table 1: Antibodies for immunohistochemistry.

Primary antibodies					
Antigen		**Clonality**	**Host**	**Dilution**	**Manufacturer**
GFAP	Glial fibrillary acidic protein	polyclonal	goat	1:1000	Abcam
GFP	Green fluorescent protein	polyclonal	chicken	1:1000	Thermo Fisher Scientific
Iba1	Ionized calcium-binding adapter molecule 1	polyclonal	goat	1:1000	Abcam
Ki67		monoclonal	rat	1:500	Thermo Fisher Scientific
MBP	Myelin basic protein	monoclonal	mouse	1:500	Biolegend
MyRF	Myelin regulatory factor	polyclonal	rabbit	1:500	Lab of Prof. Mengsheng Qiu (China)
NF	Neurofilament	polyclonal	chicken	1:500	Abcam
Olig2	Oligodendrocyte transcription factor	polyclonal	rabbit	1:1000	Millipore
PDGFRα	Platelet-derived growth factor receptor alpha	polyclonal	goat	1:1000	R&D Systems
Secondary antibodies					
Target		**Conjugation**	**Host**	**Dilution**	**Manufacturer**
anti-mouse		Alexa555	donkey	1:2000	Thermo Fisher Scientific
anti-rabbit		Alexa750		1:1000	
anti-chicken		Alexa488		1:1000	
anti-goat		Alexa647		1:1000	
anti-goat		Alexa555		1:2000	
anti-rat		Cy5		1:1000	Biozol

5.1.7 GENOTYPING PRIMERS

Table 2: Oligonucleotides for genotyping PCR.

Name	Serial number	Sequence	Amplicon (bp)
$GFAP^{CreERT2}$ forward	4750	5‘-CAGGTTGGAGAGGAGACGCATCA-3‘	WT 700
$GFAP^{CreERT2}$ reverse	7963	5’-CGTTGCATCGACCGGTAATGCAGGC-3’	TG 500
$CX_3CR_1^{CreERT2}$ forward (WT)	CXCT R2 (neu)	5’-ATCAACGTTTTGTTTTCGGA-3’	
$CX_3CR_1^{CreERT2}$ forward (WT)	5927	5‘-TCAGTGTTTTCTCCCGCTTGC-3’	WT 410
$CX_3CR_1^{CreERT2}$ reverse (KI)	5929	5‘-CAGTGATGCTCTTGGGCTTCC-3’	KI 380
$NG2^{CreERT2}$ forward (WT)	19398	5’-GGCAAACCCAGAGCCCTGCC-3’	
$NG2^{CreERT2}$ reverse (WT)	19399	5’-GCTGGAGCTGACAGCGGGTG-3’	KI 829
$NG2^{CreERT2}$ reverse (KI)	19400	5’-GCCCGGACCGACGATGAAGC-3’	WT 557
$GABA_B$ forward	24391	5'-TGGGGTGTGTCCTACATGCAGCGGACGG-3'	KI 742
$GABA_B$ reverse	24392	5'-GCTCTTCACCTTTCAACCCAGCCTCAGGCAGGC-3'	WT 526
GCaMP3 forward (KI)	27632	5'-CACGTGATGACAAACCTTGG-3'	
GCaMP3 reverse (KI)	27496	5'-GGCATTAAAGCAGCGTATCC-3'	WT 327
GCaMP3 forward (WT)	14025	5'-CTCTGCTGCCTCCTGGCTTCT-3'	KI 245
GCaMP3 reverse (WT)	14026	5'-CGAGGCGGATCACAAGCAATA-3'	

5.1.8 REAL-TIME PCR PRIMERS

Table 3: Oligonucleotides for quantitative RT-PCR.

Gene	Forward	Reverse
AQP4 (Aquaporin-4)	5'-CTTTCTGGAAGGCAGTCTCAG-3'	5'-CCACACCGAGCAAAACAAAGAT-3'
CSPG4 (Chondroitin sulfate proteoglycan)	5'-GGGCTGTGCTGTCTGTTGA-3'	5'-TGATTCCCTTCAGGTAAGGCA-3'
GABBR1 (Gamma-aminobutyric acid type B receptor subunit 1)	5'-CGAAGCATTTCCAACATGAC-3'	5'-CAAGGCCCAGATAGCATCATA-3'
ITGAM (Integrin alpha M)	5'-ATGGACGCTGATGGCAATACC-3'	5'-TCCCCATTCACGTCTCCCA-3'
PDGFRA (Platelet-derived growth factor receptor A)	5'-TCCTTCTACCACCTCAGCGAG-3'	5'-CCGGATGGTCACTCTTTAGGAAG-3'

5.2 METHODS

5.2.1 TRANSGENIC ANIMALS AND TAMOXIFEN TREATMENT

Experimental mice were housed in the associated animal facility (CIPMM, University of Saarland, Homburg) and administration of the animals was performed with PyRAT, a Python based Relational Animal Tracking software (Scionics Computer Innovation; Dresden, Germany). Humidity and temperature in the breeding and maintenance rooms of the animal facility were kept constant at 45–65 % and 20–24 °C and the facility was maintained under a 12 h light-dark cycle. All mice received food *ad libitum* ((standard autoclaved rodent diet) Ssniff Spezialdiäten; Soest, Germany) and autoclaved tap water.

Descriptions of used transgenic mouse lines are listed in **Table 4**. The Cre^{ERT2}-loxP system used here allows conditional deletion of target genes by DNA recombination mediated tamoxifen induction (Feil et al., 2009). hGFAP-Cre^{ERT2} mice (Hirrlinger et al., 2006), as well as knock-in CX_3CR_1-Cre^{ERT2} (Yona et al., 2013) and NG2-Cre^{ERT2} (Huang et al., 2014) mice were crossbred to floxed GCaMP3 reporter mice (Paukert et al., 2014). Additionally, NG2-Cre^{ERT2} mice were crossbred to floxed $GABA_B$ subunit 1 mice (Haller et al., 2004). For simplicity, the following designations were used for the individual mouse lines: $GFAP^{CreERT2}$ for astroglia, $CX_3CR_1^{CreERT2}$ for microglia, $NG2^{CreERT2}$ ctl for NG2 glia (OPC) and $NG2^{CreERT2}$ cKO for OPCs lacking $GABA_{B1}$. To induce GCaMP3 expression and a conditional inactivation of the $GABA_B$ Receptor, tamoxifen was administered intraperitoneally for three (five in case of cKO induction) consecutive days (once per day, 100 mg/kg body weight) (Jahn et al., 2018) at 10 weeks of age.

5.2.2 GENOTYPING

For obtaining genomic DNA by extraction, animal tissue from tail biopsy or ear punch samples were used and incubated for 10 min with 62.5 µl of extraction solution (in M: 0.25 KCl, 0.01 EDTA, 0.1 Tris-HCl (pH 9.5)). Then, the solution was incubated at 95ºC for 20 min in a water bath and last 50 µl of neutralization solution (containing 3 % BSA and 10 ppm Kathon) was added.

For genotyping by PCR, DNA samples were incubated with prepared sample buffer from REDextract-N-Amp PCR KIT (Sigma-Aldrich; St. Louis, USA) or DreamTaq™ Hot Start Green DNA Polymerase (Thermo Fisher Scientific; Waltham, USA) and specific oligonucleotide primers (**Table 2**). The reactions were run in 96-well plates in a Thermocycler with programs listed in **Table 5**. Following gel electrophoresis was run on 1-

2 % agarose gels including 0.015 % ethidium bromide for 30-45 min, subsequently exposed and documented with a Quantum Gel documentation system.

Table 4: Single transgenic mouse lines.

Mouse line	Short term	Description	Type	Reference
TgH(CX_3CR_1-CreERT2)	CXCT	Expression of inducible CreERT2 in microglia	Knock In	Yona et al., 2013
TgN(hGFAP-CreERT2)	GCTF	Expression of inducible CreERT2 in astrocytes	Over-expression	Hirrlinger et al., 2006
TgH(NG2-CreERT2)	NGCE	Expression of inducible CreERT2 in NG2 glia (OPCs)	Knock In	Huang et al., 2014
TgH(Rosa26-CAG-fl-stop-fl-GCaMP3-WPRE	GCaMP3	GCaMP3 expression after removal of stop cassette by cre recombinase	Knock In	Paukert et al., 2014
TgH($GABA_B$-floxed)	$GABA_B$	Inducible KO of $GABA_B$	Knock In	Haller et al., 2004

5.2.3 CUPRIZONE DIET

The animals were fed with Bis(cyclohexanone)oxaldihydrazone (Cuprizone) *ad libitum* for one week receiving a concentration of 0.3 % mixed with standard powder food and a concentration of 0.2 % for two following weeks, starting at 10 weeks of age. The diet included 4 % fine sugar (Südzucker; Mannheim, Germany) and was freshly prepared and changed every day. Animals' body weight was measured every second day monitoring the effectiveness of the diet. After three weeks of diet, animals were fed standard food again.

5.2.4 LAMINECTOMY AND SPINAL WINDOW IMPLANTATION

(Cartarozzi et al., 2018; Rieder et al., 2022)

All surgical procedures were conducted in animals receiving inhalational anesthesia (1.5-2 % isoflurane, 66 % O_2 and 33 % N_2O) via mask and the animal´s eyes were covered by Bepanthen™ (Bayer; Leverkusen, Germany). Operations were adapted and modified from (Fenrich et al., 2012; Cupido et al., 2014) to get access to T12-L2 vertebrae and by laminectomy approach T13-L1 spinal segments could be exposed. For chronic observations, a modified coverslip was implanted on the spinal cord and animals were postoperatively injected subcutaneously with analgesic and antiphlogistic agents for two consecutive days.

Table 5: Thermocycler programs for genotyping.

PCR	Step	Temperature (°C)	Time (min=`; s=``)
CXCT	1	94	3`
	2	94	30``
	3	52	30``
	4	72	1`
	5	repeat from step 1 for 29 times	
	6	72	10`
	7	10	forever
GCTF	1	94	3`
	2	94	30``
	3	60	30``
	4	72	1`
	5	repeat from step 1 for 34 times	
	6	72	10`
	7	10	forever
NGCE	1	95	3`
	2	60	30``
	3	72	1`
	4	95	30``
	5	repeat from step 1 for 35 times	
	6	60	30``
	7	72	5`
	8	10	forever
GCaMP3	1	94	3`
	2	94	30``
	3	58	30``
	4	72	30`
	5	repeat from step 1 for 34 times	
	6	72	10`
	7	10	forever
$GABA_B$	1	95	3`
	2	68	30``
	3	72	45``
	4	95	30`
	5	repeat from step 2 for 35 times	
	6	68	30`
	7	72	3`
	8	10	forever

5.2.5 ACUTE SPINAL CORD SLICE PREPARATION

(Rieder et al., 2022)

After cervical dislocation, spinal T13-L1 segments were dissected from the backbone and further processed in ice-cold artificial cerebrospinal fluid (aCSF: in mM, 125 NaCl, 2.5 KCl, 2 $CaCl_2$, 1 $MgCl_2$, 1.25 NaH_2PO_4, 25 $NaHCO_3$, and 25 D-glucose, 330 mOsm/l, pH 7.4; adapted from (Szoke et al., 2006)) and purged by carbogen. Afterwards, longitudinal sections were cut by a vibratome (VT1200 S) (Leica) with 250 µm thickness, primarily maintained at 37 °C for 30 min and subsequently stored at room temperature for further 30 min and during two-photon imaging.

5.2.6 TWO-PHOTON LASER-SCANNING MICROSCOPY

(Cartarozzi et al., 2018; Meyer et al., 2022; Rieder et al., 2022)

To perform *in vivo* and *ex vivo* recordings, a custom-made two-photon laser-scanning microscope (2P-LSM) setup, equipped with a mode-locked Ti:sapphire femto second pulsed laser, Vision II (Coherent) (Dibaj et al., 2010), in combination with ScanImage software (Pologruto et al., 2003) was used. For transgenic GCaMP3 excitation, the laser wavelength was set to 890 nm and the power was adjusted from 8 to 60 mW, depending on the imaging depth in the tissue. 2P-LSM was performed on the white matter of the dorsal funiculus for *in vivo* and *ex vivo* preparations as well as on the dorsal horn grey matter for *ex vivo* preparations up to a 100-150 µm depth by using a long-distance W Plan-Apochromat 20x 1.0 NA DIC objective (Zeiss). Areas of white and grey matter were recorded as uniformly spaced planes of field of views (FOV) with 256 x 256 pixel per image, 1.4 µs pixel dwell time and GCaMP3 emission was acquired using a 500/24 nm band pass filter, detected by a photomultiplier tube H10770PB-40 (Hamamatsu Photonics). During 2P-LSM *in vivo* recordings, animals were kept under inhalation anesthesia with 1.5 % isoflurane on a heating plate and for *ex vivo* imaging, spinal cord slices were continuously perfused with carbonated aCSF at room temperature.

5.2.7 EXPERIMENTAL DESIGN

For a better illustration of the experimental design, both study models for physiological and pathophysiological conditions are shown graphically below. The figure shows how transgenic mice were examined experimentally using the methodology of laminectomy, acute slice preparation, demyelination model and immunohistochemistry (**Figure 6**).

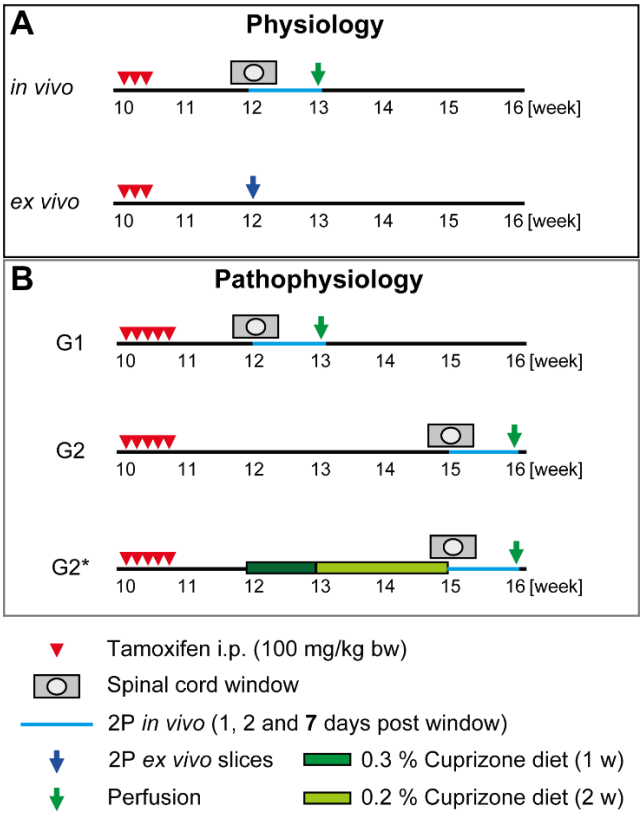

Figure 6: Experimental design of this study.

Tamoxifen induced GCaMP3 expression was initiated in mice at 10 weeks of age to record physiological Ca^{2+} signals two weeks later either *in vivo* after laminectomy during a chronic phase of one week or acutely in *ex vivo* slice preparations (**A**). To investigate a pathophysiological influence on Ca^{2+} signaling and glial cell characteristics, mice were divided into three groups. G1 served as age control for changes in recombination, G2 was chosen as a control for demyelination and G2* received a cuprizone diet for three weeks to induce toxic demyelination (**B**). Laminectomy and 2P-LSM protocols match A. All spinal cords were collected for IHC after 2P-LSM (day 7) by transcardial perfusion.

5.2.8 Automated ROA-based detection of Ca^{2+} events (activity dependent Ca^{2+} analysis)

(Stopper et al., 2022)

For automated region of activity (ROA)-based Ca^{2+} analysis, a custom-made analysis software based on MATLAB was used and fed with 2P-LSM FOV recordings, including metadata from ScanImage software. Fluorescence fluctuations at basal Ca^{2+} concentrations (F_0) were computed along the temporal axes of each individual pixel. The range projection of $\Delta F/F_0$ was then used to identify local fluorescence maxima, serving as seed points for simultaneous, correlation-based region growing. Temporal correlation of a candidate pixel with the corresponding seed point was computed using Pearson's linear correlation coefficient. A user-definable correlation threshold was used to stop the region growing process as soon as the temporal evolution of a candidate pixel deviated from its

respective seed point. Pixels belonging to two adjacent regions were marked as boundary pixels. Prior to F_0 estimation, image stacks were denoised using the PURE-LET algorithm (Luisier et al., 2011), image registration and a temporal median filter of size 3 to correct small motion artefacts and simultaneously retain sharp transient edges. Based on the pre-processed data (F), F_0 was estimated by fitting a polynomial of user-definable degree to a cleaned-up signal, where potential fluorescence transients were statistically excluded. Ca^{2+} event detection and analysis were performed on the normalized dataset ($\Delta F/F_0$). Further signal detection parameters are listed in **Supplementary Table 1**. The parameters used for the final analysis and their explanation are listed in **Table 6** (Rieder et al., 2022).

Table 6: Explanation of parameters used for Ca^{2+} characterization (key parameters in bold).

Feature	Explanation	Unit
Amplitude	Local maximum peak within a ROA	$\Delta F/F_0$
Area	Area covered by a ROA in domain units	μm^2
Deca time	Time interval between 90 % of the peak value and signal end	s
Duration	Full Width at Half Maximum (FWHM) of the signal curve	s
Frequency	Signal frequency within a chosen ROA based on the mean value of all peak-to-peak times divided by the number of signals associated to that ROA	min^{-1}
Integrated fluorescence	Area under the signal curve in correspondence of the signal duration	$\Delta F/F_0$
Rise time	Time interval between signal start and 90 % of the peak value	s
ROA density	Number of ROAs detected within a Field of View (FOV) divided by the FOV area	$10^{-3}/\mu m^2$
Signal density	Number of signals detected within a FOV divided by the FOV area	$10^{-3}/\mu m^2$
Signal start/end	Intersections of the signal curve with the horizontal line corresponding to 50 % of the signal peak amplitude	
Coincidence index	Number of simultaneously active ROAs within a FOV normalized to the total number of ROAs	c.i.

5.2.9 TISSUE FIXATION AND IMMUNOHISTOCHEMISTRY

Lethal anesthetized animals were transcardially perfused with phosphate-buffered saline (PBS) and tissue was fixed by 4 % formaldehyde perfusion. After 24 h post fixation in 4 % formaldehyde, T13-L1 spinal cord segments were dissected and detached from meninges. The spinal cord tissue was maintained in PBS and cut in sections (40 µm) by vibratome (VT1000 S) (Leica, Nußloch, Germany). Free floating slices were processed for immunohistochemistry (IHC) (Huang et al., 2020). In case of myelin staining, the sections were pretreated with ethanol (> 99 %) for 10 min and then washed three times with PBS for 10 min. Otherwise first incubation in blocking solution at room temperature was followed by primary antibody solution incubation overnight at 4 °C, three times washing with PBS for 10 min and subsequently secondary antibody solution incubation for 2 h at room temperature. After washing three times for 10 min with PBS, slices were mounted in Shandon ImmuMount (Thermo Scientific). To detect glial markers (**Table 1**), images were acquired by epifluorescence and confocal microscopy.

5.2.10 MAGNETIC CELL SEPARATION (MACS) OF OPCS AND QUANTITATIVE RT-PCR

(Fang et al., 2022b)

Anesthetized animals were perfused using ice-cold Hank's balanced salt solution without Ca^{2+} and Mg^{2+} (HBSS, Gibco) and the spinal cord was dissected on ice after it was flushed out by a syringe using HBSS. The sorting was performed on the basis of the manufacturer's instructions (Miltenyi Biotec) with minor adjustments: First, removal of debris (130-107-677) was performed and cells were resuspended using 1 ml "re-expression medium" containing NeuroBrew-21 (1:50 in MACs neuro Medium (130-093-566, 130-093-570)) and 200 mM L-glutamine (1:100, Sigma) at 37 °C for 30 min. Second, removal of myelin (130-096-731) for 15 min at 4 °C was performed and afterwards cells were incubated with Fc-receptor blocker for 10 min at 4 °C, followed by incubation with 10 µl microbeads mixture (antibodies against CD140 (130-101-502), NG2 (130-097-170) and O4 (130-096-670) in 1:1:1) at 4 °C. For further western blot processing, MACs-sorted NG2 glia were lysed by RIPA buffer (Thermo Scientific).

For quantitative real-time PCR (RT-PCR), MACs oligodendrocyte precursor cells were homogenized as described above. NucleoSpin RNA Plus XS kit (Macherey-Nagel) was used to extract mRNA. Omniscript kit (QIAGEN) was used for reverse transcription and RT-PCR was performed using EvaGreen (Axon) kit with a CFX96 Real Time System (BioRad) and the primer sequences listed in **Table 3**.

5.2.11 AUTOMATED SLIDE SCANNING BY EPIFLUORESCENCE MICROSCOPY

Fixed and immunostained spinal cord slices were scanned with the automated slide scanner AxioScan.Z1 (Zeiss). The automated slide scanner is an epifluorescence microscope equipped with a Colibri 7 LED light source and a Plan-Apochromat 10x/0.45 and 20x/0.8 objectives acquiring imaging stacks (5 µm stacks, variance projection) with appropriate beam splitters for DAPI (405 nm), Alexa Fluor 488 (495 nm), Alexa Fluor 555 (573 nm), Alexa Fluor 647/Cy 5 (652 nm) and Alexa Fluor 750 (762 nm). The setup and image acquisition were controlled by ZEN black 2.3 software (Zeiss).

5.2.12 CONFOCAL LASER-SCANNING MICROSCOPY

Confocal magnification images (512 x 512 pixel, 1.54 µs pixel dwell time) were acquired with the confocal laser-scanning microscope cLSM 880 (Zeiss) using a Plan-Apochromat 63x/1.4 Oil DIC M27 objective. Fluorescent markers were excited with argon (488 nm) and helium-neon lasers (542 nm) and appropriate beam splitters. The setup and image acquisition were controlled by ZEN black 2.3 software (Zeiss) as for the slide scanner.

5.2.13 SOFTWARE AND IMAGE ANALYSIS

For 2P-LSM recordings, the open-source MATLAB-based software application ScanImage® (Vidrio Technologies, Ashburn, VA, USA) (Pologruto et al., 2003) was used. The custom-made MATLAB-based software MSparkles (Stopper et al., 2022), GraphPad Prism 9 and Microsoft Office Excel 2019 were used for data analysis. Immunohistochemical data were generated, visualized and modified using the ZEN blue lite 3.6 imaging software (Zeiss) and the ImageJ 1.53q collection Fiji. For figure layout, the Adobe Creative Suite 2022 was used (Adobe InDesign®, Adobe Illustrator®, Adobe Photoshop®). Schematic drawings were created or modified with BioRender.com.

As an example of immunohistochemical image analysis, an MBP staining acquired using the automated slide scanner and confocal microscope is shown below. Highlighted are the areas used for fluorescence intensity measurement and cell counting, as well as the transversal sectioned myelin sheaths for myelin thickness determination (g-ratio), randomly selected by cells matching crossings with a 10 x 10 software gird overlapping the image (**Figure 7**).

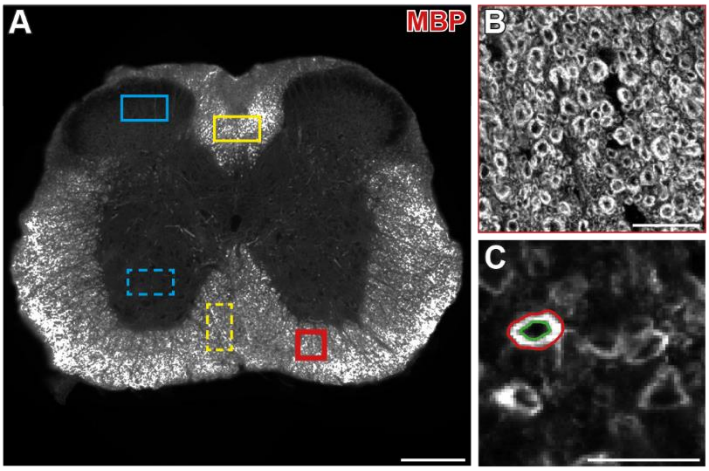

Figure 7: Immunohistochemical image analysis.

Overview image with the slide scanner (**A**; scale bar = 100 µm) shows in yellow the areas for cell counting and fluorescence intensity measurement in the white matter and in blue for the gray matter (solid frame for dorsal, dashed frame for ventral). Alongside, the confocal image of the ventral white matter (**B**; scale bar = 10 µm) and the outer edge of a transversely sectioned myelin sheath defined in red and the inner edge in green (**C**; scale bar = 10 µm).

5.2.14 Statistics

Unless otherwise stated, data are represented as mean ± SEM or median with interquartile range. Single datasets were analyzed using a Shapiro-Wilk normality test and represented as medians or means. Data were compared using an ordinary one-way ANOVA with Bonferroni's multiple comparisons, a Kruskal-Wallis test with Dunn's multiple comparisons test or unpaired t-test. If the test's p-value summary was significant, no multiple comparison test between single data sets was performed. Further test information is given in the corresponding figure legend. For statistical comparisons, following p-values were used: * $p<0.05$; ** $p<0.01$; *** $p<0.001$, **** $p<0.0001$.

5.2.15 Ethics statement

All animal experiments were performed at the University of Saarland, Center for Integrative Physiology and Molecular Medicine (CIPMM), in strict accordance with the recommendations to European and German guidelines for the welfare of experimental animals and approved by the "Landesamt für Gesundheit und Verbraucherschutz" of the state Saarland (animal license number 34/2016, 36/2016, 03/2021 and 08/2021). For each group in an experiment, the number of animals was N = 4.

6 RESULTS

6.1 TAMOXIFEN-INDUCED GCAMP3 EXPRESSION IN ASTRO-, MICROGLIA AND OLIGODENDROCYTE PRECURSOR CELLS

To visualize live Ca^{2+} fluctuations in glial cells as a cell activity readout, the DNA recombinase CreERT2 was used to induce cell-specific expression of the genetically encoded Ca^{2+} indicator GCaMP3 in a time-dependent manner by tamoxifen administration (Paukert et al., 2014). First, the recombination efficiency in astroglia, microglia, and NG2 glia (oligodendrocyte precursor cells (OPCs)) was examined.

For this purpose, 10-week-old mice with C57BL/6N background and CreERT2 expression either under the control of the human glial fibrillary acidic protein (GFAP) promoter for astroglia (Hirrlinger et al., 2006), or knocked into the C-X3-C motif chemokine receptor 1 (CX_3CR_1) (microglia; (Yona et al., 2013)), or knocked in the neural/glial antigen 2 (NG2 locus upstream of exon 2) OPCs (Huang et al., 2014) were treated with tamoxifen (100 mg/kg body weight, i. p., three times, once per day) to express GCaMP3.

Cellular recombination efficiency was determined by colocalization of green fluorescent protein (GFP) and GFAP for astroglia (**Figure 8A**), GFP and ionized calcium-binding adapter molecule 1 (Iba1) for microglia (**Figure 8C**), and GFP and platelet-derived growth factor receptor α (PDGFRα) for OPCs (**Figure 8E**) two weeks after tamoxifen administration in transversal sections of the lumbar spinal cord (L3-L6) for white and gray matter, respectively. The cell population of protoplasmic astroglia appeared typically heterogeneous, with filamentous in white matter and with fine-bush morphology in gray matter, and tended to have higher recombination efficiencies in white (87.1 ± 4.2 %) than in gray matter (77.6 ± 2.7 %; **Figure 8B**). The microglia, morphologically homogeneous throughout the spinal cord with typical slim cell body and branched, fine processes, showed a very high recombination efficiency in both white (99.0 ± 0.6 %) and gray matter (99.1 ± 0.6 %; **Figure 8D**). The OPCs were also homogeneously distributed and characterized by their multipolar cell structure and showed a low recombination efficiency in white (82.3 ± 5.4 %) and gray matter (78.8 ± 6.2 %; **Figure 8F**) than microglia and comparable with astroglia, although recombined pericytes were not included in the analysis.

In conclusion, tamoxifen injection resulted in high recombination efficiency of GCaMP3 expression reflected by GFP^+ cells within two weeks for the three used transgenic mouse lines showed by colocalization with cell-specific markers for astroglia, microglia, and OPCs in the lumbar spinal cord. On the basis of these results, mice were then used after laminectomy *in vivo* or for acute slices *ex vivo* for live Ca^{2+} imaging at 12 weeks of age by

two-photon laser-scanning microscopy (2P-LSM), whereas abnormal cell reaction caused by laminectomy was excluded by immunohistochemistry (Rieder et al., 2022).

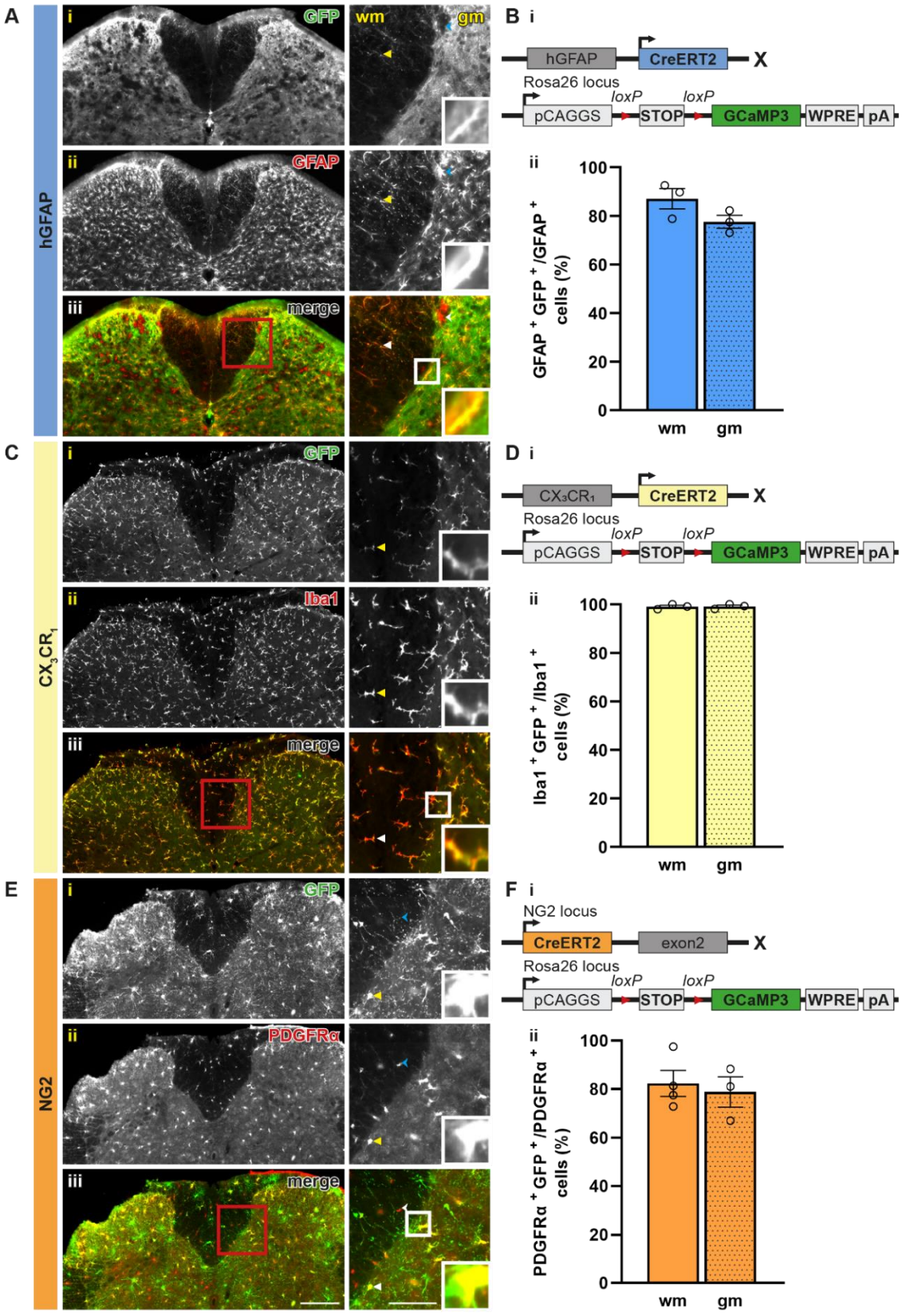

Figure 8: Highly specific tamoxifen-induced GCaMP3 expression in glial cells of the mouse spinal cord.

Staining for respective GCaMP3/GFP (i) expression in GFAP$^+$ astroglia (**Aii**), Iba1$^+$ microglia (**Cii**), and PDGFRα$^+$ OPCs (**Eii**) and corresponding overlay (iii) with magnification of the dorsal interface between white and gray matter, and focus on a single positive cell (each shown on the right), and cell-specific recombination efficiency for white and gray matter in astroglia (**Bi-ii**), microglia (**Di-ii**), and NG2 glia (OPCs) (**Fi-ii**). Yellow arrows highlight double positive cells, blue arrows indicate GFP$^-$ cells. Scale bar = 500 µm (iii) and 100 µm for zoom; N = 3-4.

6.2 SPONTANEOUS AND EVOKED CA^{2+} SIGNALS IN SPINAL AND PERIPHERAL ASTROGLIA

Ca^{2+} signals in astroglia, visualized by the genetically encoded sensor GCaMP3 can occur spontaneously or evoked. In the course of this work, mainly spontaneous glial Ca^{2+} signals were recorded and measured. In this chapter, in contrast, the possibility of induced Ca^{2+} activity and a comparison of evoked signals by chemical and electrical stimulation will be presented, along with the features of the program MSparkles capable for analysis of different Ca^{2+} signals to investigate the differences of spontaneous and chemically or electrically induced Ca^{2+} fluctuations and their properties.

Two weeks after tamoxifen administration, spontaneous and electrically Ca^{2+} activity was measured in spinal GFAP$^+$ astroglia (**Figure 9A**) *in vivo*, and chemically induced Ca^{2+} activity was measured in astroglial, glutamate aspartate transporter (GLAST) positive satellite glial cells (**Figure 9B**) of the dorsal root ganglion (DRG) *ex vivo* for easy access and chemical bolus application. Two different Cre-driver mouse lines were used here, since astroglial satellite cells in DRG are not GFAP but GLAST positive (Carozzi et al., 2008). All Ca^{2+} data shown here and below, acquired with 2P-LSM, were processed using MSparkles, a MATLAB-based software program for automatic and objective analysis of fluorescence intensity changes (Stopper et al., 2022). This software tool allowed an automatic and bias-free detection of static, not dynamic regions of activity (ROAs) relying on a range projection of $\Delta F/F_0$ and a temporal correlation based on the algorithm of this projection (see chapter 5.2.8). The spontaneously occurring Ca^{2+} signals in spinal astroglia after laminectomy and spinal cord window implantation (**Figure 9C**) occurred over a few seconds with spreading across multiple ROAs (**Figure 9Ci-iv**) and high synchronicity (**Figure 9Cvii**) within a field of view (FOV). Furthermore, not only spontaneous but also chemically induced Ca^{2+} activity was measured in acute *ex vivo* preparations of DRGs by bolus application of 50 µM noradrenaline (**Figure 9Di-vi**), which occurred for a short time with high synchronicity across the majority of detected ROAs (**Figure 9Dvii**). In addition to the chemically induced Ca^{2+} activity *ex vivo*, Ca^{2+} signals were also measured immediately after electrical

stimulation *in vivo*. Together with the placement of the spinal cord window, biocompatible surface electrodes (adapted to spinal application (Schweigmann et al., 2021)) were implanted, allowing electrical stimulation with a gradient increasing (**Figure 9E**) and a tetanically constant (**Figure 9F**) current intensity. Stimulation with increasing current intensity showed the largest amplitude of the fluorescence intensity change at 750 µA (**Figure 9Evi**) and comparatively consistent synchronicity of the signals in all ROAs (**Figure 9Evii**). In contrast, in the next step with tetanically constant repeated stimulation at 750 µA, a decrease in amplitude and synchronicity was measured after the second stimulation in series (**Figure 9Fvi-vii**).

Summarizing, MSparkles can be used to measure a wide variety of Ca^{2+} activities. Spontaneous and chemically evoked Ca^{2+} signals in different astroglia were comparable in their duration and strength of fluorescence intensity change as well as synchronicity. An electrical stimulation with a current of 750 µA induced a strong fluorescence change with very high synchronicity, but this was not equally prominent with repeated stimulation of the same current.

Figure 9: Spontaneous, chemically and electrically mediated Ca^{2+} activity in spinal and peripheral astroglia.

Mouse constructs for cell-specific GCaMP3 expression in spinal astroglia (**A**) and satellite glial cells of the DRG (**B**). Spontaneous Ca^{2+} activity in spinal astroglia *in vivo* (**C**). Maximum intensity projection (i) with time course of Ca^{2+} activity (ii-iv) and ROAs (v) automatically detected by MSparkles, plus the corresponding signal trace (vi) and fluorescence change shown as a heat map with synchronicity progression (vii). Chemically induced Ca^{2+} activity in astroglial satellite cells in the DRG by bolus application of 50 µM noradrenaline via a pipette *ex vivo* (**D**). *In vivo* Ca^{2+} activity in spinal astroglia stimulated electrically via surface electrodes by increasing current intensity (500-1250 µA/0.5 mm^2, 50 pulses, 50 µs pulse width; **E**) respectively repeated constant current intensity (750 µA/0.5 mm^2; **F**). Scale Bar = 50 µm.

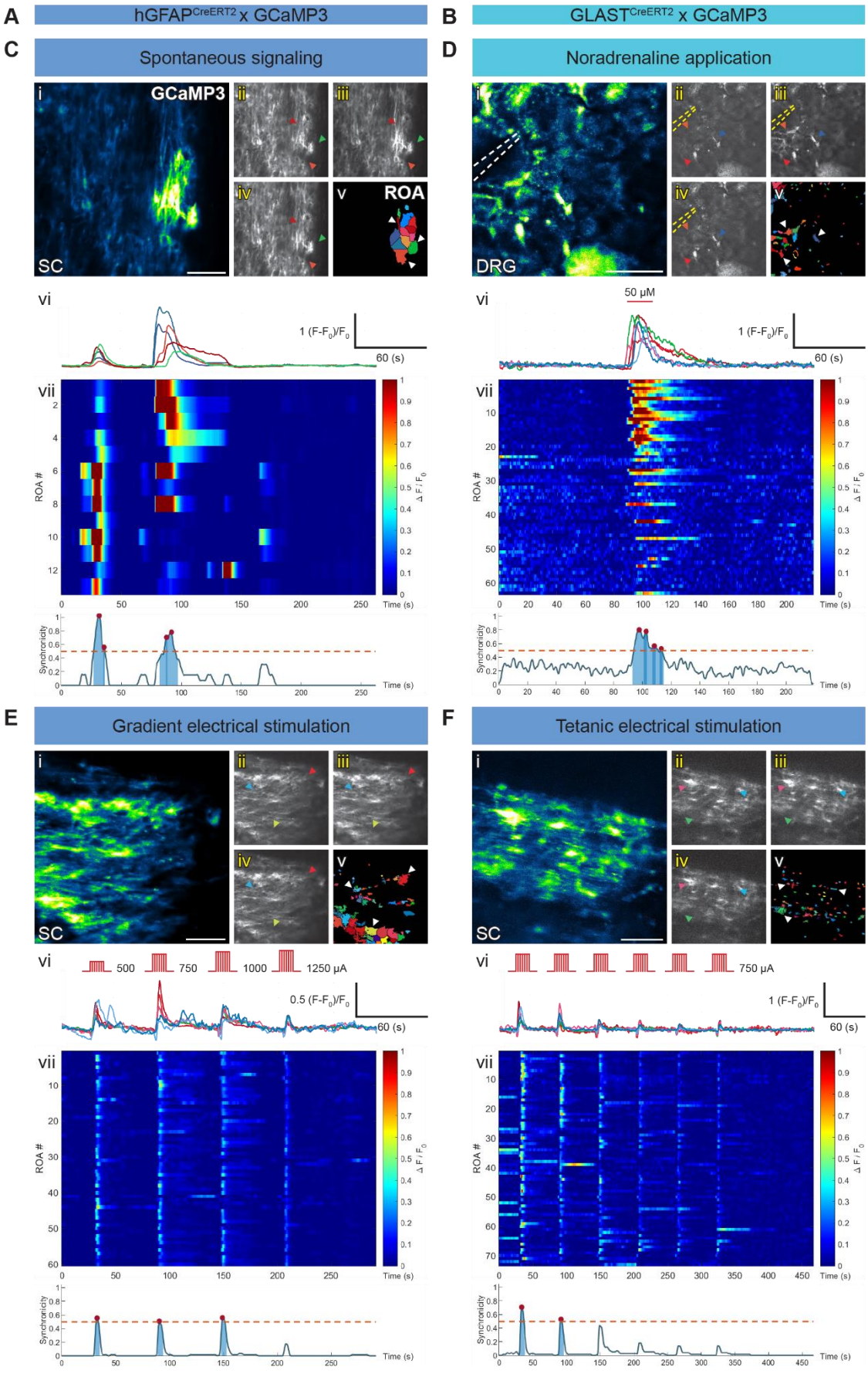
A
hGFAP^CreERT2 x GCaMP3
B
GLAST^CreERT2 x GCaMP3
C
Spontaneous signaling
D
Noradrenaline application
GCaMP3
ROA
SC
DRG
50 µM
1 (F-F0)/F0
60 (s)
ROA #
Time (s)
Synchronicity
E
Gradient electrical stimulation
F
Tetanic electrical stimulation
500
750
1000
1250 µA
750 µA
0.5 (F-F0)/F0

6.3 CELL-SPECIFIC Ca^{2+} ACTIVITY BETWEEN ASTRO-, MICROGLIA AND OPCS IS DISTINGUISHABLE BY KEY SIGNAL PARAMETERS *IN VIVO*

The activity of the second messenger Ca^{2+} is essential for a variety of cellular functions and communication in glial cells. To identify these cell-specific differences, *in vivo* spinal Ca^{2+} signals were recorded two weeks after tamoxifen administration via 2P-LSM in astro- (hGFAP$^+$), micro- ($CX_3CR_1^+$) and NG2$^+$ glia (OPCs) and analyzed by MSparkles.

In anesthetized mice, spontaneous Ca^{2+} fluctuations were measured by changes in GCaMP3 fluorescence intensity after laminectomy and implantation of a spinal cord window for chronic imaging one, two, and seven days after surgery. The GCaMP3 expression displayed the highly branched cell structure of astroglia (**Figure 10Ai**) and was distributed among few ROAs (**Figure 10Aii-iii**) identified by MSparkles. In contrast, larger and more ROAs were detected in elongated microglia (**Figure 10Aiv-vi**). The typical morphology of OPCs was evident in their recording with very small ROAs but multiple signals (**Figure 10Avii-ix**). Six key parameters were identified to reveal differences in spinal Ca^{2+}signaling characteristics between the three glial cell types regarding day seven of the recordings. The detected signal density (1) was comparatively high in microglia ($8.68 \pm 6.97 \times 10^{-3}/\mu m^2$) and OPCs ($8.26 \pm 4.37 \times 10^{-3}/\mu m^2$) compared to (p-value = 0.0395) less signals in astrocytes ($0.59 \pm 6.51 \times 10^{-3}/\mu m^2$; **Figure 10B**). The highest density of active regions (2) was found for microglia ($2.87 \pm 0.16 \times 10^{-3}/\mu m^2$) with (p-value = 0.0005-0.0006) approximately tenfold fewer ROAs in astrocytes ($0.81 \pm 0.45 \times 10^{-3}/\mu m^2$) and OPCs ($0.76 \pm 0.08 \times 10^{-3}/\mu m^2$; **Figure 10C**). One would expect that a high signal density and at the same time a high density of active regions would also lead to a high coincidence (3) of activity, however, the highest coincidence was found in OPCs (0.16 ± 0.01), higher than in microglia (0.10 ± 0.01, p-value = 0.0077) and astrocytes (0.03 ± 0.02, p-value = <0.0001), with the lowest values also showing less coincident signals than microglia (p-value = 0.0053; **Figure 10D**). For the size of automatically detected ROAs ((4) **Figure 10E**), a similar area was detected for astrocytes ($157.8 \pm 55.0\ \mu m^2$) and microglia ($137.1 \pm 27.6\ \mu m^2$), whereas the smallest area was detected by OPCs ($24.63 \pm 4.68\ \mu m^2$), that were smaller than that of astrocytes (p-value = 0.0268). For the signal amplitude ((5) **Figure 10F**) of the fluorescence change after background correction, there were no differences between the Ca^{2+} signals of the three cell types (astroglia: $0.15 \pm 0.02\ \Delta F/F_0$; microglia: $0.16 \pm 0.01\ \Delta F/F_0$; OPCs: $0.18 \pm 0.02\ \Delta F/F_0$). Comparable to the ROA area, the signal duration ((6) **Figure 10G**) between astrocytes (8.61 ± 2.18 s) and microglia (7.56 ± 0.98 s) was of similar length, and OPCs exhibited two and a half times shorter signals (3.24 ± 0.29 s) that were shorter compared with astrocytes (p-value = 0.0232). In addition to the six parameters already described for identifying Ca^{2+} activity, in **Supplementary Figure 1** five additional parameters (signal frequency

Supplementary Figure 1G, integrated fluorescence **Supplementary Figure 1H**, mean fluorescence **Supplementary Figure 1I**, signal rise and decay time **Supplementary Figure 1J-K**) were collected and summarized. Furthermore, all recording days (day one, two and seven) are listed there. For most additional parameters, no differences were found between the individual recording days within the cell types. Only OPCs showed an increase in coincidence (d1: 0.13 ± 0.01, d2: 0.11 ± 0.00, d7: 0.19 ± 0.01) and signal frequency (d1: 1.90 ± 0.13 min^{-1}, d2: 2.14 ± 0.17 min^{-1}, d7: 2.99 ± 0.34 min^{-1}) on day seven compared to days one (coincidence p-value = 0.0435, signal frequency p-value = 0.0005) and two (coincidence p-value = 0.0107, signal frequency p-value = 0.0044). In addition, the highest signal frequency was found in OPCs at all time points and similar to the signal duration, the lowest signal rise and decay time was revealed (**Supplementary Figure 1G**). The fluorescence of the signals remained indiscriminate throughout. The remaining days performed predominantly similar to the data already shown for day seven and also reflected similar differences within the three cell types.

To summarize *in vivo* Ca^{2+} activity in astrocytes, microglia, and OPCs (NG2 glia), it can be concluded that Ca^{2+} signals are cell type specific and only slight changes occur over one week. Comparatively high signal density and frequency were found in a few, small ROAs, highly coincidental and short in duration for OPCs. Microglia had comparatively large number of signals in many ROAs of medium coincidence, area, and length. And for astrocytes, relatively few signals revealed in ROAs of medium size, low number, and coincidence with medium length.

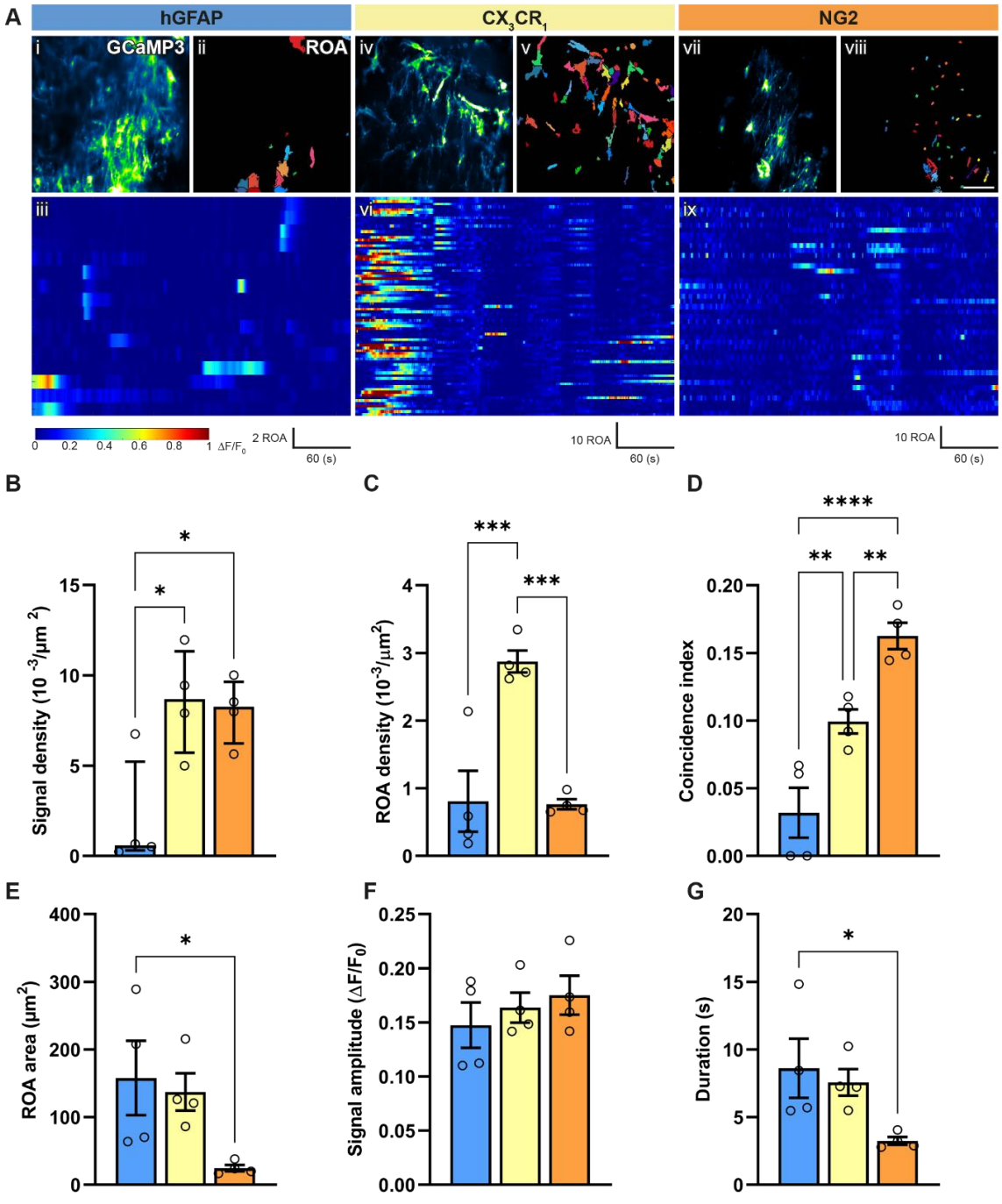

Figure 10: Cell-specific *in vivo* Ca^{2+} signaling in astro-, microglia and OPCs.

Fluorescence changes of the Ca^{2+} indicator GCaMP3 in hGFAP^{+}, $CX_3CR_1^{+}$ and NG2^{+} cells automatically detected by MSparkles (**A**). Maximum intensity projection of the image, automatically detected ROAs as a color-coded map and the fluorescence change over time of all ROAs as a heatmap for astroglia (**Ai-iii**), microglia (**Aiv-vi**) and NG2 glia (OPCs; **Avii-ix**). Six parameters signal density (**B**), ROA density (**C**), coincidence index (**D**), ROA area (**E**), signal amplitude (**F**) and signal duration (**G**) are used to separate Ca^{2+} activity seven days after laminectomy between cell types. Scale bar = 50 µm. N = 4, the mean or median values ± SEM/IQR from several FOVs (n = 16) are shown and compared using ordinary one-way ANOVA or Kruskal-Wallis test. *p <0.05, **p <0.01, ***p <0.001, ****p <0.0001.

6.4 DIFFERENT *EX VIVO* Ca^{2+} ACTIVITY ONLY IN ASTROGLIA AND OPCS BETWEEN WHITE AND GRAY MATTER OF THE SPINAL CORD

Although the spinal cord with its outer white matter is very suitable for the study of cellular conditions in the myelin environment *in vivo*, for comparative study of glial cells in white and gray matter, *ex vivo* slice preparations have to be relied upon because imaging in the deeper gray matter is strongly affected by the light refractive property of the overlying lipid-containing white matter.

For this purpose, mice expressing GCaMP3 in astroglia, microglia, or OPCs (NG2 glia) were cervically dislocated two weeks after tamoxifen administration. The spinal cord was exposed in artificial CSF and fresh sections were prepared. Under continuous carbogenization and artificial CSF flow, Ca^{2+} activity in glial cells was recorded by 2P-LSM as described in the previous chapter. Switching between white and gray matter was performed using a transmitted light camera, in which the slightly darker gray matter could be distinguished from the lighter white matter. The images showed a typical region-specific morphology for astroglia, accompanied by distinct finer branching of the cells in the gray matter than in the white matter (**Figure 11Ai, Bi**). The detected ROAs appeared larger and were more numerous in the gray matter than in the white matter (**Figure 11Aii-iii, Bii-iii**). The morphology of microglia in both substances was spherical in character with very low numbers of ROAs (**Figure 11Aiv-vi, Biv-vi**). Third, no morphological differences between gray and white matter for OPCs was discerned at first sight, with Ca^{2+} activity distributed among a large number of small projections (**Figure 11Avii, Bvii**). Also, the shape and activity of the ROAs appeared the same in the heatmaps, but were characterized by a strong initial activation at the beginning of the recordings (**Figure 11Aviii-ix, Bviii-ix**).

Automatic analysis of Ca^{2+} activity revealed relatively similar data distribution in the six key parameters as previously shown *in vivo*. Only for microglia a reduction of Ca^{2+} activity between the two imaging methods could be shown. There were no differences in signal density (**Figure 12A**), ROA density (**Figure 12B**), signal amplitude (**Figure 12E**), or signal duration (**Figure 12F**) between the two regions studied (white and gray matter). But for OPCs an increased (p-value = 0.0428) coincidence of Ca^{2+} activity (**Figure 12C**) could be detected in white matter (0.12 ± 0.02) compared to gray matter (0.07 ± 0.01). In contrast, for astroglia, a larger (p-value = 0.0422) area of ROAs (**Figure 12D**) by almost double could be identified in gray (37.00 ± 3.47 μm^2) than in white matter (19.92 ± 5.67 μm^2). No cell type specific differences between white and gray matter could be identified in the additional parameters signal frequency, integrated fluorescence, mean fluorescence, and signal rise and decay time (**Supplementary Figure 2**).

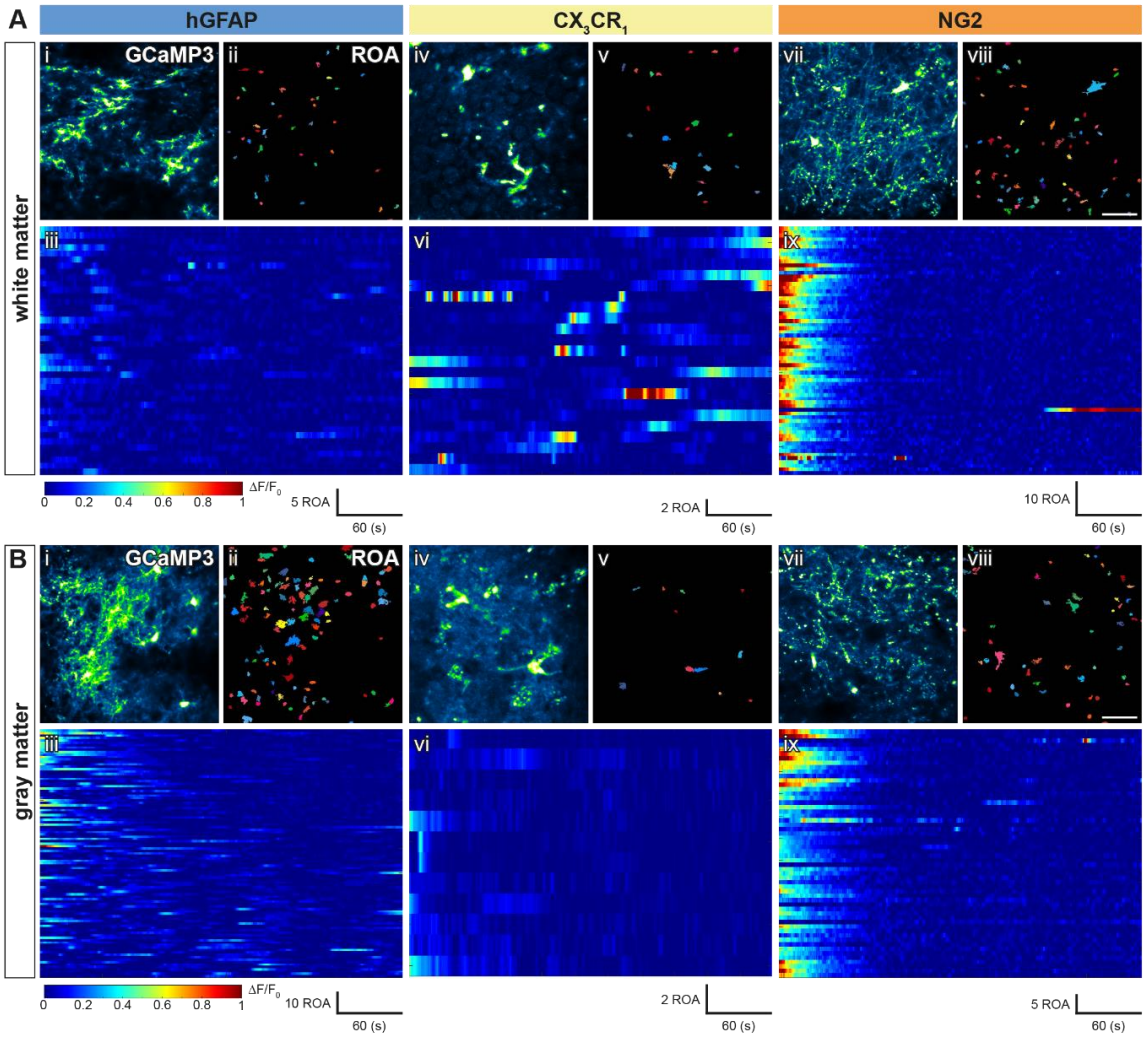

Figure 11: Exemplaric *ex vivo* Ca^{2+} activity in acute spinal cord slices.

Representative illustration of GCaMP3 signal differences in white (**A**) and gray matter (**B**) with maximum intensity projection, respectively, automatic ROA detection shown as a map and corresponding activity distribution as a heatmap for astroglia (i-iii), microglia (iv-vi) and NG2 glia (OPCs; vii-ix). Scale bar = 50 µm.

In brief, *ex vivo* slice preparation revealed Ca^{2+} activity for astroglia, microglia, and OPCs (NG2 glia) in both white and gray matter, and cell type-specific signaling differences were identified. Thus, morphological differences in Ca^{2+} activity in astroglia were found with concomitant changes in ROA area to more large-scale signals in gray matter. Furthermore, although morphologically identical, there were higher coincidences of signals for OPCs in gray matter than in white matter. In general, this preparation method showed good feasibility and quality with a morphological change of microglia towards a more activated form. For simplicity, differences between cell types were not statistically compared here and only differences between regions were highlighted.

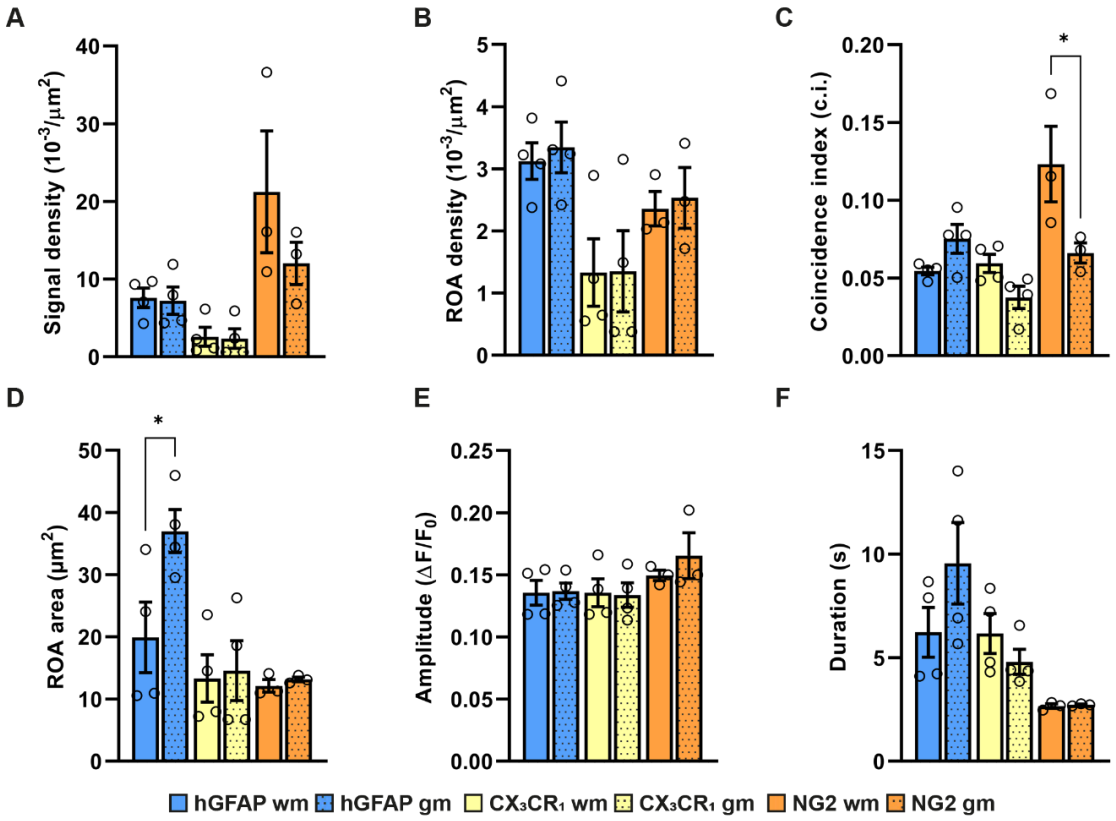

Figure 12: Ca^{2+} activity in fresh spinal cord slices differs between white and gray matter in a cell type-specific manner.

Automated activity analysis using MSparkles for the six key parameters signal density (**A**), ROA density (**B**), coincidence index (**C**), ROA area (**D**), signal amplitude (**E**), and signal duration (**F**) shows reduced coincidence for NG2 glia (OPs) and increased ROA area for astroglia in gray matter. N = 3-4, the mean or median values ± SEM/IQR from several FOVs (n = 12-16) are shown and the two matters per cell type were compared using unpaired t- or Mann-Whitney test. *p <0.05.

6.5 Inducing an OPC-specific conditional $GABA_B$ knockout to manipulate cell physiology

Since the metabotropic $GABA_B$ receptor in OPCs is suspected to affect intracellular Ca^{2+} concentrations via the cAMP signaling pathway or via IP_3-mediated internal Ca^{2+} release (Bai et al., 2021), the pathophysiological impact of its loss for cellular Ca^{2+} activity was investigated using a conditional knockout mouse.

For studying the effects of the conditional $GABA_B$ receptor knockout in OPCs, the $NG2^{GCaMP3}$ mouse line presented previously and serving as control (ctl) was crossed with the $GABA_B$-floxed mouse line (Haller et al., 2004) in which floxed exons seven and eight of the $GABA_{B1}$ subunit are excised after tamoxifen administration. Hence, subsequent results were used synonymously as ($GABA_B$) ctl for OPCs (NG2 glia) expressing GCaMP3 (**Figure 13Ai**) and ($GABA_B$) cKO for OPCs expressing GCaMP3 and lacking $GABA_{B1}$ subunit

(**Figure 13Aii**). After transcardial perfusion of ctl and cKO mice with Hanks' Balanced Salt Solution, a spinal cord homogenate was prepared. Magnetic-activated cell sorting (MACS) was used to sort spinal cell populations into $NG2^-$ (flow) and $NG2^+$ (sorted) cells (**Figure 13B**) for subsequent analysis of quantitative mRNA expression of the *GABABR1* gene by RT-PCR two weeks after five times tamoxifen administration at ten weeks of age (**Figure 13C**). Quantitative analysis of the purity of sorted cells was performed by RT-PCR for OPC- (*CSPG4* = Chondroitin sulfate proteoglycan 4, *PDGFRA*), astroglia- (*AQP4* = Aquaporin-4), and immune cell-specific genes (*ITGAM* = Integrin alpha M; **Figure 13D**). Relative mRNA levels normalized to NG2-sorted cells were increased for *CSPG4* and *PDGFRA* in sorted cells (*CSPG4*: 1.00 ± 0.18; *PDGFRA*: 11.97 ± 1.59) compared with flow cells (*CSPG4*: 0.34 ± 0.03, p-value = 0.0248; *PDGFRA*: 0.82 ± 0.21, p-value = 0.0001). Whereas for the flow cells (*AQP4*: 3.56 ± 0.30; *ITGAM*: 21.58 ± 0.87), mRNA levels were increased for *AQP4* and *ITGAM* compared to sorted cells (*AQP4*: 1.30 ± 0.25, p-value = 0.0004; *ITGAM*: 1.22 ± 0.45, p-value = <0.0001). After confirmation of OPC purity, a reduction of 37 % (p-value = 0.0336) in cKO (0.63 ± 0.09) compared with ctl (1.00 ± 0.11) was found for the relative mRNA expression of *GABABR1* by RT-PCR analysis (**Figure 13E**).

Summarizing this section, a cell type-specific knockout of the metabotropic $GABA_B$ receptor in OPCs could be induced by tamoxifen administration. The purity of MACS sorted OPCs was verified by RT-PCR and a significant forty percent reduction in mRNA encoding the B1 subunit of the $GABA_B$ receptor was detected only two weeks later as cKO.

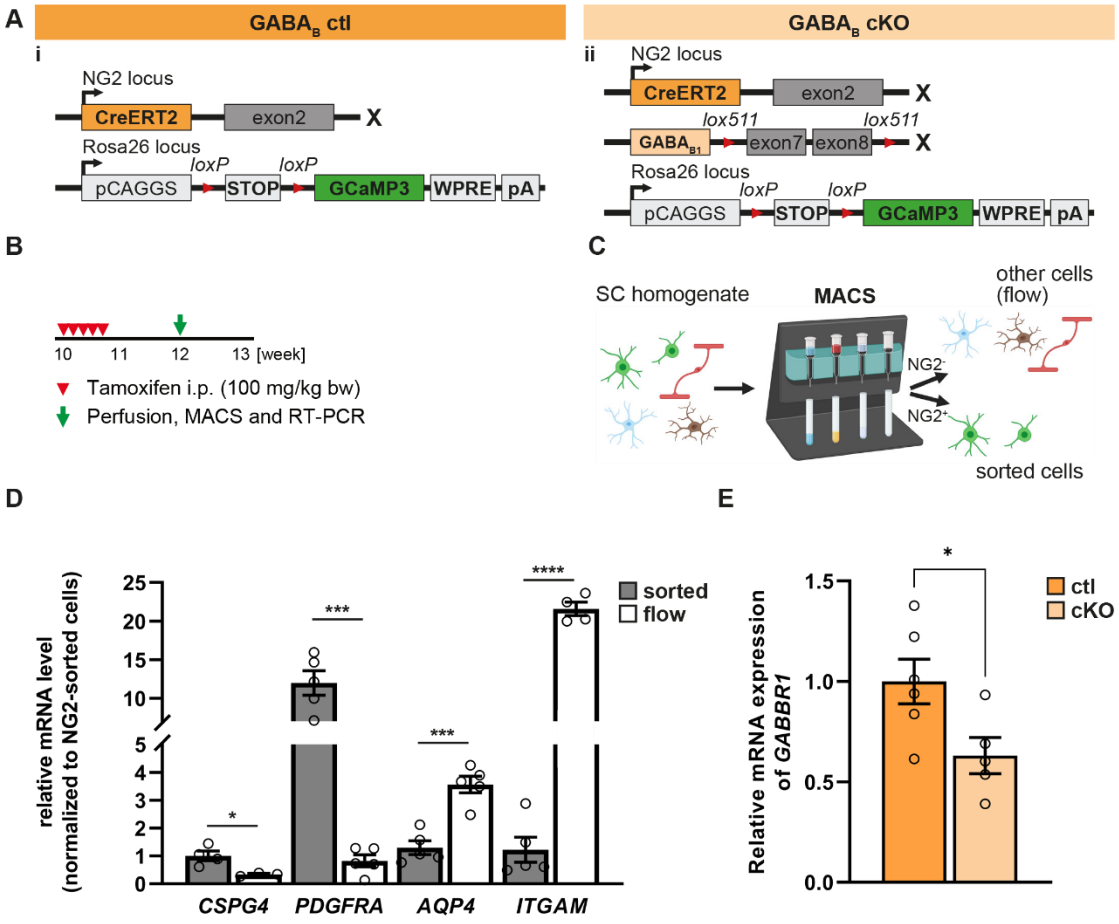

Figure 13: Relative mRNA expression of the metabotropic $GABA_B$ receptor subunit B1 is reduced in the conditional $GABA_B$ knockout.

The control mouse line ($NG2^{GCaMP3}$; **Ai**) was crossed with a $GABA_B^{fl/fl}$ mouse line (**Aii**). Using MACS from spinal homogenate (**B**), a purity check of sorted NG2 glia (OPCs) was performed by RT-PCR two weeks after tamoxifen administration (**C-D**). A reduction in relative *GABABR1* mRNA expression in cKO mice was detected by RT-PCR (**E**). N = 5-6, the mean ± SEM are shown and compared using unpaired t-test. *p <0.05, **p <0.01, ***p <0.001, ****p <0.0001.

6.6 $GABA_B$ RECEPTOR LOSS IN OPCS DOES NOT ALTER THEIR RECOMBINATION AND DIFFERENTIATION CAPACITY IN SPINAL TISSUE

To be able to determine the influence of $GABA_B$ receptor in OPCs (NG2 glia) on their recombination efficiency, specificity, and on oligodendroglial lineage (OL) differentiation, quantitative analysis of immunohistochemical staining was performed in white matter spinal cord tissue. For this purpose, $NG2^{GCaMP3}$ (ctl) and $NG2^{GCaMP3}$ x $GABA_B^{fl/fl}$ (cKO) mice were treated with tamoxifen five times at ten weeks of age to induce recombination. At time G1, mice were transcardially fixed with PFA, followed by spinal cord dissection and vibratome sections immunohistochemically stained. Subsequent quantitative analysis was performed by counting stained cells of the OL.

For the immunohistochemistry, GFP^+ cells (GCaMP3; **Figure 14Ai**), $PDGFR\alpha^+$ cells (OPCs; **Figure 14Aii**) and $MyRF^+$ cells (mature oligodendrocytes (myelin regulatory factor); **Figure 14Aiii**) were analyzed in order to quantify proportion and cell density of OPCs, recombined OPCs ($PDGFR\alpha^+/GFP^+$ cells), and mature oligodendrocytes as well as recombined mature oligodendrocytes ($MyRF^+/GFP^+$ cells). The recombination efficiency in OPCs (**Figure 14B**) in the cKO (81.93 ± 3.48 %) was found to be as high as in the ctl (82.33 ± 5.38 %) shown earlier (Figure 8Fii). The recombination specificity (**Figure 14C**) tended to be lower in the cKO (86.10 ± 1.00 %) than in the ctl (90.43 ± 3.96 %). Quantification of recombined mature oligodendrocytes also demonstrated no difference between ctl and cKO. Thus, the recombination efficiency (**Figure 14D**) was comparably low in ctl (2.69 ± 0.69 %) and cKO (3.08 ±0.91 %), as was the recombination specificity (ctl: 13.06 ± 4.38 %; cKO: 13.45 ± 2.62 %; **Figure 14E**). A closer look at the cell density of OPCs (ctl: 45.65 ± 2.95 cells/10^{-3} mm^3; cKO: 47.57 ± 2.30 cells/10^{-3} mm^3; **Supplementary Figure 3A**), recombined OPCs (ctl: 37.48 ± 2.96 cells/10^{-3} mm^3; cKO: 38.68 ± 2.55 cells/10^{-3} mm^3; **Supplementary Figure 3B**), mature oligodendrocytes (ctl: 184.50 ± 9.64 cells/10^{-3} mm^3; cKO: 213.70 ± 20.43 cells/10^{-3} mm^3; **Supplementary Figure 3C**), and recombined mature oligodendrocytes (ctl: 5.05 ± 1.38 cells/10^{-3} mm^3; cKO: 6.17 ± 1.32 cells/10^{-3} mm^3; **Supplementary Figure 3D**) also revealed no differences between ctl and cKO mice.

In summary, the loss of the $GABA_B$ receptor in OPCs has no effect on recombination efficiency and specificity for the OL. The cell number of OPCs and mature oligodendrocytes was also unchanged in the cKO. The number of mature oligodendrocytes was fourfold higher than for OPCs (ctl and cKO) but in total showed a higher ratio for recombined OPCs than mature oligodendrocytes.

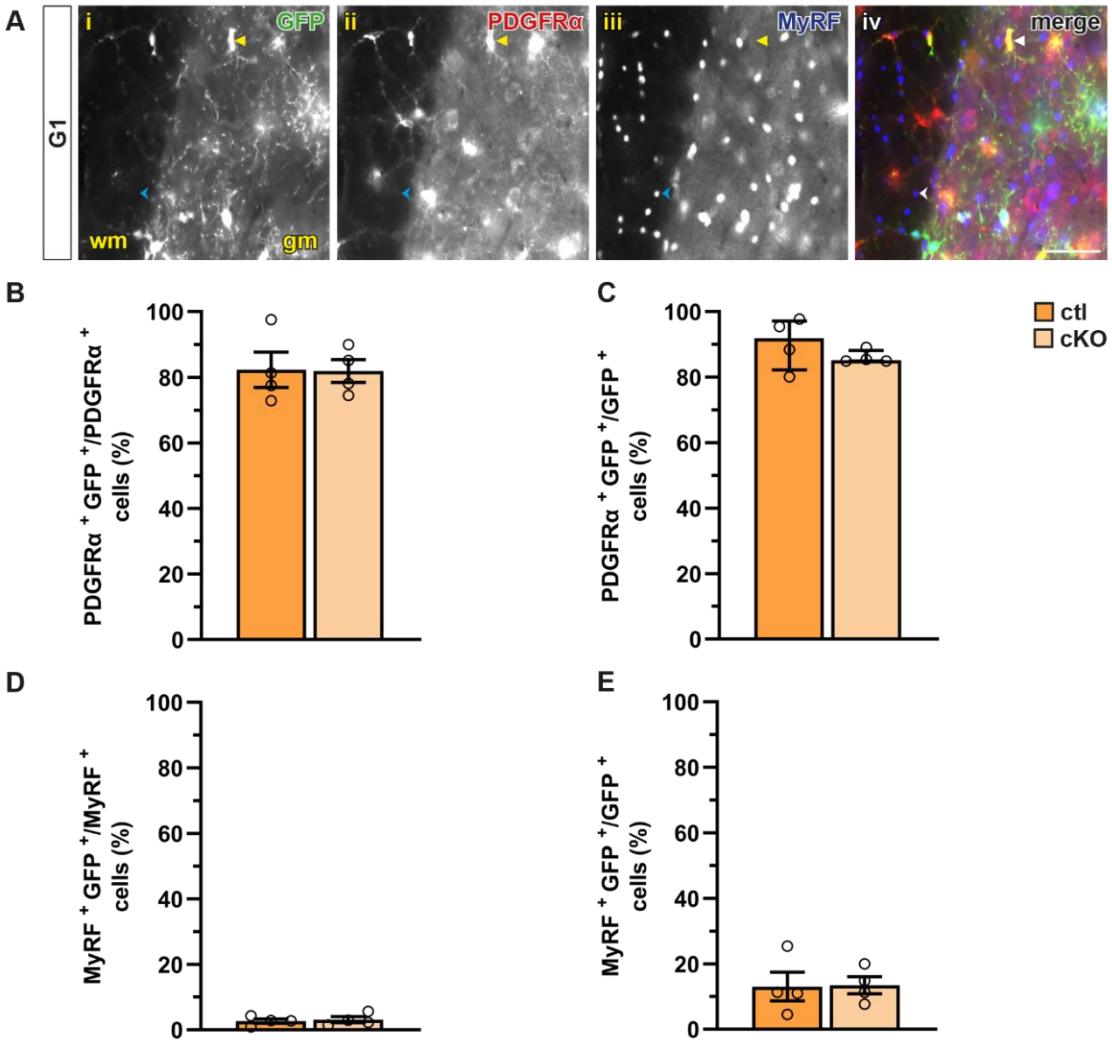

Figure 14: Recombination efficiency and specificity of OL remains unchanged by $GABA_B$ cKO in OPCs.

Three weeks after tamoxifen-induced recombination, cell type-specific staining by immunohistochemistry is shown for GCaMP3 (**Ai**), PDGFRα⁺ OPCs (**Aii**), MyRF⁺ mature oligodendrocytes (**Aiii**), and as an overlay (**Aiv**) to identify recombination for OPCs (yellow arrow) and nonrecombined mature oligodendrocytes (blue arrow) in white (wm) and gray matter (gm). The recombination efficiency and specificity percentages of white matter are shown for ctl and cKO in OPCs (**B-C**), as well as for mature oligodendrocytes (**D-E**). N = 4, n = 32 ROIs from 16 slices showing mean ± SEM. Scale bar = 50 µm**.**

6.7 THE $GABA_B$ RECEPTOR LOSS IN OPCS ALTERS MYELIN STRUCTURE IN THE SPINAL CORD

OPCs are seen as a reservoir for mature oligodendrocytes. As they can differentiate and serve as a pool for a livelong myelination, the formation of myelin characteristic of white matter was compared between ctl and cKO mice. Here, the spinal cord of ctl and cKO mice was immunohistochemically stained at 12 weeks of age (G1) as previously described. In this case, myelin, degraded myelin, and axon markers were used and their fluorescence

intensity was measured. In addition, not only overview images were obtained with the slide scanner but also magnified images with a cLSM to determine the level of the myelin sheaths.

To assess myelin levels, one of the major myelin proteins myelin basic protein (MBP; **Figure 15Ai-ii**) was stained and combined with neurofilament, the key structure-determining protein for axons (NF; **Figure 15Aiii**), comparing ctl (**Figure 15Ai-iv**) and cKO (**Figure 15Av-viii**) mice. First, immunohistochemistry in overview images of transverse spinal cord sections by fluorescence intensity analysis normalized to DAPI showed no change between ctl and cKO for NF in white (ctl: 3.74 ± 0.18; cKO: 3.24 ± 0.20; **Figure 15B**) and gray matter (**Supplementary Figure 4B**). Second, analysis of the MBP fluorescence intensity in white matter (**Figure 15C**) showed a reduction (p-value = 0.0206) in cKO (4.98 ± 0.10) compared with ctl (5.98 ± 0.23) mice indicating impaired myelin formation in the cKO. For further analysis of myelin quality, fluorescence intensity of degraded MBP (dMBP) was quantified (**Supplementary Figure 4A**), with no difference between ctl and cKO in contrast to MBP. Next, the quality of the myelin sheaths was investigated (**Figure 15D**). For this purpose, higher resolution images of the ventral white matter were acquired with cLSM. These were then overlaid with a grid (10 x 10 μm^2) and random myelin sheaths that were under a coordinate overlay were selected for analysis. The ratio was finally calculated from the area of the inner myelin ring and the outer myelin ring, but no difference between ctl (0.25 ± 0.02) and cKO (0.21 ± 0.01) was detected.

The results provided information about the amount of myelin three weeks after induction of the $GABA_B$ cKO in OPCs maturing to myelinating oligodendrocytes, leading to reduced MBP in cKO mice that was not degraded and did not affect myelin sheath quality. Furthermore, axons were not affected by cKO in either white or gray matter.

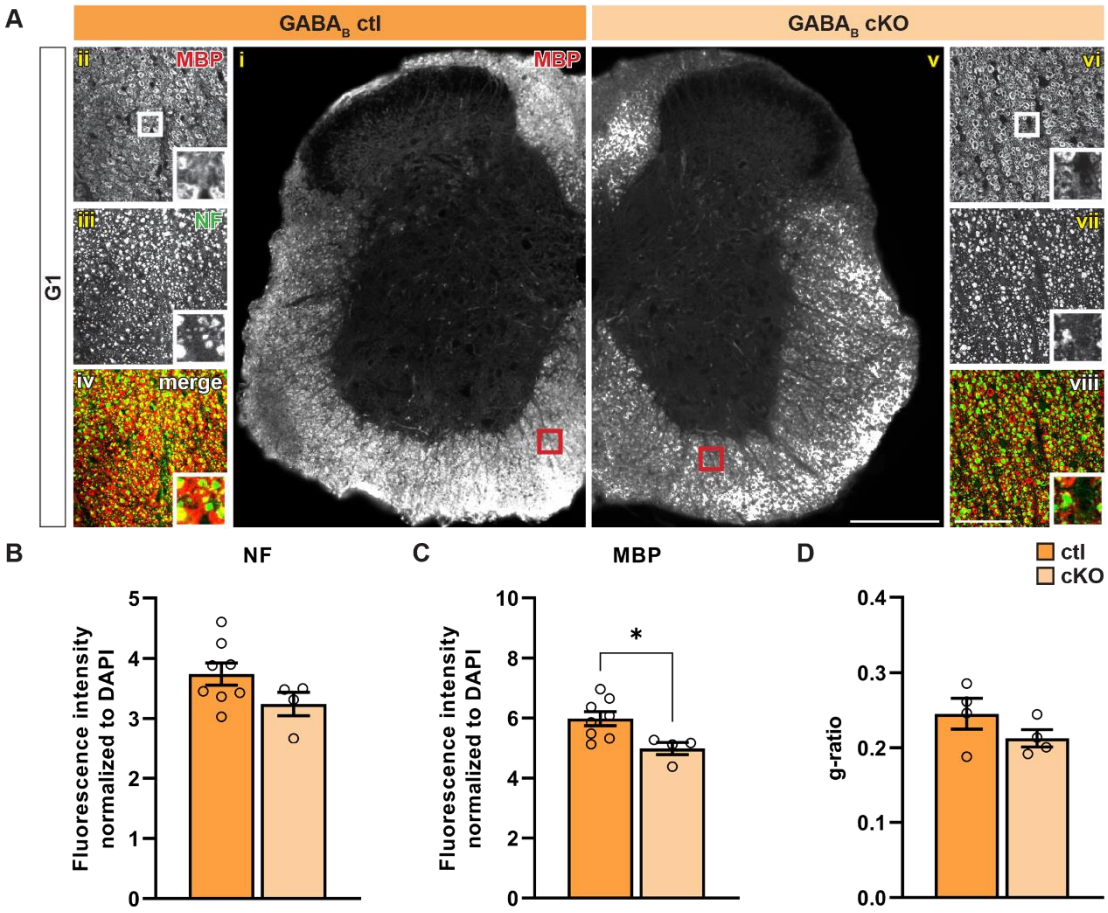

Figure 15: MBP reduction in GABA$_B$ cKOs.

Myelin amount by MBP as overview image (**Ai/Av**), along with cLSM and magnification image of ventral white matter (**Aii/Avi**) combined with axonal NF (**Aiii/Avii**) and superimposed (**Aiv/Aviii**) in transverse spinal cord sections of ctl (**Ai-iv**) and cKO mice **(Av-viii**). Fluorescence intensity analysis normalized to DAPI showed no difference between ctl and cKO for NF (**B**), but a reduction for MBP in cKO (**C**) and no difference in myelin sheath thickness (**D**). N = 4-8, n = 96 ROIs from 48 slices in case for fluorescence intensity and n = 128 ratios from 32 slices in case for g-ratio measurements. The mean ± SEM are shown and compared using unpaired t-test. *p <0.05. Scale bar = 200 µm (v) and 50 µm (viii).

6.8 GABA$_B$ RECEPTOR LOSS DOES NOT INFLUENCE CELL PROLIFERATION OF RECOMBINED OPCS AND GLIOSIS

To investigate the effect of the GABA$_B$ loss in OPCs on their cell physiology and neighboring glial cells in the white matter of the spinal cord, the proliferation of the recombined OPCs, as well as the response of microglia and astroglia, was further examined.

For this purpose, cKO mice were collected at time G1 compared with ctl as previously described and evaluated by immunohistochemistry. To determine the proliferation rate, recombined cells (as already shown, OPCs in the majority (Figure 14)) were labeled with GFP (**Figure 16Ai**) and proliferating cells with Ki67 (**Figure 16Aii**), which is expressed

during the cell cycle in every phase except the resting phase. For analysis of immune response by microglia, Iba1 (**Figure 16D1**) was stained as a marker and cell number was determined.

The fluorescence intensity for GFAP (**Figure 16Dii**) was determined to quantify astrogliosis. The number of recombined proliferating OPCs (**Figure 16B**) was not significantly increased in the cKO (1.59 ± 0.13 cells/10^{-3} mm^3) than the ctl (1.12 ± 0.32 cells/10^{-3} mm^3). Similarly, the ratio of recombined proliferating OPCs among all proliferating cells (**Figure 16C**) also tended to be higher in the cKO (ctl: 49.19 ± 11.10 %; cKO: 60.67 ± 12.00 %). The cell numbers of $Iba1^+$ microglia (**Figure 16E**), collected as another assay, also revealed no difference between ctl (30.11 ± 3.21 cells/10^{-3} mm^3) and cKO (29.07 ± 1.38 cells/10^{-3} mm^3). Fluorescence intensity measurement of the astroglial marker GFAP normalized to DAPI (**Figure 16F**) likewise showed only a tendency toward increased fluorescence intensity in cKO (ctl: 1.26 ± 0.08; cKO: 1.57 ± 0.17).

In conclusion, the $GABA_B$ receptor loss in OPCs had no effect on the proliferation of recombined OPCs and the proportion of these in all dividing cells in the spinal cord was not changed in cKO mice. The effect of the receptor loss on the other glial cells showed no change in the number of microglia and likewise no change in astroglia, indicating unchanged physiological interplay of these three glial cells without evidence of gliosis.

Figure 16: Induction of $GABA_B$ receptor loss in OPCs does not lead to altered proliferation in recombined OPCs, nor to gliosis.

Shown are recombined GFP^+ cells (**Ai**), proliferating $Ki67^+$ cells (**Aii**) in combination with DAPI (**Aiii**) and as an overlay (**Aiv**; yellow arrow), the number of recombined and proliferating OPCs (**B**), as well as the ratio of those to all dividing cells (**C**) between ctl and cKO. Iba^+ microglia (**Di**) and $GFAP^+$ astroglia (**Dii**) with DAPI (**Diii**) as an overlay (**Div**) to analyze microglia number (**E**) and astrogliosis by fluorescence intensity (**F**) with no difference between ctl and cKO. N = 4-8, n = 32 ROIs from 16 slices for cell counting and n = 96 ROIs from 48 slices for fluorescence intensity measurement, showing mean ± SEM. Scale bar = 20 µm.

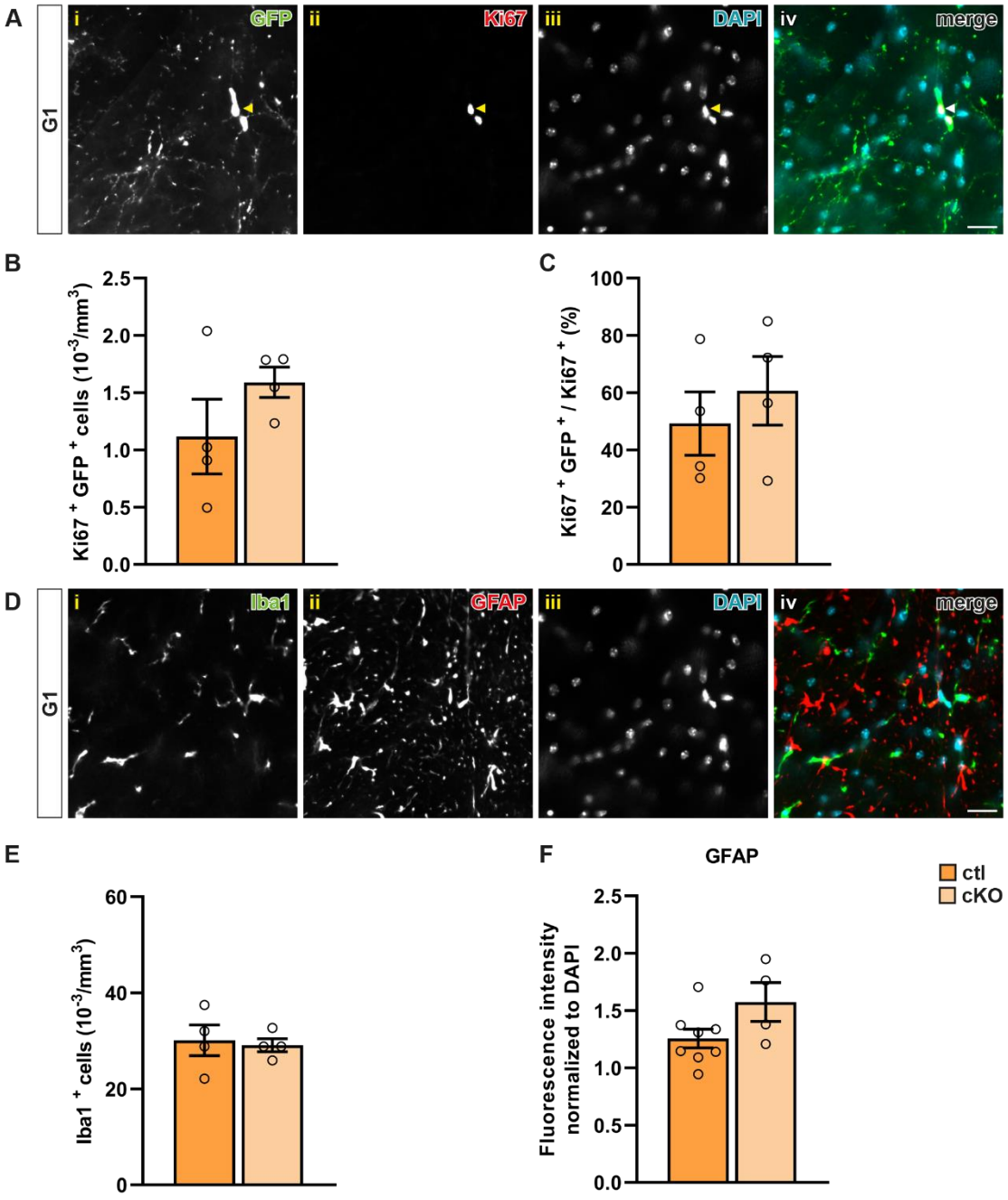

6.9 Ca^{2+} SIGNALS ARE ATTENUATED BY $GABA_B$ RECEPTOR LOSS IN OPCS

As the $GABA_B$ receptor is thought to influence the intracellular Ca^{2+} balance of OPCs, the GCaMP3 data from $NG2^{CaMP3}$ ctl mice were compared with *in vivo* 2P-LSM data from $NG2^{GCaMP3}$ x $GABA_B^{fl/fl}$ cKO mice to investigate the influence of $GABA_B$ receptor loss on several parameters of spontaneous Ca^{2+} fluctuations.

For this purpose, mice were treated with tamoxifen to induce recombination and cKO, as previously described at 10 weeks of age. Two weeks later and one week after placement of the spinal cord window (at time point G1, d7), spontaneous Ca^{2+} activity in ctl and cKO

mice was recorded by 2P-LSM and analyzed with MSparkles. The cell morphology revealed by GCaMP3 was of finely structures and cell typical in both conditions. The detected ROAs appeared to be larger in cKO, the activity in the heat maps was comparable (**Figure 17A**). Analysis of Ca^{2+} activity revealed a reduction (p-value = 0.0034) in signal density in cKOs (ctl: 8.05 ± 0.91 x 10^{-3} µm^2; cKO: 2.00 ± 0.53 x 10^{-3} µm^2; **Figure 17B**), as well as decreased (p-value = 0.0416) ROA density (ctl: 0.76 ± 0.08 x 10^{-3} µm^2; cKO: 0.41 ± 0.11 x 10^{-3} µm^2; **Figure 17C**) and a lower (p-value = 0.0030) coincidence index (ctl: 0.16 ± 0.01; cKO: 0.09 ± 0.10; **Figure 17D**). For the area of the ROAs (ctl: 24.63 ± 4.68 µm^2; cKO: 22.11 ± 4.35 µm^2; **Figure 17E**), the signal amplitude (ctl: 0.18 ± 0.02 $\Delta F/F_0$; cKO: 0.17 ± 0.03 $\Delta F/F_0$; **Figure 17F**) and signal duration (ctl: 3.24 ± 0.29 s; cKO: 3.90 ± 0.45 s; **Figure 17G**) no differences between ctl and cKO could be detected. The additionally collected signal parameters for signal frequency, integrated fluorescence, mean fluorescence, and signal rise and decay time showed no difference between ctl and cKO (**Supplementary Figure 5**).

Thus, compared to the ctl, cKO mice have fewer signals in less active regions that are also less coincidentally active. In parallel, the temporal parameters such as signal duration, frequency and amplitude, as well as the spatial extent were not affected.

$GABA_B$ receptor deletion in OPCs resulted in a reduction of the $GABA_B$ mRNA level, with no effect on recombination, proliferation, or surrounding cells such as axons or gliosis. Nevertheless, a reduction of the myelin protein MBP as well as a decreased Ca^{2+} activity could be detected in cKO mice, which has been considered in more detail in both cases hereafter.

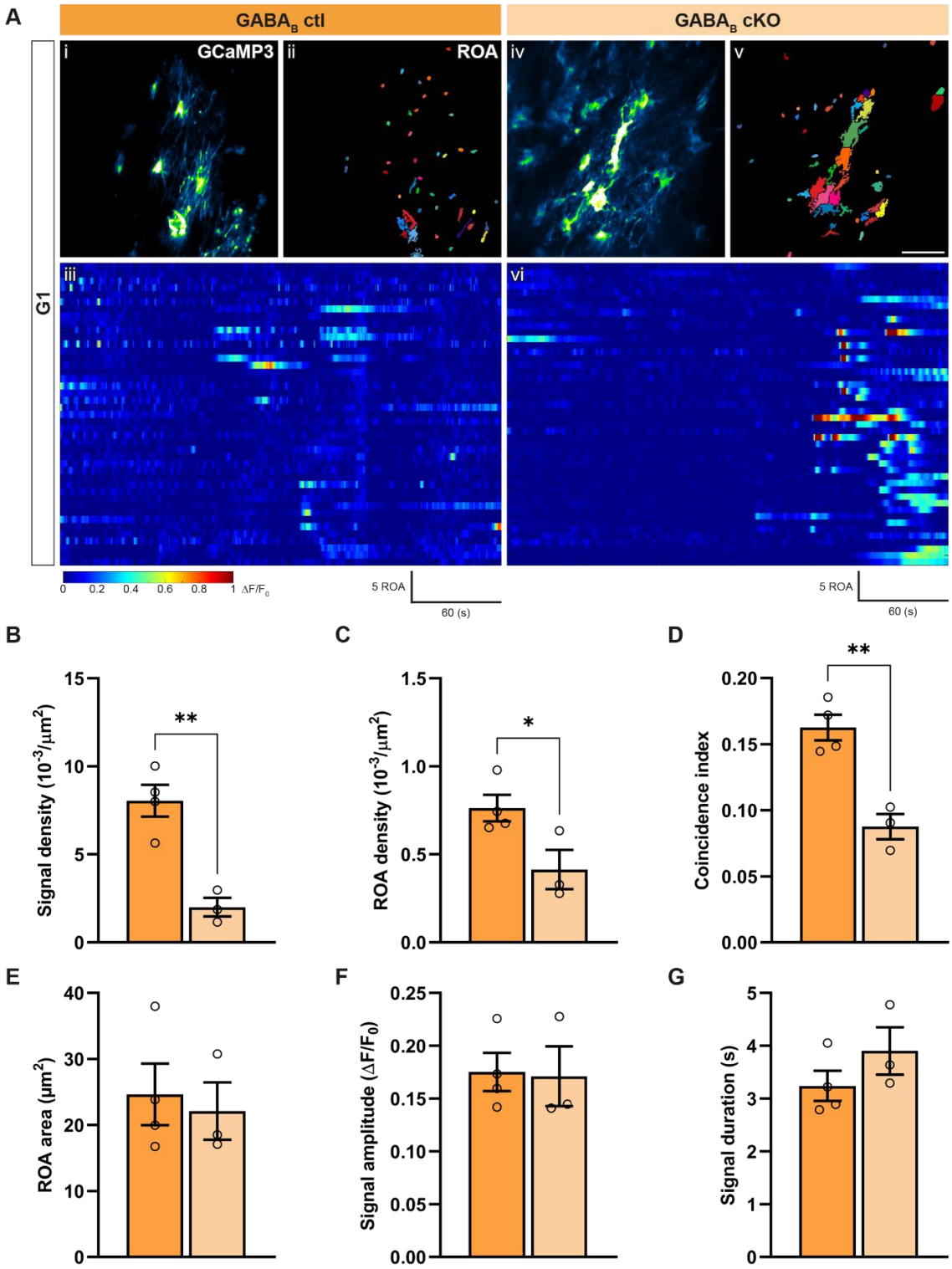

Figure 17: *In vivo* Ca^{2+} signaling of OPCs is impaired in $GABA_B$ cKO mice.

Fluorescence changes of GCaMP3 in $NG2^{GCaMP3+}$ (ctl) and $NG2^{GCaMP3}$ x $GABA_B^{fl/fl}$ (cKO) cells detected by MSparkles (**A**; ctl: i-iii; cKO: iv-vi) at G1. Maximum intensity projection of the image (i/iv), automatically detected ROAs as a color-coded map (ii/v) and the fluorescence change over time of all ROAs as a heatmap (iii/vi). Six parameters signal density (**B**), ROA density (**C**), coincidence index (**D**), ROA area (**E**), signal amplitude (**F**) and signal duration (**G**) show six parameters of the software to separate Ca^{2+} activity seven days after laminectomy between conditions. Scale bar = 50 µm. N = 3-4, the mean or median values ± SEM/IQR from several FOVs (n = 12-16) are shown and compared using ordinary one-way ANOVA or Kruskal-Wallis test. *p <0.05, **p <0.01.

6.10 WEIGHT LOSS IN MICE WITH $GABA_B$ DEPRIVATION AFTER CPZ

OPCs mature into myelinating oligodendrocytes whose myelination capacity is Ca^{2+} dependent and a reducing effect in myelin quality, as well as Ca^{2+} activity, has previously been shown in OPCs with $GABA_B$ receptor deprivation in the spinal cord. Comparative studies using a demyelination model have been performed subsequently to be able to elaborate a possible influence on myelin loss.

Cuprizone (CPZ) is used as a toxic demyelination model in mice and leads to weight loss when fed as a diet, which is a definite sign of myelin loss in the CNS (Steelman et al., 2012; Toomey et al., 2021). To verify whether $GABA_B$ cKO in OPCs affects demyelination, ctl and cKO mice were fed CPZ for three weeks two weeks after being treated with tamoxifen five times at ten weeks of age. The diet was provided as a powder and body weight was measured every other day during the diet (**Figure 18**). The mice were fed a dose of 0.3 % CPZ during the first week of the diet, followed by 0.2 % for two weeks and then back to standard chow. Baseline weight before the start of the diet was taken as 100 % for comparison. There was a steeply declining weight loss of more than 10 % already at the beginning of the diet, which stagnated at the end of the first week. This was equally observed for ctl and cKO mice. During the diet phase with 0.2 % CPZ, weight increased slightly in the ctl, whereas it hardly increased in the cKO. On days 13 (ctl: 89.49 ± 0.98 %; cKO: 83.65 ± 3.92 %), 15 (ctl: 89.13 ± 1.25 %; cKO: 81.04 ± 4.07 %), 17 (ctl: 90.88 ± 1.06 %; cKO: 85.12 ± 3.69 %) and 19 (ctl: 91.86 ± 1.04 %; cKO: 84.75 ± 3.06 %), the weight of the cKO remained below (p-value = d13: 0.0235, d15: 0.0019, d17: 0.0257, d19: 0.0061) that of the ctl mice (**Figure 18A**). Separating the ctl animals and looking at weight loss in a sex-specific manner, there were no differences between the sexes (**Figure 18B**). Except for loss of weight, no obvious changes in animal behavior were noted during daily monitoring while on the CPZ diet.

The diet with CPZ for three weeks resulted in weight loss in all mice, which was clearly greater at the beginning in the first third than in the last two thirds. Although weight loss stagnated after the first week, the cKO mice lagged behind the ctl in weight, which would suggest a stronger demyelination effect by $GABA_B$ receptor deletion in OPCs. No sex-related differences were observed.

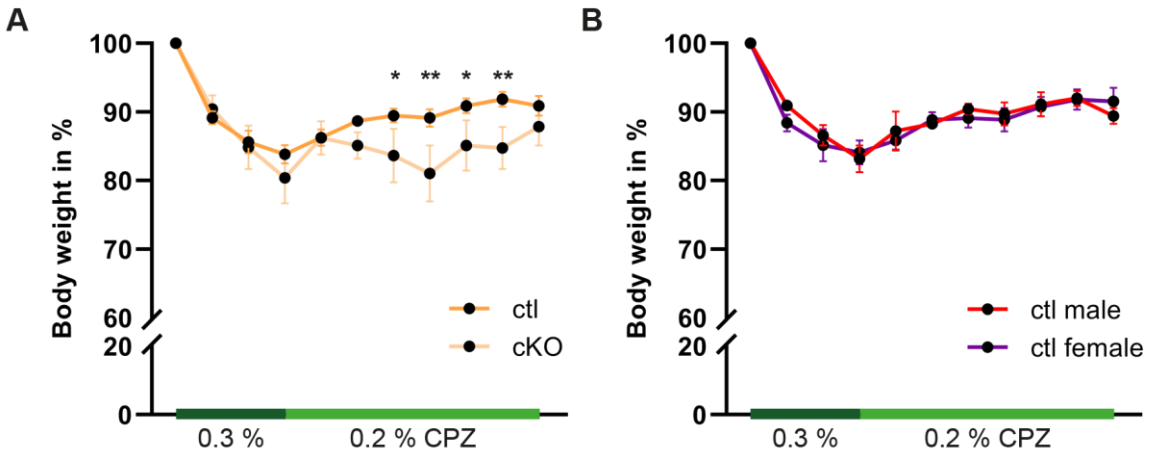

Figure 18: Weight loss due to cuprizone diet is stronger in $GABA_B$ cKO mice.

Shown is baseline weight as 100 % and weight loss measured every other day in percentage while on the diet with CPZ powder one week at 0.3 % followed by two weeks 0.2 % for ctl and cKO mice (**A**), and by sex separated for ctl (**B**). N = 4-10, the mean values ± SEM from 11 days are shown and compared using 2way ANOVA test. *p <0.05, **p <0.01.

6.11 Unchanged recombination in OPCs during demyelination

Furthermore, the recombination efficiency and specificity, as well as the distribution of OL cells in the spinal cord, were examined under influence of the demyelination model in ctl and cKO mice.

For this, two time points were chosen for analysis. As already established, the mice received tamoxifen five times at ten weeks of age and then one group of ctl and cKO mice was treated with CPZ for three weeks starting at 12 weeks of age (G2*) and the other group continued to receive normal chow (G2). Both groups were perfused at 16 weeks of age to evaluate immunohistochemically the effect of demyelination on OL (**Figure 19A-B**). For the recombination efficiency of PDGFRα$^+$ OPCs (**Figure 19C**), similarly high values were found for ctl (77.07 ± 24.44 %) and cKO (86.29 ± 17.78 %) at time point G2 as at time point G2* (ctl: 81.38 ± 10.14 %; cKO: 64.70 ± 19.87 %). Similarly, for ctl and cKO at time point G2 (ctl: 75.62 ± 4.95 %; cKO: 88.20 ± 2.08 %) and G2* (ctl: 78.30 ± 5.33 %; cKO: 83.92 ± 2.07 %) for recombination specificity (**Figure 19D**). No differences were detected in either case. Also very low and without difference remained the number of recombined mature oligodendrocytes (MyRF$^+$; **Figure 19E**) at time point G2 (ctl: 5.18 ± 1.31 %; cKO: 2.43 ± 0.49 %) and G2* (ctl: 3.97 ± 1.04 %; cKO: 2.77 ± 0.32 %), as well as the OL differentiation level (**Figure 19F**) at time points G2 and G2* for ctl (G2: 18.44 ± 1.30 %; G2*: 16.56 ± 3.79 %) and cKO mice (G2: 10.28 ± 1.02 %; G2*: 14.65 ± 1.86 %). Considering cell numbers, there was an increased (p-value = 0.0074) number of mature oligodendrocytes of about 32 % in the cKO at time point G2 (ctl: 198.90 ± 14.89 cells/10^{-3} mm^3; cKO:

278.40 ± 29.69 cells/10^{-3} mm^3; **Supplementary Figure 6A**). This was consistent between ctl and cKO after CPZ treatment (G2*) and was increased (p-value = 0.0252) for ctl compared to G2 (G2: 198.90 ± 14.89 cells/10^{-3} mm^3; G2*: 262.00 ± 5.08 cells/10^{-3} mm^3) of about 28 %. The number of recombined mature oligodendrocytes, the number of OPCs, and the number of recombined OPCs remained unchanged (**Supplementary Figure 6B-D**).

Taken together, neither ctl, nor cKO showed any effect on recombination efficiency or specificity in OPCs and mature oligodendrocytes by doubling the waiting time after tamoxifen-induced recombination or demyelination by CPZ. By contrast, the number of mature oligodendrocytes increased with longer waiting time in the cKO, as well as their number during demyelination in the ctl.

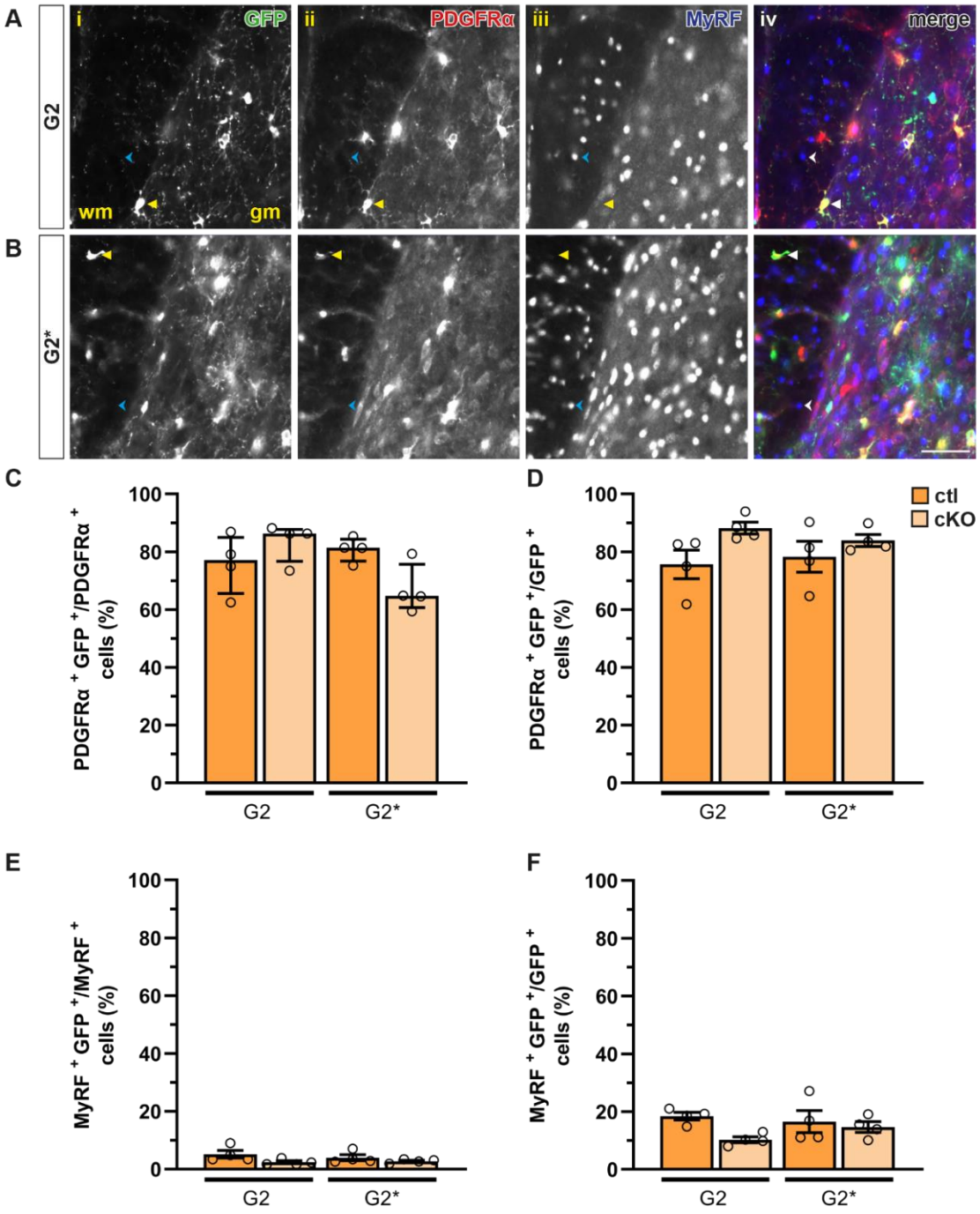

Figure 19: Recombination efficiency and specificity of OL remains unchanged by CPZ induced demyelination.

Six weeks after tamoxifen-induced recombination, cell type-specific staining by immunohistochemistry for GCaMP3 (i), PDGFRα$^+$ OPCs (ii), MyRF$^+$ mature oligodendrocytes (iii), and as an overlay (iv) to identify recombination for OPCs (yellow arrow) and nonrecombined mature oligodendrocytes (blue arrow) in white (wm) and gray matter (gm) without (**A**) and with (**B**) CPZ treatment. The recombination efficiency and specificity percentages of white matter are shown for ctl and cKO in OPCs (**C-D**), as well as the subsequent differentiation to mature oligodendrocytes (**E-F**). N = 4, n = 32 ROIs from 16 slices showing mean or median ± SEM/IQR. Scale bar = 50 µm.

6.12 OPC SPECIFIC DELETION OF $GABA_B$ RECEPTOR WITH PROTECTIVE EFFECT ON SPINAL DEMYELINATION

To examine the rate of demyelination in the white matter of the spinal cord and the direct effect of CPZ on myelin levels, axons and myelin were quantitatively evaluated by immunohistochemistry as previously described.

Two groups at 16 weeks of age, treated as G2 without and G2* with CPZ, were stained with antibodies against NF and MBP at the age of 16 weeks (**Figure 20A-B**), and fluorescence intensity normalized to DAPI in white matter was evaluated. In addition, cLSM recordings of transversal sections were again used to evaluate the thickness of myelin sheaths also in the demyelination phase here. Fluorescence intensity measurement of the axon marker NF (**Figure 20C**) did not reveal differences between ctl and cKO in either G2 (ctl: 3.25 ± 0.32; cKO: 3.47 ± 0.20), or G2* (ctl: 2.62 ± 0.18; cKO: 3.32 ± 0.43). But for MBP evaluation (**Figure 20D**), a reduction in the fluorescence intensity of ctl mice by 1.5-fold could be found (p-value = 0.0009) between G2 (ctl: 6.30 ± 0.50; cKO: 6.02 ± 0.71) and G2* (ctl: 4.18 ± 0.20; cKO: 5.08 ± 0.37), whereas cKO barely changed. The myelin sheaths recorded by cLSM were then measured for their area and to be able to calculate the ratio between inner and outer ring (**Figure 20E**). The ratio between ctl and cKO was unchanged at time point G2 (ctl: 0.20 ± 0.01; cKO: 0.18 ± 0.01), but increased for ctl versus cKO (p-value = 0.0222) at time point G2* (ctl: 0.29 ± 0.03; cKO: 0.22 ± 0.02). Also, increased was the ratio of ctl comparing G2 and G2* (p-value = 0.0070). No difference was observed in the fluorescence intensity of degraded MBP or NF in gray matter between ctl or cKO with and without CPZ treatment (**Supplementary Figure 7**).

In conclusion, axons in neither white nor gray matter were affected by demyelination and only in ctl mice a strong MBP reduction was detected, whereas the mice with cKO of the $GABA_B$ receptor in OPCs hardly underwent MBP loss. The additional determination of myelin sheath thickness, using high magnification confocal images, showed a marked increase in the area ratio between the inner and outer rings in ctl mice due to demyelination, indicating thinner myelin sheath ring, which was not the case in cKO.

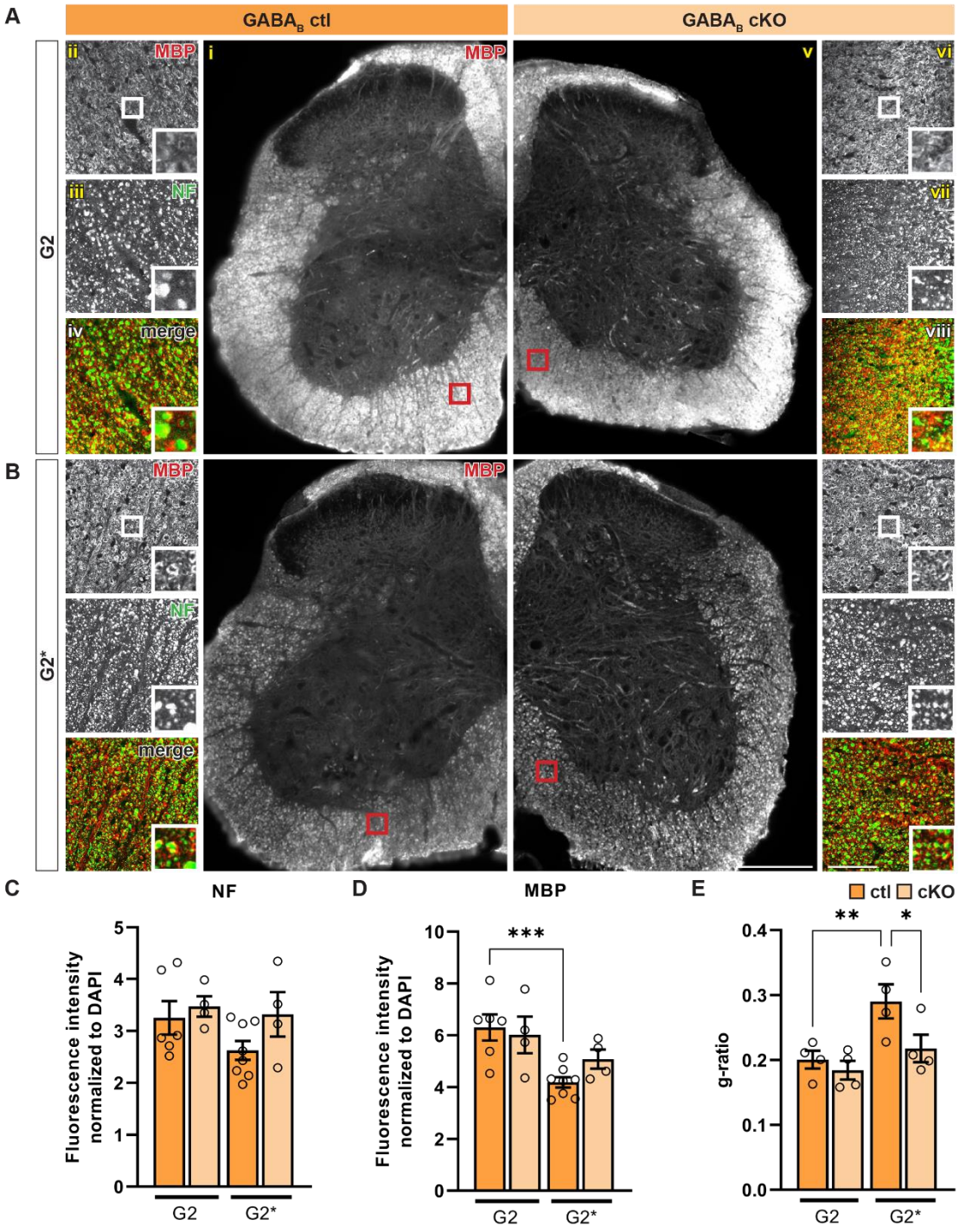

Figure 20: MBP reduction in CPZ demyelination is rescued by GABA$_B$ receptor loss in OPCs.

Myelin quality by MBP as overview image (i/v), along with cLSM and magnification image of ventral white matter (ii/vi) combined with axonal NF (iii/vii) and as superimposed (iv/viii) in transverse spinal cord sections of ctl (i-iv) and cKO mice (v-viii) for G2 (**A**) and G2* (**B**). Fluorescence intensity analysis normalized to DAPI with no difference between ctl and cKO for NF (**C**), but a reduction for MBP in ctl by demyelination (**D**) and loss in myelin sheath thickness (**E**). N = 4-8, n = 96 ROIs from 48 slices in case for fluorescence intensity and n = 128 ratios from 32 slices in case for g-ratio measurements. The mean ± SEM are shown and compared using one-way ANOVA. *p <0.05, **p <0.01, ***p <0.001. Scale bar = 200 µm (v) and 50 µm (viii).

6.13 CUPRIZONE INDUCED DEMYELINATION DOES NOT AFFECT PROLIFERATION OF RECOMBINED OPCS OR GLIOSIS

Further, the influence of demyelination by CPZ on the proliferation of recombined OPCs was subsequently investigated and evaluated by immunohistochemistry using the proliferation marker Ki67 as previously described. Gliosis due to demyelination was also investigated with the markers Iba1 for microglia and GFAP for astroglia.

For both groups G2 and G2*, the recombined GFP^+ cells and proliferating $Ki67^+$, as well as $DAPI^+$ cells were quantified, respectively (**Figure 21A-B**). No difference was detected for either ctl or cKO mice at time points G2 (ctl: 2.88 ± 6.80 cells/10^{-3} mm^3; cKO: 1.87 ± 1.60 cells/10^{-3} mm^3) and G2* (ctl: 3.37 ± 3.85 cells/10^{-3} mm^3; cKO: 1.53 ± 1.18 cells/10^{-3} mm^3) in the number of recombined and proliferating OPCs (**Figure 21C**). Furthermore, no difference was detected in the proportion of recombined dividing OPCs among all proliferating cells at time points G2 (ctl: 33.27 ± 12.43 %; cKO: 30.63 ± 7.94 %) and G2* (ctl: 24.27 ± 7.64 %; cKO: 44.69 ± 10.03 %; **Figure 21D**). Of note, the data distribution was very variable in both cases.

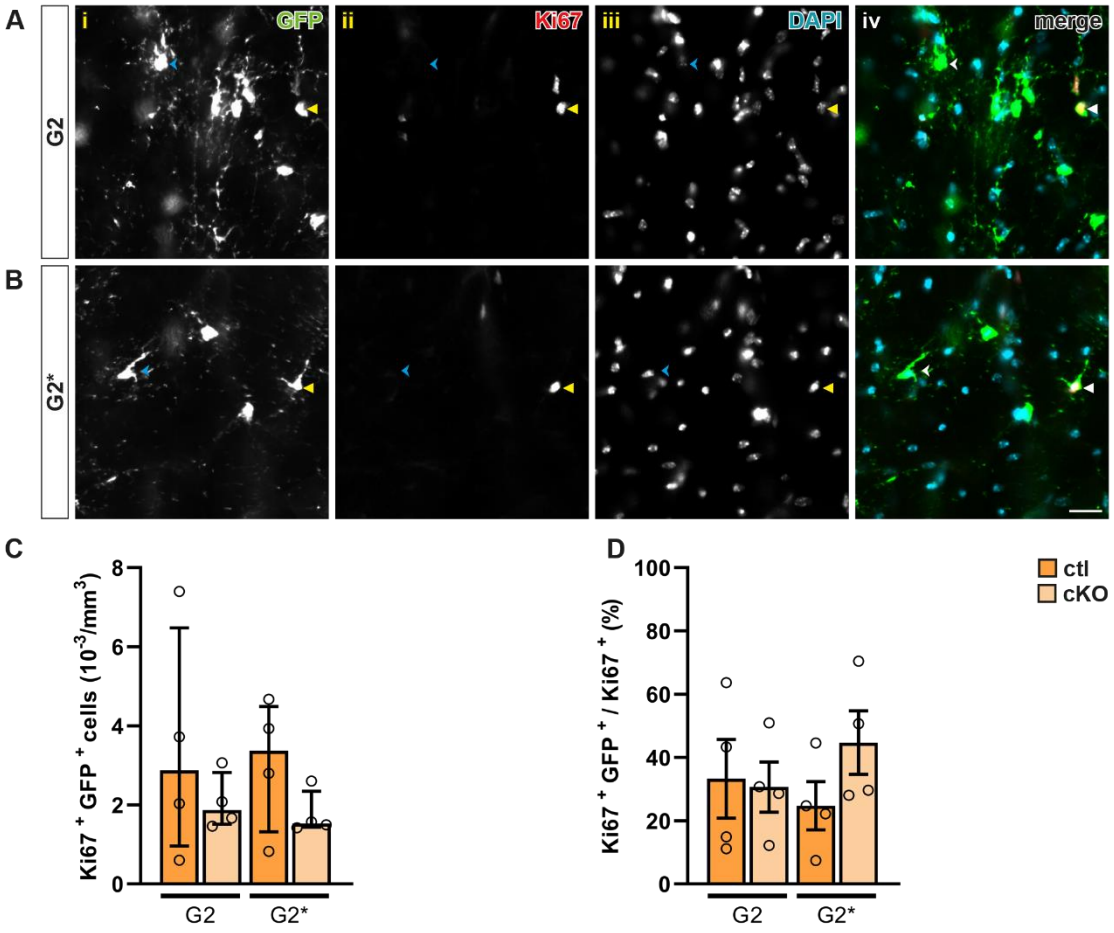

Figure 21: Demyelination does not lead to altered proliferation in recombined OPCs.

Recombined GFP$^+$ cells (i), proliferating Ki67$^+$ cells (ii) in combination with DAPI (iii) and as an overlay (iv; yellow arrow) for G2 (**A**) and G2* (**B**) treated mice respectively. No difference in recombined and proliferating OPCs (**C**), as well as the ratio of those to all dividing cells (**D**) between ctl and cKO after demyelination. N = 4, n = 32 ROIs from 16, showing mean or median ± SEM/IQR. Scale bar = 20 µm.

To verify whether demyelination in the spinal cord leads to gliosis, the cell number of Iba1$^+$ microglia and the fluorescence intensity of GFAP$^+$ astroglia were evaluated (**Figure 22A-B**). Here, as for proliferation rate, no clear differences for ctl and cKO mice at time points G2 (ctl: 48.05 ± 16.98 cells/10^{-3} mm^3; cKO: 35.40 ± 10.57 cells/10^{-3} mm^3) and G2* (ctl: 42.76 ± 8.65 cells/10^{-3} mm^3; cKO: 43.72 ± 16.34 cells/10^{-3} mm^3) for the number of microglia (**Figure 22C**) could be found. Whereas sporadic accumulation clusters of microglial cells (**Figure 22Ai**) could be identified. However, also for the fluorescence intensity of GFAP normalized to DAPI no difference could be detected (**Figure 22D**), only a tendency for the fluorescence intensity was found in astroglia of ctl compared to cKO for G2 (ctl: 1.95 ± 1.02; cKO: 1.451 ± 0.33) and G2* (ctl: 1.83 ± 1.47; cKO: 1.42 ± 1.15).

Therefore, demyelination did not affect the proliferation rate of recombined OPCs or the proportion of all dividing cells in the white matter of the spinal cord. And an immune response induced by demyelination through microglia accumulation could not be confirmed, nor could an activation of astroglia induced by CPZ.

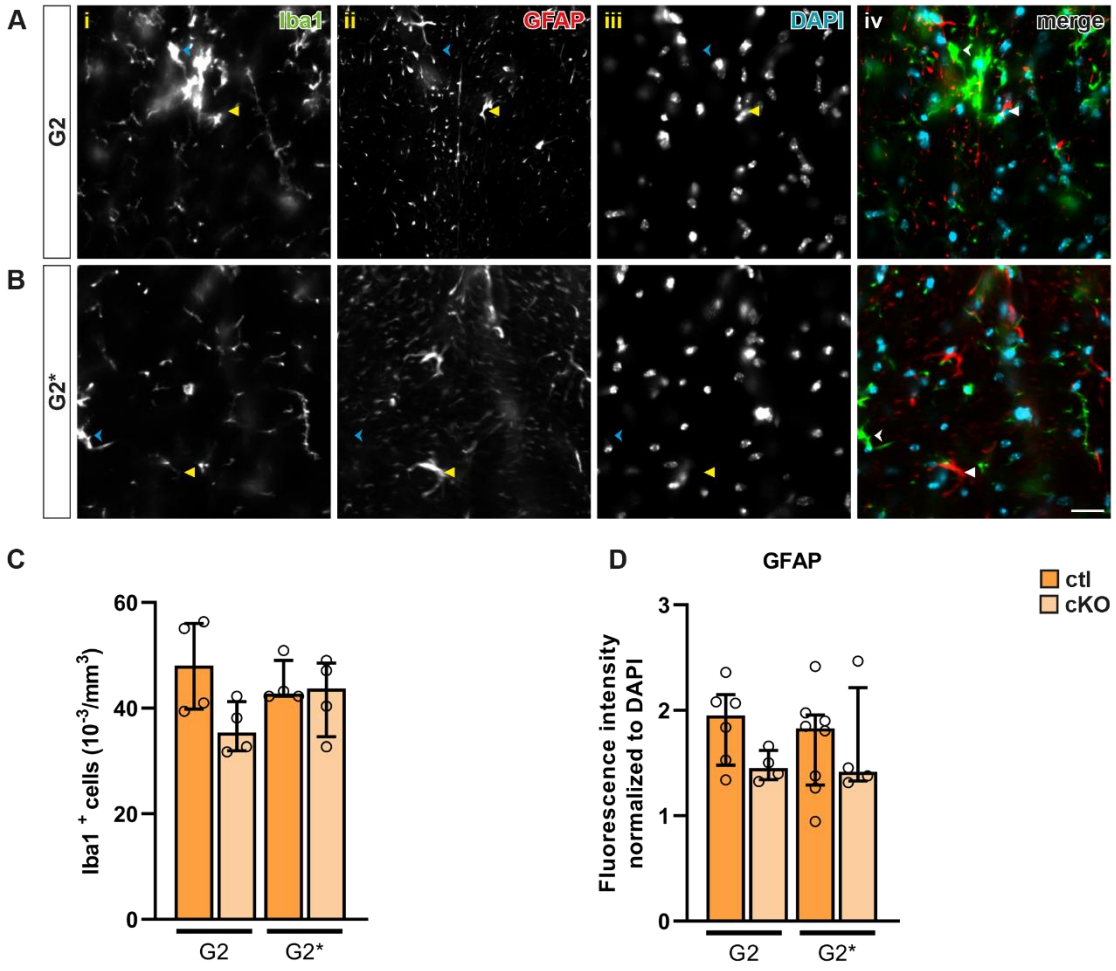

Figure 22: Demyelination does not lead to gliosis by microglia or astroglia in the spinal cord.

Recombined Iba1⁺ microglia (i), GFAP⁺ astroglia (ii) in combination with DAPI (iii) and as an overlay (iv; yellow arrow) for G2 (**A**) and G2* (**B**) to analyze microglia number (**C**) and astrogliosis by fluorescence intensity (**D**). N = 4-8, n = 128 ROIs from 64 slices for cell counting and n = 176 ROIs from 88 slices for fluorescence intensity measurement, showing median ± IQR. Scale bar = 20 µm.

6.14 Ca^{2+} SIGNALS IN OPCS ARE LESS AFFECTED BY DEMYELINATION THAN BY LOSS OF THE $GABA_B$ RECEPTOR

As a final point, Ca^{2+} activity in OPCs with and without reduction of the $GABA_B$ receptor was examined in the context of demyelination in the spinal cord to give an indication of their cellular activity. For this purpose, a spinal cord window was implanted at 15 weeks of age and spontaneous Ca^{2+} activity was recorded by 2P-LSM, CPZ-ctl group G2 and immediately after CPZ treatment in group G2* for one week. Analyzed was the end point one week after diet.

The images of the G2 and G2* groups each showed different Ca^{2+} activity after detection with MSparkles and a variable dispersion of activity distributed over the active regions (**Figure 23A-B**). Signal density (**Figure 23C**) was increased in the cKO (p-value = 0.0051) at time point G2 (ctl: 3.03 ± 0.79 x 10^{-3} µm^2; cKO: 10.71 ± 2.02 x 10^{-3} µm^2), whereas at time point G2* this only trended (ctl: 7.64 ± 1.83 x 10^{-3} µm^2; cKO: 11.33 ± 1.59 x 10^{-3} µm^2). The result was similar for the ROA density (**Figure 23D**), where a difference (p-value = 0.0462) was only present within G2 (ctl: 0.53 ± 0.09 x 10^{-3} µm^2; cKO: 1.02 ± 0.11 x 10^{-3} µm^2), but not at G2* (ctl: 0.76 ± 0.04 x 10^{-3} µm^2; cKO: 1.15 ± 0.18 x 10^{-3} µm^2). The coincidence index (**Figure 23E**) was also increased in cKO (p-value = 0.0146) at time point G2 (ctl: 0.10 ± 0.02; cKO: 0.18 ± 0.02), whereas no difference between cKO and ctl at time point G2* (ctl: 0.18 ± 0.02; cKO: 0.17 ± 0.02), but an increase for ctl compared to G2 (p-value = 0.0206) were found. The sizes of the ROA area (**Figure 23F**) were highest in the ctl in G2 (ctl: 52.41 ± 17.92 µm^2; cKO: 19.04 ± 1.87 µm^2), but without significance and without difference to G2* (ctl: 17.33 ± 2.33 µm^2; cKO: 17.16 ± 1.38 µm^2). The signal amplitude (**Figure 23G**) was highest in the ctl (p-value = 0.0167) at time G2 (ctl: 0.26 ± 0.04 $\Delta F/F_0$; cKO: 0.15 ± 0.01 $\Delta F/F_0$) and again no difference for G2* (ctl: 0.15 ± 0.01 $\Delta F/F_0$; cKO: 0.15 ± 0.01 $\Delta F/F_0$) was found, but a reduction for the ctl compared to G2 (p-value = 0.0155). For the duration of the signals (**Figure 23H**), the ctl tended to be highest in G2 (ctl: 4.14 ± 0.88 s; cKO: 2.81 ± 0.08 s) and G2* (ctl: 3.42 ± 0.96 s; cKO: 2.64 ± 0.10 s) only. No demyelination-related difference in signal frequency, integrated fluorescence, mean fluorescence, signal rise and decay time could be detected in the additional parameters collected (**Supplementary Figure 8**).

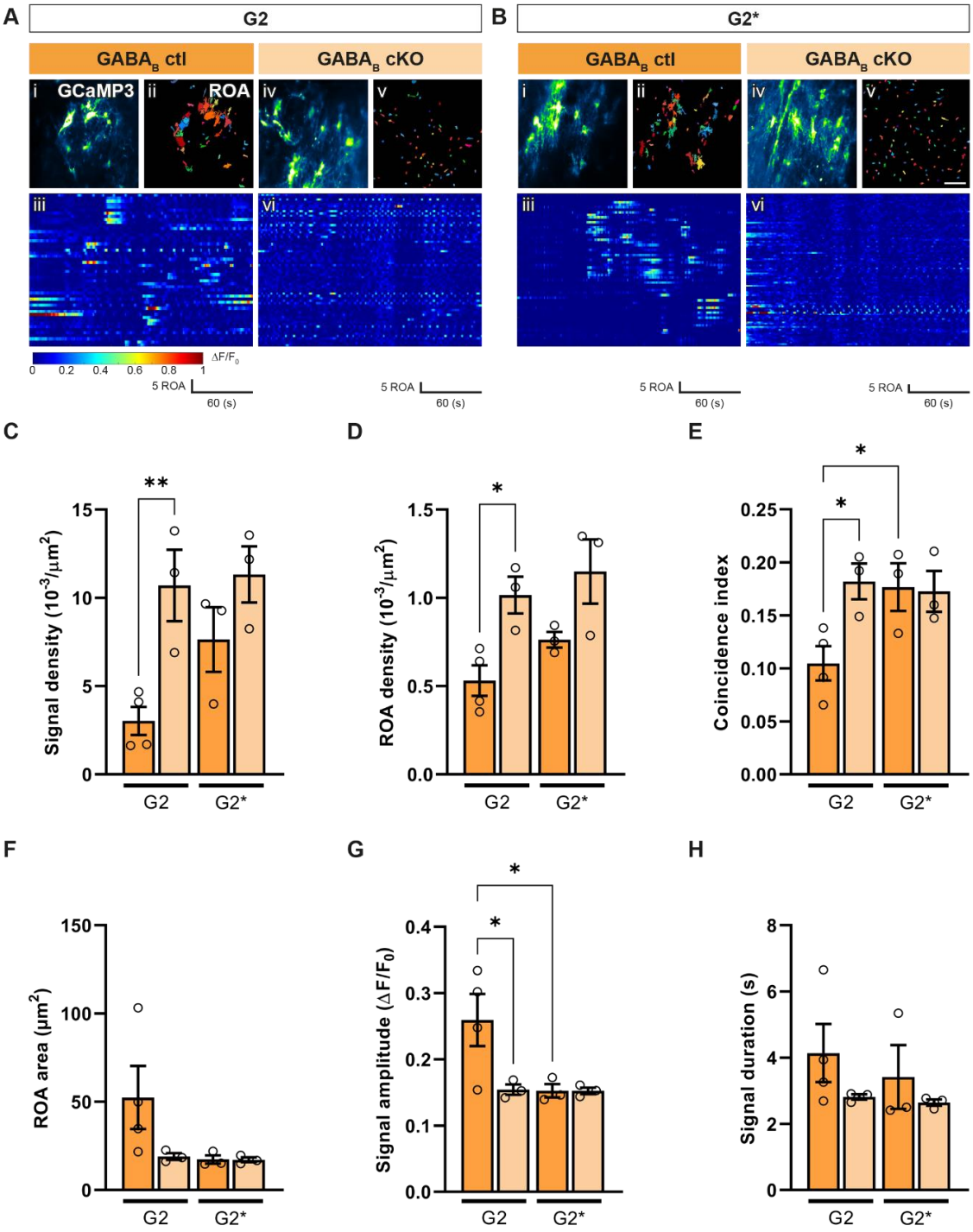

Figure 23: *In vivo* Ca^{2+} signaling of $GABA_B$ ctl and cKO OPCs after demyelination.

Fluorescence changes of the Ca^{2+} indicator GCaMP3 in $NG2^{GCaMP3+}$ (ctl) and $NG2^{GCaMP3}$ x $GABA_B^{fl/fl}$ (cKO) cells automatically detected by MSparkles at G2 (A; ctl: i-iii; cKO: iv-vi) and G2* (B; ctl: i-iii; cKO: iv-vi) one week after CPZ treatment and six weeks after tamoxifen administration. Maximum intensity projection of the image (i/iv), automatically detected ROAs as a color-coded map (ii/v) and the fluorescence change over time of all ROAs as a heatmap (iii/vi). The key parameters signal density (C), ROA density (D), coincidence index (E), ROA area (F), signal amplitude (G) and signal duration (H) show six parameters of the software to separate Ca^{2+} activity between conditions. Scale bar = 50 µm. N = 3-4, the mean values ± SEM from several FOVs (n = 12-16) are shown and compared using ordinary one-way ANOVA. *p <0.05, **p <0.01.

The Ca^{2+} activity examined in the last part showed predominantly differences between ctl and cKO in the CPZ untreated group G2, which was inversed to the results shown previously (Figure 17) but recorded at a three-week later time point. Signal and ROA density and coincidence index were increased in cKO and signal amplitude was decreased. For the CPZ-treated group, the only differences in ctl compared to the untreated group were shown for the coincidence and amplitude of the signals, which comparatively changed in the opposite direction. There were no differences for cKO between untreated and treated group, Ca^{2+} activity and active regions was similar.

7 DISCUSSION

Glial cells do not use electrical excitability as their main communication pathway like neurons, but predominantly Ca^{2+} as a second messenger to process intra- and extracellular information. This signaling pathway of communication within glial cells is cell type specific and can be influenced by GABAergic stimulation of the metabotropic $GABA_B$ receptor and has already been shown for astrocytes and is also suspected for oligodendrocyte precursor cells. The investigation of glial Ca^{2+} activity under physiological conditions in the spinal cord, as well as the influence of $GABA_B$ receptor loss in oligodendrocyte precursor cells and associated effects on toxic demyelination by cuprizone was performed by *in vivo* two-photon Ca^{2+} imaging and immunohistochemical analysis in the spinal cord using transgenic mice and resulted in the following key findings of this thesis:

- Glial Ca^{2+} activity is cell type specific in the spinal cord for oligodendrocyte precursor cells (OPCs), astro- and microglia while region dependent for OPCs and astroglia but not microglia.

- Deletion of the metabotropic $GABA_B$ receptor in oligodendrocyte precursor cells reduces their Ca^{2+} activity and alters myelin formation.

- Cell-type specific $GABA_B$ receptor loss in oligodendrocyte precursor cells results in a myelin-protective effect during toxic demyelination with less altered Ca^{2+} activity.

The spinal cord (medulla spinalis) is a major part of the central nervous system and at the same time the link between the body and the brain. This is because afferents with sensory information of the skin, skeletal muscles, joints as well as the viscera enter via the posterior roots of the spinal nerves, while spinal nerve roots exit at its front and conduct information to the periphery as efferents - to the skeletal muscles, the viscera, for instance. For this purpose, spinal cord circuits between and within neurons and glia are indispensable for sensory information processing and controlling reflexes and adaptive behaviors in physiology as well as pathophysiology; an intermezzo that can effect cellular and regional differences between spinal segments or gray and white matter (Shekhtmeyster et al., 2023).

7.1 GLIAL Ca^{2+} ACTIVITY IS CELL TYPE SPECIFIC IN THE SPINAL CORD FOR OPCS, ASTRO- AND MICROGLIA WHILE REGION DEPENDENT FOR OPCS AND ASTROGLIA BUT NOT MICROGLIA

To analyze in detail Ca^{2+} activity in different glial cell types in the spinal cord under physiological conditions, two-photon Ca^{2+} imaging was performed in transgenic mice expressing the Ca^{2+} indicator GCaMP3 in astroglia, microglia, or NG glia (oligodendrocyte precursor cells (OPCs; **Figure 8**)), and the images were analyzed using MSparkles, a fully automated Ca^{2+} analysis software (Stopper et al., 2022).

This fully automated software was developed to obtain unbiased detection as well as analysis of fluorescence change with background subtraction. Furthermore, this application allows a method detached from the morphology of the otherwise mostly manually selected regions of interest and reflects regions of activity (ROAs) as automatically recognized areas for Ca^{2+} activity. The applied software enables, by feeding with the recordings generated by means of 2P-LSM, besides the ROA detection also an overview of the signal traces, additionally a visual illustration of the activity as heatmap and a synchronicity trace of the Ca^{2+} activity (**Figure 9**). In addition to spontaneous Ca^{2+} activities in astroglia, chemical and electrical stimulation can also be performed, allowing intracellular Ca^{2+} changes to be observed. The results show different synchronicity or reinforced coincidence considering that these signals, especially when spontaneously recorded, are more coincidental than synchronously caused by a trigger. Synchronicity in this case would mean a concrete coordination of the signals, whereas coincidence would indicate a random temporal relationship of the signals. The duration and amplitude magnitude, as well as the number of the signal and distribution gives information about the relative activity of the cells. Ca^{2+} is the main and critical signaling pathway of non-electrically excitable glial cells for intra-/extracellular communication (Clapham, 2007). Nevertheless, it is hardly described in the

literature that astroglia in an electrically excited environment can positively influence critical neurological and psychiatric diseases, especially of the brain. Astroglia, like neurons, are also electrically excitable and, unlike neurons, do not show a sustained constant excitability in their Ca^{2+} response, which is consistent with the results previously shown here by stimulations and should be considered when using complex electrical neuromodulation (Cirillo et al., 2012; Ma et al., 2021). Similarly, via adrenergic α1 and β1 receptors, distinct Ca^{2+} responses to noradrenergic stimulations were also shown here for astrocytes (Delumeau et al., 1991; Horvat et al., 2016; Nuriya et al., 2017).

Regarding the structural properties of the individual Ca^{2+} signals, no differences between astroglia and microglia could be identified *in vivo* nor *ex vivo* and differences were only found for the signal amplitude and signal duration of the OPCs, which were predominantly manifested in a time shortening *in vivo* (**Supplementary Figure 1**). This suggests common mechanisms underlying Ca^{2+} homeostasis and may be exclusively faster in time for the OPCs, indicating that faster signal paths are required here. Exclusively key parameters identified in this work, such as ROA density, ROA area, signal density, signal frequency, and coincidence, provide the ability to distinguish glial Ca^{2+} signals spatial and temporally and thus these cell types from each other and occur differently *ex vivo* in slices than *in vivo* in sleeping mice (Rieder et al., 2022). A detailed comparison between astroglia and microglia has already been published and is attached as an appendix. This work is extended here to include OPCs which Ca^{2+} signals can be evoked by axons and astrocytes releasing ATP and glutamate (Hamilton et al., 2010). Looking more closely at spontaneous recordings of Ca^{2+} activity and comparing astroglia and microglia, with OPCs by six key parameters (signal and ROA density, coincidence index, ROA area, signal amplitude and duration; **Figure 10**), *in vivo* reveals high signal density and frequency of signals in a few, small ROAs for OPCs, which appear highly coincident with short duration. For the developing OPCs, Ca^{2+} and its controlled intracellular oscillation is important for proliferation. This can be disturbed in case of continuously high Ca^{2+} concentration and integrate synaptic inputs with Ca^{2+} changes globally and in their fine dendrites (Sun et al., 2016; Seidman et al., 2022). A similar high signal density is shown for microglia Ca^{2+} activity distributed over a high number of ROAs with moderate coincidence, area and signal duration. Contrary to literature, where microglia show increased Ca^{2+} signaling only in response to inflammation and injury and otherwise lag behind astroglia in Ca^{2+} activity *in vivo*, the results in this work show relatively high spontaneous Ca^{2+} activity in microglia compared to other glial cells (Eichhoff et al., 2011; Pozner et al., 2015). In addition, it is known that high Ca^{2+} activities are required for the surveillance function of the microglial projections that constantly scan the environment (Umpierre et al., 2020); inflammatory reaction is excluded here (Rieder et al., 2022). Comparatively few signals are detectable in

astroglia, which are low coincidentally active in a few ROAs of intermediate extent and signal duration. This is consistent with the fact that astroglial Ca^{2+} signals, which can otherwise be diverse and extend across multiple astroglia, are attenuated under anesthesia (Thrane et al., 2012; Fujii et al., 2017; Taheri et al., 2017). Only in the signal amplitude all three cell types are indistinguishable. In every other measured parameter, the three different cell types always show pairwise similarities in parameters to different pairs. Thus, OPCs and microglia are similar in signal density, and OPCs and astroglia are similar in ROA density. Only in two parameters, ROA area and signal density, astroglia and microglia resemble each other in their Ca^{2+} activity. It is worth mentioning that chronically studied over a week, Ca^{2+} activity hardly changes between days. This is not true for OPCs, whose signal incidence and frequency are highest on day seven compared to the other days before (**Supplementary Figure 1**). Looking at the differences between the white and gray matter *ex vivo* (**Figure 11** & **Figure 12**), already known morphological differences for astroglia can be seen, which can also be reflected in the Ca^{2+} activity by a different ROA area, which is more extensive in the gray matter. Microglia show no regional difference in any of the parameters. For OPCs, on the other hand, the coincidence of the signals shows a strong increase in the white matter. Both results can be explained by the different features of the cell types. For astrocytes by their enormous heterogeneity and for OPCs by their special task in the myelinated white matter as monitor and maintainer of the function of fast axonal excitation propagation (Bayraktar et al., 2014; Dimou and Gallo, 2015; Parolisi and Boda, 2018). Finally, the differences between in vivo and ex vivo should not be ignored. These were particularly evident for microglia compared to the other glial cells, but also point in particular to regional specifications for astroglia and OPCs when looking at the signal area and its coincidence. This complicates future interpretations of responses to chemical stimuli, which can only be studied ex vivo in fresh slices.

In summary, differently stimulated Ca^{2+} signals in astrocytes could be compared for their properties and physiological differences between astroglia, microglia and OPCs could be identified, which are intrinsic to the different tasks and natures of the cell types. OPCs showed a signal density similar to microglia and a density of active regions comparable to astroglia. These results were consistent when examined chronically over one week.

7.2 DELETION OF THE METABOTROPIC $GABA_B$ RECEPTOR IN OLIGODENDROCYTE PRECURSOR CELLS REDUCES THEIR CA^{2+} ACTIVITY AND ALTERS MYELIN STRUCTURE

Cell type-specific reduction of the metabotropic $GABA_B$ receptor in OPCs (NG2 glia) was detected by quantitative RT-PCR in the $NG2^{GCAMP3}$ x $GABA_B^{fl/fl}$ mouse line, an already established method (Fang et al., 2022b). Here, already two weeks after tamoxifen administration, a reduction was clear after checking the purity of the sorted cells (**Figure 13**). With the confirmation of the $GABA_B$ receptor loss, further analysis revealed no changes in recombination or cell numbers in the populations of OPCs or mature oligodendrocytes between ctl and cKO mice (**Figure 14**). Thus, the deletion of the $GABA_B$ receptor does not lead to a change of differentiation in the adult oligodendrocyte lineage, whereas in the developing CNS, functional expression of the receptor stimulates proliferation and migration of precursor cells in in rat primary cerebral culture (Luyt et al., 2007). But it is the control of myelination by OPCs and their GABAergic control shown for cerebral interneurons that makes them key players in functional brain function, myelination right up to the adjustment of cognitive abilities (Fang et al., 2022b). Furthermore, a high heterogeneity was shown for OPCs varying in age, myelination capacity and location (Dimou and Simons, 2017; Foerster et al., 2019; Boshans et al., 2020; Sherafat et al., 2021). And for example important for a subgroup of OPCs, belonging to the OL (2-26 %), which remain in a precursor stage as soon as a disturbance of brain physiology occurs (Fang et al., 2022a). Myelin analysis after induction of $GABA_B$ receptor loss showed MBP reduction, whereas myelin thickness, degenerated MBP, and neurofilament (in white and grey matter) did not change (**Figure 15**). This revealed a quantitative change in myelin with one of its major components MBP, analyzed by fluorescence intensity measurement before a morphological change in myelin structure is apparent upon ring formation. This result confirms the potential contribution of the $GABA_B$ receptor to myelination, through loss there is a reverse effect of myelination potency due to receptor activity (Serrano-Regal et al., 2019). The change shown here is probably not due to the change in differentiation, since only about 2 % recombined mature oligodendrocytes were counted. Much more, a mechanism via the neurons with which OPCs form synapses seems possible. It is the interplay between neurons and oligodendrocytes that is important for myelination capacity, as discussed at the beginning. Thus, impaired and reduced Ca^{2+} activity in OPCs could passively affect myelination. Interestingly, and underscoring this, not only is the metabotropic $GABA_B$ receptor responsible for intact myelination, impaired remyelination was also shown by the loss of voltage-dependent $Ca_v1.2$ channel (Santiago González et al., 2017). Whether this myelin change is accompanied by a proliferation change of the recombined OPCs and whether

there is an activation of microglia and astroglia could not be confirmed. Consequently, the measured MBP loss and thus myelin change was not related to a change in the cell cycle of recombined OPCs and were not accompanied by microgliosis or astrogliosis (**Figure 16**). MBP levels reduced by manipulation and loss of the $GABA_B$ receptor could be supplemented by live Ca^{2+} analysis. This showed decreased activity in signal density, number of active regions, and coincidence of signals compared with ctl mice *in vivo* (**Figure 17**). Thus, loss of the $GABA_B$ receptor also showed a change with reduced Ca^{2+} activity in OPCs due to decreased reactivation of intracellular Ca^{2+}. This proves that reduction of $GABA_B$ receptor mRNA leads to a functional change affecting cell physiology. Despite fewer signals that appeared less synchronous and occurred in less active regions, the areas and signal parameters of amplitude and length remained unchanged. In general, this can be interpreted as reduced cell activity that triggers less myelination by the surrounding oligodendrocytes. And it is known that myelin is different between the brain and the spinal cord. For example, the myelin sheaths produced by oligodendrocytes in the brain are shorter than those produced by oligodendrocytes in the spinal cord and thus presumably have different resilience (Bechler et al., 2015).

Losing the $GABA_B$ receptor in OPCs thus resulted in a change in spinal myelin structure but no shift in OL composition or gliosis. Ca^{2+} activity was attenuated, raising the question of how this would be the case with active manipulation of myelination and is answered in the next part of this work.

7.3 Cell-type specific $GABA_B$ receptor loss in oligodendrocyte precursor cells results in a myelin-protective effect during toxic demyelination with less altered Ca^{2+} activity

Multiple sclerosis is known to cause damage to myelin, which can only be repaired to a limited extent by remyelination by oligodendrocytes if chronic, or can be worsened by defective OPCs (Jäkel et al., 2019; Lassmann, 2019; Yeung et al., 2019). The model used here to induce myelin loss is a toxic, systemic demyelinating one. It was chosen to study the effect of myelin alteration and Ca^{2+} activity reduction due to $GABA_B$ receptor loss in OPCs. The diet with Cuprizone (CPZ) leads to a weight loss that has been described before and is commonly known (Steelman et al., 2012; Toomey et al., 2021). This weight loss is clinically the only external effect observed during the course of the experiment and is a sure sign that demyelination is progressing; far less aggressively than in an inflammatory demyelination model. The CPZ diet resulted in the expected weight loss with first a steep

and then a stable progression, which in combination with the $GABA_B$ receptor loss was distinctly stronger than without (**Figure 18**). No gender-specific differences were observed in the response to the diet, which makes an analysis purely concerning the $GABA_B$ receptor possible.

As before, the proportion of OPCs and mature oligodendrocytes was determined here with a longer interval to induction of cKO and in combination with demyelination. Again, there was no change due to receptor loss in OL composition and this was also true at the time point after demyelination (**Figure 19**). Over time, the number of mature oligodendrocytes changed and was greater in the cKO group while it was increased by CPZ treatment in the ctl group, but this was not evident in the mice with $GABA_B$ receptor deficit (**Supplementary Figure 6**). This is contrary to the hypothesis that stimulation of the $GABA_B$ receptor can lead to potentiation of OPC differentiation and might be region-specific.

For the expression of MBP, there was no difference at the later time point due to the extent of the diet, but there was a clear demyelination-related loss in the group with functional $GABA_B$ receptor. MBP was not affected by loss of the $GABA_B$ receptor here. Demyelination could also be confirmed by measuring the ring thickness of myelin and was clearly evident for the ctl group but had no effect on the receptor-deficient mice. Despite myelin ring thickness impairment, axons in gray and white matter remained unchanged (NF) and the level of degraded MBP did not change but was quite high over all (**Figure 20** & **Supplementary Figure 7**). The protective effect of $GABA_B$ receptor loss in the CPZ model reflects its crucial role in myelination. Conversely, targeted stimulation of this receptor by its agonist baclofen promoted myelination (Serrano-Regal et al., 2022).

Demyelination showed no change in the proliferation rate of the recombined OPCs, but the data sets were scattered probably because of the limited field of observation in the spinal cord. Also, no gliosis could be detected by Iba1 or GFAP activation, suggesting only a mild demyelination model in the spinal cord by cuprizone (**Figure 21** & **Figure 22**) compared to forebrain data from literature (Zirngibl et al., 2022). This is accompanied by the undetected change of the degenerated MBP and suggests an onset of demyelination at the observed time point, in which there are already qualitative impairments that can be protected by a $GABA_B$ receptor deficit and appear without showing structural effects.

Looking at the Ca^{2+} signals of the OPCs at the later time point with 15 weeks, they were inverted compared to the data at 12 weeks (chapter 7.2). Due to the $GABA_B$ receptor loss, an increased Ca^{2+} activity was shown by increased signal density, ROA density and coincidence of the signals with reduced amplitude excursion. For the demyelination group, the $GABA_B$ receptor loss was without changes and only the control group showed increased

coincidence with decreased amplitude compared to the untreated group. Thus, it can be said that at this time point, Ca^{2+} activity was increased by receptor loss and is not altered in intensity by demyelination (**Figure 23**). As increased Ca^{2+} activity coincides with increased cell stress (Ermak and Davies, 2002; Cerella et al., 2010), this indicates that the receptor-deficient OPCs already exert increased activity of their cellular functions and this decelerates the demyelination process and has protective effects.

Here, the complexity of OPCs and oligodendrocytes becomes apparent. If at an earlier time point Ca^{2+} activity is decreased by $GABA_B$ receptor loss and loss of MBP has been shown, at a later time point and by the toxic demyelination model a protective effect is evident (5 weeks later), but Ca^{2+} activity is increased by receptor loss. Presumably, at the later time point, the new mature oligodendrocytes are able to form better myelin, which brings a protective effect. Thus, the loss of the receptor may have a negative effect at the early time point and a positive effect later on. Already in zebrafish it was shown that low Ca^{2+} amplitudes are beneficial for myelin sheath formation, whereas short and high frequency amplitudes can be detrimental (Baraban et al., 2018; Paez and Lyons, 2020). This is due to the fact that Ca excess per se can be cytotoxic and due to a rapid increase and high cytoplasmic concentration changes the cells cannot react fast enough to mitigate it. Especially a constant amplitude ratio over all groups after CPZ showed this and could argue for a better myelin quality after the diet (**Figure 23G**). Electron-microscopic images should be used for a more precise quantification. Several publications showed that the myelination capacity of oligodendrocytes depends not only on their own Ca^{2+} homeostasis but also on the Ca^{2+} signals released from the axons to be myelinated (Krasnow et al., 2018; Miller, 2018). Furthermore, the ability of MBP as one of the main components of myelin to establish its membrane integrity is influenced by protein zero (P0) and the given cellular Ca^{2+} concentration (Raasakka et al., 2019), in this case shown for peripheral nerves. Moreover, there are differences between rodent and human OL responses to demyelination and from which cells or concomitant circumstances demyelination originates (Jäkel et al., 2019). The increasing importance of investigating transcriptional influences in the course of a degenerative disease also shows how complex it is when multiple pathways have to be illuminated and how for example in this work a manipulation of the GABAergic $GABA_B$ receptor has an effect on myelinating OL cells not directly affected but probably via an OPC, neuron, oligodendrocyte interaction.

If we now combine the effect of the receptor loss and its impact on reduced Ca^{2+} activity and myelination and a myelin protection in case of demyelination (chapters 7.2 and 7.3), considering that $GABA_B$ receptor activation in OPCs leads to intracellular Ca^{2+} increase released from the ER, there is an active network effect within the glial syncytium probably

involving neurons. Hence, the initially reduced Ca^{2+} activity due to loss of the receptor may be compensated in the later course and an increased Ca^{2+}/cell activity may result in a protective effect against demyelination. Further myelin proteins such as MAG and MOG or PLP would need to be investigated for precise clarification, as well as targeted chemical $GABA_A$ and $GABA_B$ receptor stimulation during the course of demyelination.

8 CONCLUSION AND OUTLOOK

In the first part of the present study, cell type-specific Ca^{2+} activities were revealed using a genetically encoded Ca^{2+} sensor in glial cells of the spinal cord *in vivo* and *ex vivo*, which are characteristic depending on cell function and, in the case of astroglia, can be stimulated in different ways. In some cases, differences in methodology were identified that led to possible artifacts or changes in signal parameters *ex vivo* and were represented in the publication attached to this work. In the second part, the conditional knockout of the metabotropic $GABA_B$ receptor in oligodendrocyte precursor cells was demonstrated and its reducing effect on myelin and Ca^{2+} activity was shown. In the subsequent and final part, the myelin-protective effect caused by $GABA_B$ receptor loss was demonstrated in a toxic demyelination model.

The protective effect demonstrated is promising, especially because the understanding and treatment of demyelinating diseases such as multiple sclerosis requires urgent research and action. Especially for the second messenger Ca^{2+}, which is used as main communication in glial cells, the underlying mechanisms reveal a complexity, which becomes even more extensive by the manifold modifiable differentiation of the oligodendroglial lineage. Nevertheless, Ca^{2+} activity could be a key factor for therapy, because agonists acting via GABA signaling pathways are already therapeutic options for spasticity. But the regional heterogeneity of the nervous system and different cell response could become a difficulty here.

Future research goals may include ultra-high-resolution microscopy of myelin structures and their individual components up to molecules, as well as the interplay of different signaling pathways and their changes over time in a demyelinating disease. Thus, inflammatory cascades are just as interesting as acute cellular stress responses, which can change as shown here, and which can be of particular interest in the relapsing course of multiple sclerosis.

9 APPENDIX

9.1 SUPPLEMENTARY FIGURES

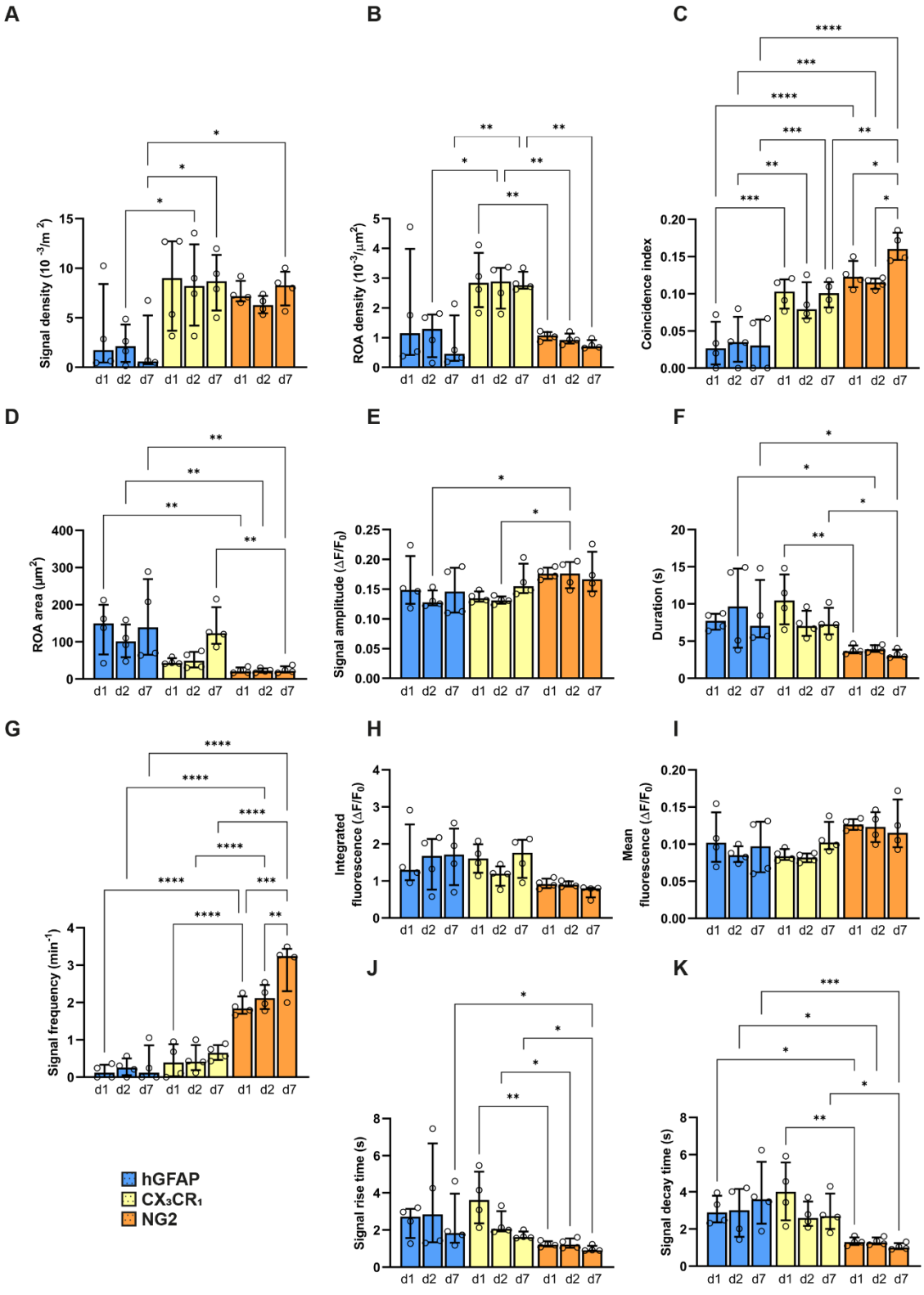

Supplementary Figure 1. *In vivo* Ca^{2+} signaling in astro-, microglia and OPCs is cell-specific and mostly time-independent as well as surgery independent.

MSparkles analysis depicts signal density (**A**), ROA density (**B**), coincidence index (**C**), ROA area (**D**), signal amplitude (**E**) and signal duration (**F**) as six key parameters of the software to separate Ca^{2+} activity one, two and seven days after laminectomy. Signal frequency (**G**), Integrated fluorescence (**H**), mean fluorescence (**I**), Signal rise (**J**) and decay time (**K**). N = 4, the mean or median values ± SEM/IQR from several FOVs (n = 16) are shown and compared using ordinary one-way ANOVA or Kruskal-Wallis test. *p <0.05, **p <0.01, ***p <0.001, ****p <0.0001.

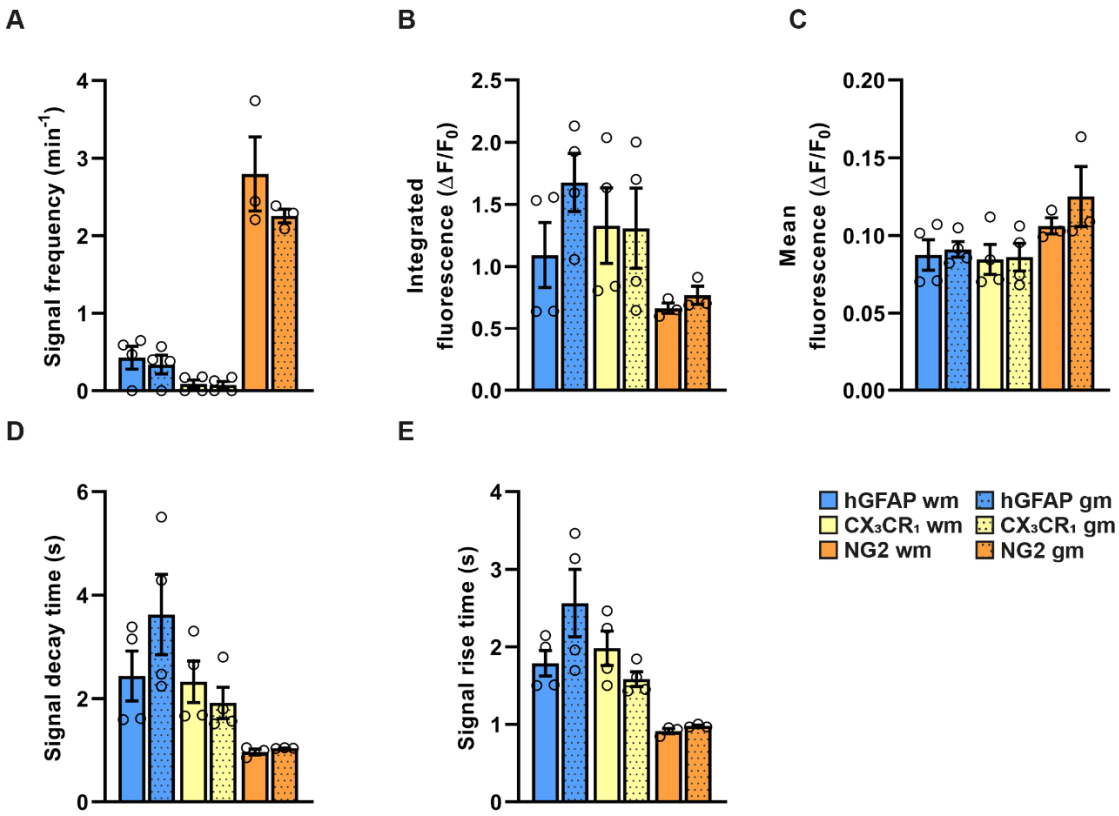

Supplementary Figure 2: Ca^{2+} activity in acutely isolated spinal cord slices.

Automated activity analysis using MSparkles for additional parameters signal frequency (**A**), integrated fluorescence (**B**), mean fluorescence (**C**), signal decay (**D**), and rise time (**E**) to analyze 2P-LSM recordings from white and grey matter. N = 3-4, the mean or median values ± SEM/IQR from several FOVs (n = 12-16) are shown and the two matters per cell type were compared using unpaired t- or Mann-Whitney test.

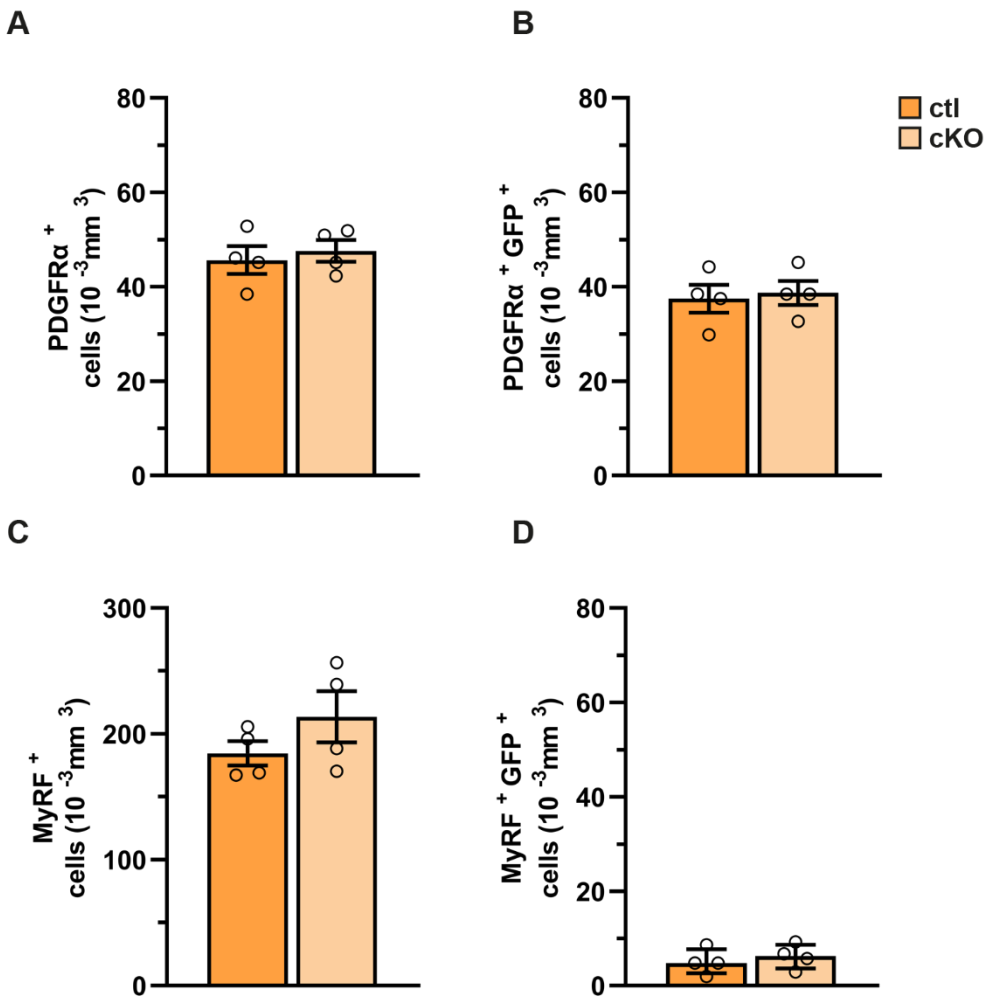

Supplementary Figure 3: Cell numbers of OL remains unchanged by $GABA_B$ receptor loss in white matter OPCs.

Three weeks after tamoxifen-induced recombination, cell type-specific staining by immunohistochemistry shows equal cell numbers for PDGFRα⁺ OPCs (A), recombined PDGFRα⁺ and GFP⁺ OPCs (**B**), MyRF⁺ oligodendrocytes (**C**) and MyRF⁺ and GFP⁺ oligodendrocytes (**D**) in ctl and cKO mice. N = 4, n = 32 ROIs from 16 slices showing mean ± SEM.

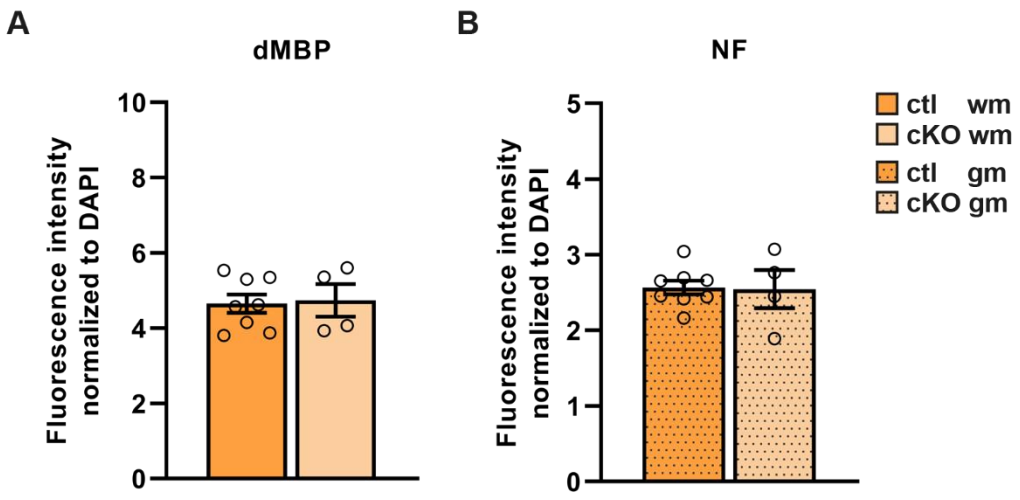

Supplementary Figure 4: No change of dMBP and NF after $GABA_B$ receptor depletion in OPCs.

Fluorescence intensity analysis normalized to DAPI shows no difference between ctl and cKO for dMBP (**A**) in the white matter and no difference in gray matter NF (**B**). N = 4-8, n = 96 ROIs from 48 slices in case for fluorescence intensity, the shown mean ± SEM were compared using unpaired t-test.

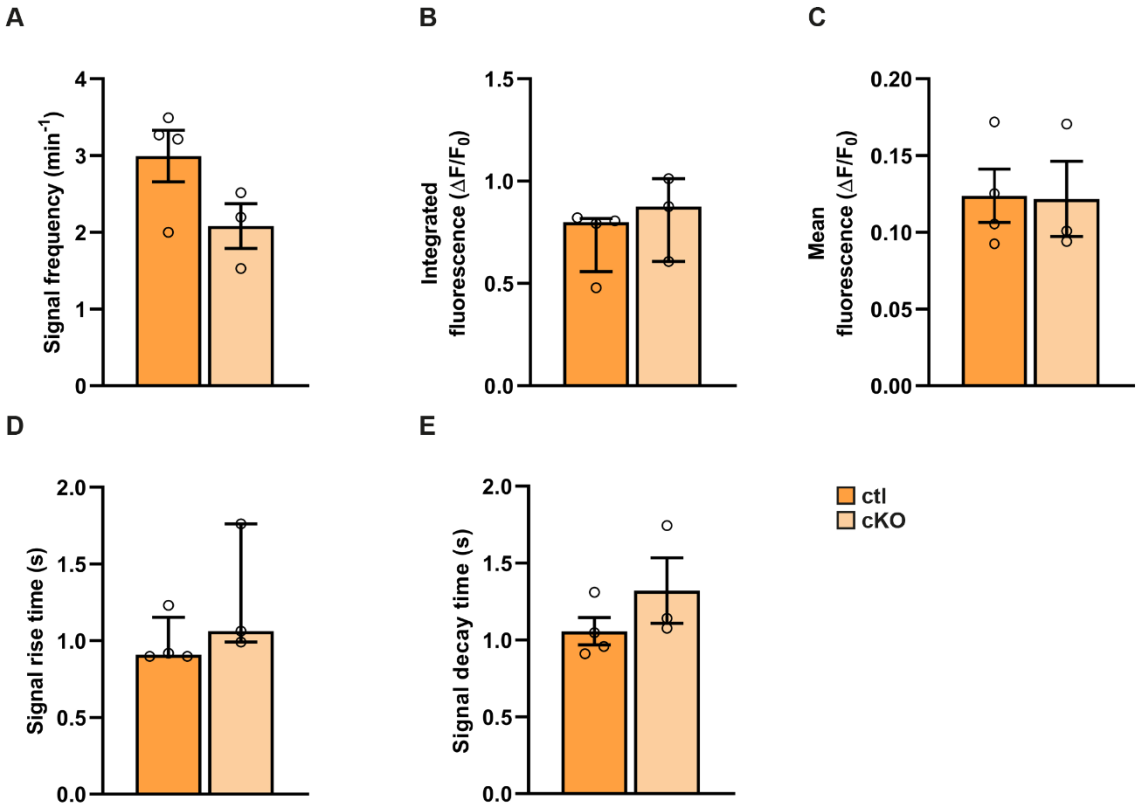

Supplementary Figure 5: *In vivo* Ca^{2+} signaling of OPCs in the $GABA_B$ cKO.

Recordings of the Ca^{2+} indicator GCaMP3 in $NG2^{GCaMP3+}$ (ctl) and $NG2^{GCaMP3}$ x $GABA_B^{fl/fl}$ (cKO) automatically detected by MSparkles two weeks after five times tamoxifen administration (G1) does not show differences in the parameters signal frequency (**A**), integrated fluorescence (**B**), mean fluorescence (**C**), signal rise (**D**) and decay time (**E**) between ctl and cKO. N = 3-4, the mean or median values ± SEM/IQR from several FOVs (n = 12-16) are shown and compared using unpaired t- or Mann-Whitney test.

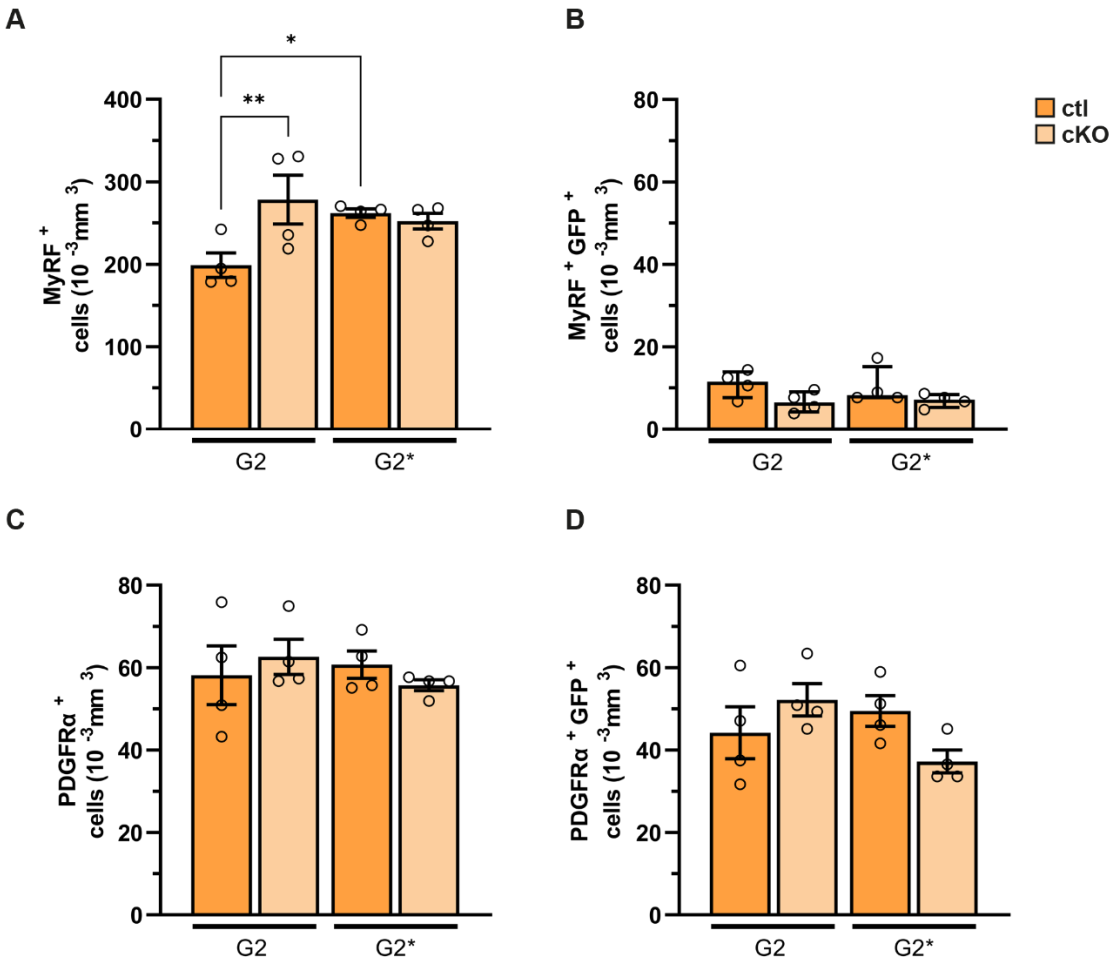

Supplementary Figure 6: More OL in demyelination and in mice with $GABA_B$ receptor loss.

Six weeks after tamoxifen-induced recombination, changes in cell numbers for MyRF⁺ oligodendrocytes (**A**) but not for MyRF⁺ and GFP⁺ oligodendrocytes (**B**), PDGFRα⁺ OPCs (**C**) and PDGFRα⁺ and GFP⁺ OPCs (**D**) were found. N = 4, n = 32 ROIs from 16 slices showing mean or median ± SEM/IQR.

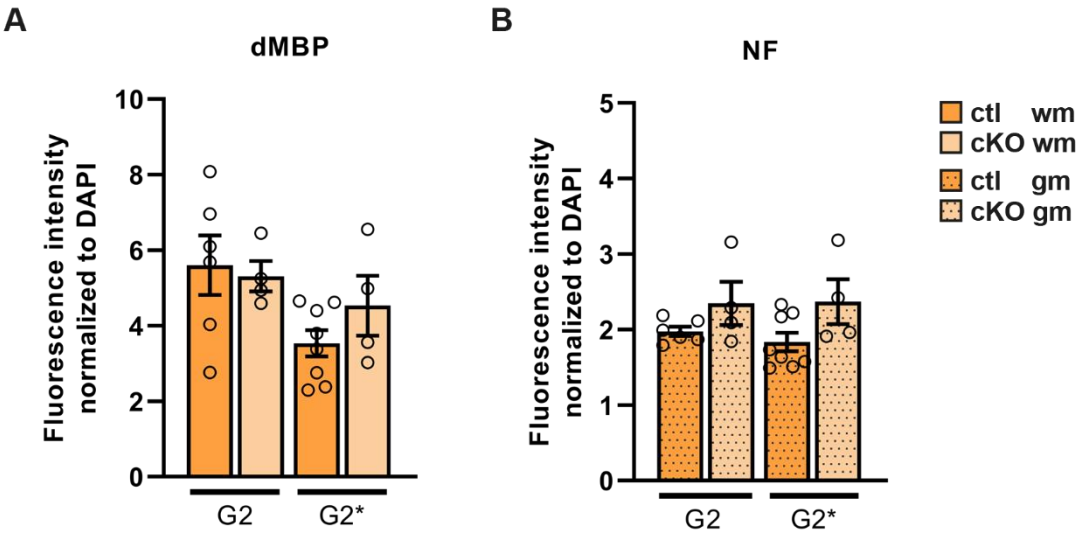

Supplementary Figure 7: No changes in dMBP in white and NF in grey matter by $GABA_B$ cKO or ctl in demyelination.

Fluorescence intensity analysis normalized to DAPI shows no difference between ctl and cKO or between CPZ untreated (G2) and treated group (G2*) for dMBP (**A**) in white and NF (**B**) in gray matter of the spinal cord N = 4-8, n = 96 ROIs from 48 slices showing the mean ± SEM and compared using one-way ANOVA.

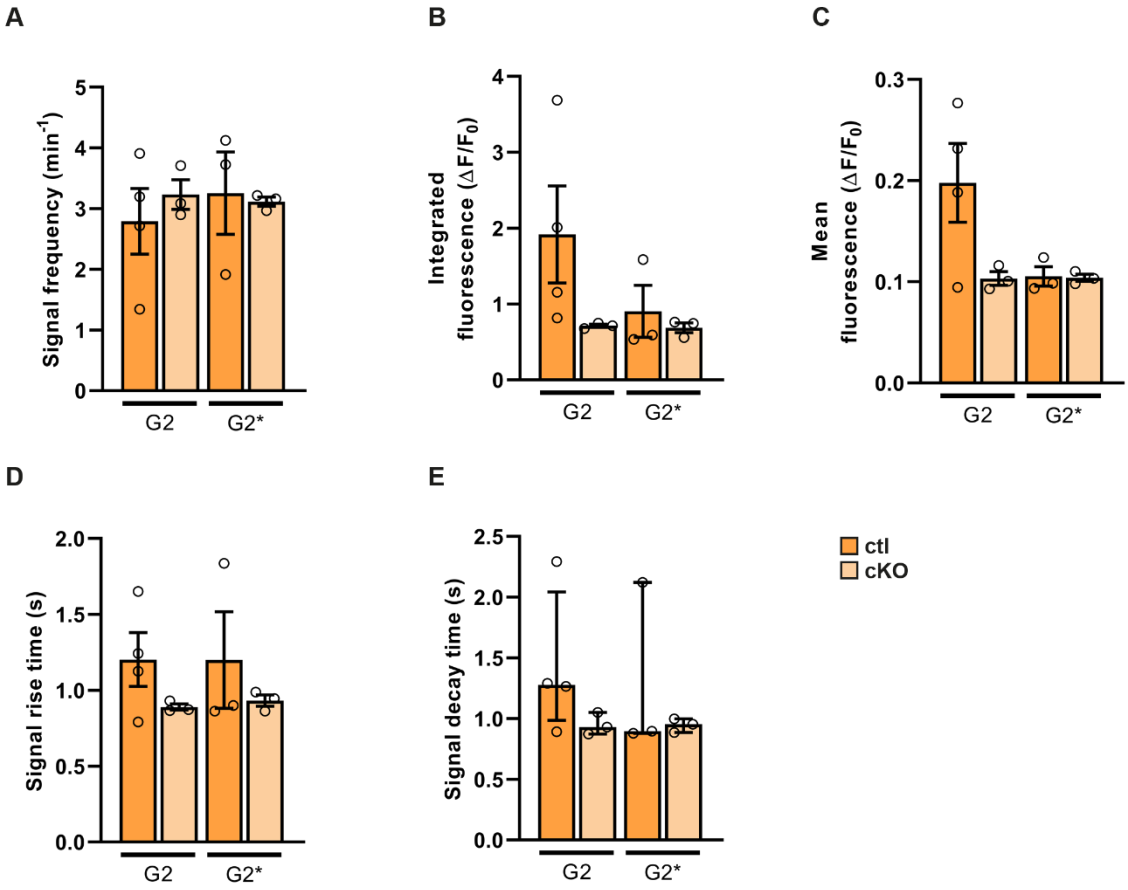

Supplementary Figure 8: *In vivo* Ca^{2+} signaling of $GABA_B$ ctl and cKO OPCs in demyelination.

Fluorescence changes of the Ca^{2+} indicator GCaMP3 in $NG2^{GCaMP3+}$ (ctl) and $NG2^{GCaMP3}$ x $GABA_B^{fl/fl}$ (cKO) cells automatically detected by MSparkles at G2 and G2* one week after CPZ treatment and six weeks after tamoxifen administration. Signal frequency (**A**), integrated fluorescence (**B**), mean fluorescence (**C**), signal rise (**D**) and decay time (**E**) to separate Ca^{2+} activity between conditions. N = 3-4, the mean or median values ± SEM/IQR from several FOVs (n = 12-16) are shown and compared using ordinary one-way ANOVA or Kruskal-Wallis test.

9.2 SUPPLEMENTARY TABLES

Supplementary Table 1: MSparkles analysis parameters for automated Ca^{2+} analysis.

Pre-processing	
PURE-LET denoise	
Temporal median filter	Kernel half-size: 2
Stack registration	Reference frame: 1
F_0 computation	
Smoothing	Kernel half-size: 5; Sigma 2
Outlier removal (mean + SD)	Order: 3; Sigma factor: 2.00
Guidance signal	Order: 6; Optimizer: min. error
F_0 fit	Order: 5
ROA detection & analysis	
Detrending	$(F-F_0)/F_0$
Segmentation method: correlation	Threshold: 0.5
Range image smoothing	Sigma: 3; Medial filter size: 7
ROA detection threshold	Guided threshold; Detector sensitivity: 90 %
Minimum ROA area	50 pixels
Sanity bounds	Min: -1; Max: 20
Signal filtering	Order: 3; Size: 7
Signal duration height preference	50 % full width at half maximum
Minimum peak prominence	0.1
Maximum signal duration	50 s
Classification thresholds	0.1; 0.25; 0.5; 1; 1.5
Synchronicity duration reference	50 %
Synchronicity threshold	0.5

9.3 SUPPLEMENTARY PUBLICATION

frontiers in Molecular Neuroscience

ORIGINAL RESEARCH
published: 30 March 2022
doi: 10.3389/fnmol.2022.840948

OPEN ACCESS

Edited by:
Stella Elkabes,
Rutgers Biomedical and Health Sciences, United States

Reviewed by:
Eric Newman,
University of Minnesota Twin Cities, United States
Alexey Semyanov,
Institute of Bioorganic Chemistry (RAS), Russia
Joshua R. Berlin,
Rutgers Biomedical and Health Sciences, United States

***Correspondence:**
Anja Scheller
anja.scheller@uks.eu

†ORCID:
Phillip Rieder
orcid.org/0000-0002-0786-574X
Davide Gobbo
orcid.org/0000-0002-4076-2697
Gebhard Stopper
orcid.org/0000-0003-2496-4755
Anna Welle
orcid.org/0000-0001-9915-2845
Elisa Damo
orcid.org/0000-0002-1205-1097
Frank Kirchhoff
orcid.org/0000-0002-2324-2761
Anja Scheller
orcid.org/0000-0001-8955-2634

‡These authors have contributed equally to this work

Specialty section:
This article was submitted to Brain Disease Mechanisms, a section of the journal Frontiers in Molecular Neuroscience

Received: 21 December 2021
Accepted: 22 February 2022
Published: 30 March 2022

Citation:
Rieder P, Gobbo D, Stopper G, Welle A, Damo E, Kirchhoff F and Scheller A (2022) Astrocytes and Microglia Exhibit Cell-Specific Ca^{2+} Signaling Dynamics in the Murine Spinal Cord. Front. Mol. Neurosci. 15:840948. doi: 10.3389/fnmol.2022.840948

Astrocytes and Microglia Exhibit Cell-Specific Ca^{2+} Signaling Dynamics in the Murine Spinal Cord

Phillip Rieder[1†‡], Davide Gobbo[1†‡], Gebhard Stopper[1†], Anna Welle[2†], Elisa Damo[1,3†], Frank Kirchhoff[1†] and Anja Scheller[1†]*

[1] Department of Molecular Physiology, Center for Integrative Physiology and Molecular Medicine (CIPMM), University of Saarland, Homburg, Germany, [2] Department of Genetics and Epigenetics, University of Saarland, Saarbrücken, Germany, [3] Institute of Pharmacology, Medical Faculty Heidelberg, Heidelberg University, Heidelberg, Germany

The spinal cord is the main pathway connecting brain and peripheral nervous system. Its functionality relies on the orchestrated activity of both neurons and glial cells. To date, most advancement in understanding the spinal cord inner mechanisms has been made either by *in vivo* exposure of its dorsal surface through laminectomy or by acute *ex vivo* slice preparation, likely affecting spinal cord physiology in virtue of the necessary extensive manipulation of the spinal cord tissue. This is especially true of cells immediately responding to alterations of the surrounding environment, such as microglia and astrocytes, reacting within seconds or minutes and for up to several days after the original insult. Ca^{2+} signaling is considered one of the most immediate, versatile, and yet elusive cellular responses of glia. Here, we induced the cell-specific expression of the genetically encoded Ca^{2+} indicator GCaMP3 to evaluate spontaneous intracellular Ca^{2+} signaling in astrocytes and microglia. Ca^{2+} signals were then characterized in acute *ex vivo* (both gray and white matter) as well as in chronic *in vivo* (white matter) preparations using MSparkles, a MATLAB-based software for automatic detection and analysis of fluorescence events. As a result, we were able to segregate distinct astroglial and microglial Ca^{2+} signaling patterns along with method-specific Ca^{2+} signaling alterations, which must be taken into consideration in the reliable evaluation of any result obtained in physiological as well as pathological conditions. Our study revealed a high degree of Ca^{2+} signaling diversity in glial cells of the murine spinal cord, thus adding to the current knowledge of the astonishing glial heterogeneity and cell-specific Ca^{2+} dynamics in non-neuronal networks.

Keywords: spinal cord, astrocytes, microglia, Ca^{2+}, laminectomy, slice preparation, *in vivo*, 2-photon laser-scanning microscopy

INTRODUCTION

The spinal cord is a highly sophisticated structure required for correct and rapid information transmission and processing (Bican et al., 2013; DeSai et al., 2021; Harrow-Mortelliti et al., 2021). In transverse sections, the spinal cord displays a distinct compartmentalization into white matter tracts containing neuronal fibers and a central gray matter region containing most of the neuronal cell bodies (Anderson et al., 2009). In both regions glial cells ensure alongside neurons reliable spinal network function and response upon physiological (such as somatosensory inputs) or pathological

(such as neuropathic pain, inflammation, and spinal cord injury) stimuli. The attribution of glial cells to the correct functioning central nervous system has recently led to the comprehensive concept of an *active milieu* to point at the dynamic and reciprocal interactions between neuronal and glial compartments as well as extracellular space, extracellular matrix and vasculature that occur at any time within the nervous tissue (Semyanov and Verkhratsky, 2021). In particular, spinal cord injury induces robust alterations in both astroglial and microglial cellular phenotypes and activity around the lesion (Gaudet and Fonken, 2018; Hassanzadeh et al., 2021). Acute and sub-acute triggered, astroglial response fully develops in the range of days after the insult (Silver and Miller, 2004; Okada et al., 2006; Sofroniew and Vinters, 2010; Cregg et al., 2014; Fan et al., 2016; Liddelow et al., 2017; Li et al., 2019, 2020), whereas microglia can react in the scale of seconds or minutes (Prewitt et al., 1997; Dibaj et al., 2010; David and Kroner, 2011; Kopper and Gensel, 2018; Bellver-Landete et al., 2019; Kolos and Korzhevskii, 2020).

It is known since decades that glial cells undergo complex changes of internal Ca^{2+} concentration ($[Ca^{2+}]_i$), which represent a key read-out of glial activity and reactivity (Verkhratsky et al., 1998; Verkhratsky, 2006). In particular, astroglia exhibit highly dynamic intra- as well as intercellular Ca^{2+} signaling (Khakh and McCarthy, 2015; Caudal et al., 2020), both spontaneously (Araque et al., 1999; Parri et al., 2001; Nett et al., 2002; Haustein et al., 2014; Bindocci et al., 2017) as well as in response to extracellular inputs (Bazargani and Attwell, 2016; Panatier and Robitaille, 2016; Perea et al., 2016; Mariotti et al., 2018; Nagai et al., 2019; Kofuji and Araque, 2020). Importantly, neuropathological conditions (Bezzi et al., 2001; Rossi et al., 2005; Kuchibhotla et al., 2009; Carmignoto and Haydon, 2012; Hamby et al., 2012; Lee et al., 2013; Jiang et al., 2016; Mizuno et al., 2018; Shigetomi et al., 2019) as well as mechanical and biochemical insults (Shigetomi et al., 2019) perturb astroglial Ca^{2+} signaling, which in turn can mediate the cellular response and reactive phenotype. Microglia also display fast $[Ca^{2+}]_i$ changes (from a millisecond and up to minute range) due to the presence of Ca^{2+}-permeable membrane ion channels (Möller, 2002; Kettenmann et al., 2011) as well as in response to a plethora of extracellular ligands (Ferrari et al., 1996; Nolte et al., 1996; Möller et al., 1997; Toescu et al., 1998; Biber et al., 1999; Visentin et al., 1999; Noda et al., 2000; Kuhn et al., 2004; Bianco et al., 2005; Light et al., 2006). Microglial Ca^{2+} signals correlate *in situ* with microglial reactive phenotype (Hoffmann et al., 2003; Färber and Kettenmann, 2006; Haynes et al., 2006; Ikeda et al., 2013; Heo et al., 2015; Michaelis et al., 2015; Korvers et al., 2016) and were recorded *in vivo* at low frequency, in response to damage-induced ATP release (Eichhoff et al., 2011; Pozner et al., 2015; Brawek et al., 2017). Notably, hypoactive shifts in neuronal activity (Brawek et al., 2014; Umpierre et al., 2020) as well as neuronal hyperactivity during kainate induced-status epilepticus and after chemogenetic artificial activation (Umpierre et al., 2020) increase the frequency of microglial Ca^{2+} signals *in vivo*. Nevertheless, as for astroglia, the microglial reactive phenotype and subsequent inflammatory response involve $[Ca^{2+}]_i$ variations, which may add to different extents on the microglial contribution to several pathophysiological conditions (Glass et al., 2010; Perry et al., 2010; Kettenmann et al., 2011; Brawek and Garaschuk, 2013; Ransohoff and El Khoury, 2015).

To date, the detailed characterization of glial Ca^{2+} signaling in the spinal cord has been facing up to its limited accessibility and the extensive manipulation required to either obtain acute slice preparations or perform acute and chronic *in vivo* imaging (Cupido et al., 2014; Cartarozzi et al., 2018; Nelson et al., 2019). In comparison to spinal cord neuronal Ca^{2+} signaling (Johannssen and Helmchen, 2010; Nishida et al., 2014; Sekiguchi et al., 2016), little is known about astroglial Ca^{2+} activity (Cirillo et al., 2012; Sekiguchi et al., 2016) and none, to our knowledge, about spinal microglial Ca^{2+} activity. It is therefore unknown if under physiological conditions these glial cell types display similar Ca^{2+} changes to other CNS regions or whether they exhibit distinct specifications. In addition, it needs to be elucidated to which extent their activity is affected by the experimental procedure required to access them, i.e., acute slice preparation (*ex vivo*) and chronic window implantation for *in vivo* imaging. Here, we provide a comprehensive analysis of Ca^{2+} signals in astroglia and microglia of the murine spinal cord using transgenic mice with cell-type specific expression of a genetically encoded Ca^{2+} indicator (GCaMP3), thus adding on the long-lasting and still ongoing research on the heterogeneity of glial Ca^{2+} signaling.

MATERIALS AND METHODS

Animals

Mice were maintained in the animal facility of the Center for Integrative Physiology and Molecular Medicine (CIPMM, University of Saarland, Homburg). Humidity and temperature were maintained at 45–65% and 20–24°C and the facility was kept under a 12 h light-dark cycle. All mice received food *ad libitum* (standard autoclaved rodent diet, Ssniff Spezialdiäten, Soest, Germany) and autoclaved tap water. Transgenic hGFAP-Cre^{ERT2} mice [Tg(GFAP-cre/ERT2)1Fki, MGI:4418665] (Hirrlinger et al., 2006) and knock-in CX_3CR_1-Cre^{ERT2} mice [Cx3cr1$^{tm2.1(cre/ERT2)Jung}$, MGI: 5467985] (Yona et al., 2013) were crossbred to mice with Rosa26 reporter mice [Gt(ROSA)26Sor$^{tm1(CAG-GCaMP3)Dbe}$, MGI: 5659933] (Paukert et al., 2014). To induce GCaMP3 expression, tamoxifen was administered intraperitoneally for three consecutive days (once per day, 100 mg/kg body weight) (Jahn et al., 2018) at 10 weeks of age. Spinal cord laminectomy, acute slice preparation, 2P-LSM and IHC were performed at 12–13 weeks of age.

Laminectomy and Spinal Window Implantation

All surgical sections were realized in animals under inhalational anesthesia (1.5–2% isoflurane, 66% O_2 and 33% N_2O) and the animal's eyes were covered by Bepanthen (Bayer, Leverkusen, Germany). Surgeries were adapted and modified from Fenrich et al. (2012) to get access to T12-L2 vertebrae and by laminectomy approach, L4-S1 spinal segments could be exposed. For chronic observations, a modified coverslip was fit on the spinal cord and animals were postoperatively injected subcutaneously with

analgesic and antiphlogistic agents for two consecutive days (Cupido et al., 2014).

Acute Spinal Cord Slice Preparation

After cervical dislocation, spinal T13-L1 segments were dissected and further processed in ice-cold artificial cerebrospinal fluid [aCSF; in mM, 125 NaCl, 2.5 KCl, 2 $CaCl_2$, 1 $MgCl_2$, 1.25 NaH_2PO_4, 25 $NaHCO_3$, and 25 D-glucose, 330 mOsm/l, pH 7.4; adapted from Hirrlinger et al. (2005)] and purged by carbogen. Afterward, longitudinal sections were cut by a vibratome (VT1200 S) (Leica, Nußloch, Germany) with 250 μm thickness, primarily maintained at 37°C for 30 min and subsequently stored at room temperature for further 30 min and during 2P-LSM.

Two-Photon Laser-Scanning Microscopy

To perform *in vivo* and *ex vivo* recordings, a custom-made two-photon laser-scanning microscope (2P-LSM), equipped with a mode-locked Ti:sapphire femto second pulsed laser, Vision II (Coherent, St. Clara, United States) (Dibaj et al., 2010), in combination with ScanImage software (Pologruto et al., 2003) was used. For transgenic GCaMP3 excitation, the laser wavelength was set to 890 nm and the power was adjusted from 8 to 60 mW, depending on the imaging depth in the tissue. 2P-LSM was performed on the white matter of the dorsal funiculus for *in vivo* and *ex vivo* preparations as well as on the dorsal horn gray matter for *ex vivo* preparations up to a 100–150 μm depth (laminae IV and V) by using a long-distance W Plan-Apochromat 20 × 1.0 NA DIC objective (Zeiss, Oberkochen, Germany). Areas of white and gray matter were recorded as uniformly spaced planes of field of views with 256 × 256 pixel per image, 1.4 μs pixel dwell time and GCaMP3 emission was acquired using a 500/24 nm band pass filter, detected by a photomultiplier tube H10770PB-40 (Hamamatsu Photonics, Hamamatsu, Japan). During 2P-LSM *ex vivo* spinal cord slices were continuously perfused with carbogenated aCSF.

Automated ROA-Based Detection and Analysis of Ca^{2+} Events

Ca^{2+}-event analysis was performed using a custom-made analysis software, developed in MATLAB (MSparkles, unpublished). Fluorescence fluctuations at basal Ca^{2+} concentrations (F_0) were computed along the temporal axes of each individual pixel, by fitting a polynomial of user-defined degree in a least-squares sense. Prior to polynomial fitting, potential Ca^{2+} signals were removed for the purpose of F_0 estimation. The range projection of $\Delta F/F_0$ was then used to identify local fluorescence maxima, serving as seed points for simultaneous, correlation-based region growing. Therefore, the correlation of a candidate pixel's fluorescence profile with the fluorescence profile of its corresponding seed point was computed, using Pearsons's linear correlation coefficient. A user-definable correlation threshold was used to stop the region growing process as soon as the temporal evolution of a candidate pixel deviated from its respective seed point (minimum ROA area, 5 μm^2; temporal correlation threshold, 0.2). Pixels belonging to two adjacent regions were marked as boundary pixels. Prior to F_0 estimation, image stacks were denoised using the PURE-LET algorithm (Luisier et al., 2011) as well as a temporal median filter to correct small motion artifacts and simultaneously retain sharp transient edges. Based on the pre-processed data (F), Ca^{2+} event detection and analysis were performed on the normalized dataset ($\Delta F/F_0$) (**Table 1**). MSparkles automatically computed Ca^{2+} signal parameters, such as peak amplitude, duration, Ca^{2+} signal start and end time, ROA area and per-ROA signal frequency. The fluorescence profiles of each ROA were obtained by computing the mean fluorescence among the ROA pixels per recorded time point. ROA areas were obtained by reading the pixel sizes from the image metadata and multiplying them with the individual number of pixels per ROA. Signal durations were computed at full-width at half-maximum (FWHM) of a signal's peak amplitude. Start and end times of a signal were computed as the intersection points of the FWHM with the transient curve. Per ROA signal frequency was computed only if more than one signal was detected within a ROA as the mean signal frequency.

Immunohistochemistry

Anesthetized animals were transcardially perfused with phosphate-buffered saline (PBS) and tissue was fixed by 4% formaldehyde perfusion. After 24 h post fixation in 4% formaldehyde, T13-L1 spinal cord segments were dissected and detached from meninges. The spinal cord tissue was maintained in PBS and cut in transversal or longitudinal sections (40 μm) by vibratome (VT1000 S) (Leica, Nußloch, Germany). Free floating slices were processed for immunohistochemistry (IHC) as described before (Huang et al., 2020). Briefly, incubation in blocking solution (Triton X-100, horse serum and PBS) at RT was followed by primary antibody solution incubation overnight at 4°C for detection of the following glial markers: monoclonal mouse: anti-GFAP (1:500, Novacostra, NCL-GFAP-GA5), anti-GFP (1:500, Abcam, ab1218), polyclonal goat: anti-GFAP (1:1,000, Abcam, ab53554), anti-Iba1 (1:1,000, Abcam, ab5076), polyclonal rabbit: anti-GFP (1:1,000, Clontech, 632593), anti-Iba1 (1:1,000, Wako, 019-19741). Detection of the secondary antibodies (donkey anti-mouse, goat and rabbit secondary antibodies conjugated with Alexa488, Alexa555, Alexa633 and Alexa647; 1:2.000 in PBS; Invitrogen, Grand Island, NY, United States) was executed with the fully automated epifluorescence slide scanner microscope AxioScan.Z1 using the Colibri 7 LED system and appropriate filters (Zeiss, Oberkochen, Germany). Image stacks (5 μm, variance projection) were recorded and analyzed with ZEN blue (Zeiss, Oberkochen, Germany).

Software

For 2P-LSM acquisition, the open-source MATLAB-based software application ScanImage® (Vidrio Technologies, Ashburn, VA, United States) (Pologruto et al., 2003) was used. The custom-made MATLAB-based software MSparkles, GraphPad Prism 8 and Microsoft Office Excel 2016 were used for data analysis. Immunohistochemical data were visualized and modified using the ZEN blue imaging software (Zeiss, Oberkochen, Germany) and the ImageJ collection Fiji. For figure layout, the Adobe

Creative Suite 2021 was used (Adobe InDesign®, Adobe Illustrator®, Adobe Photoshop®).

Unsupervised Clustering Analysis

Clustering analysis was performed using MSparkles output as medians of all signals at Field of View (FOV) level. The data was imported into R Studio R Studio Team (2020). RStudio: Integrated Development for R. RStudio, PBC, Boston, MA URL[1]. Heatmaps of scaled values were generated using the R package *pheatmap()*[2].

Statistics

Unless otherwise stated, data are represented as mean ± SEM of single FOVs. Single datasets were analyzed using a Shapiro–Wilk normality test and represented as FOV medians. Data were compared using an ordinary one-way ANOVA with Bonferroni's multiple comparisons test. Non-linear fitting of the data was performed using a Least-Squares fitting with no weighting method and compared using the extra-sum-of-squares F test. F ratios and relative *p-values* of single curve comparisons are schematically represented as a polygonal diagram and gray-scaled color-coded. For paired comparisons, a Wilcoxon matched pairs signed rank test was used. For statistical analysis, following *p-values* were used: $^{*}p < 0.05$; $^{**}p < 0.01$; $^{***}p < 0.001$, $^{****}p < 0.0001$.

Ethics Statement

All animal experiments were performed at the University of Saarland, Center for Integrative Physiology and Molecular Medicine (CIPMM), in strict accordance with the recommendations to European and German guidelines for the welfare of experimental animals and approved by the "Landesamt für Gesundheit und Verbraucherschutz" of the state of Saarland (animal license number 34/2016, 36/2016, 03/2021 and 08/2021). For 2P-LSM $N \geq 4$ animals were used for each *ex vivo* or *in vivo* experiment (total 20 animals), for immunohistochemical analysis 24 animals were used in total.

RESULTS

Tamoxifen-Induced GCaMP3 Expression in Adult Spinal Cord Astro- and Microglia and Acquisition of Ca^{2+} Signals

In order to record astroglial and microglial Ca^{2+} variations, we took advantage of the inducible DNA recombinase CreERT2 to achieve time-controlled and cell type-specific expression of the genetically-encoded Ca^{2+}indicator GCaMP3 (Paukert et al., 2014) in astroglia under the control of the human glial fibrillary acidic protein promoter (GFAP) and in C-X3-C motif chemokine receptor 1 (CX_3CR_1)-expressing microglia (**Figure 1A**; Hirrlinger et al., 2006; Yona et al., 2013). 10 weeks-old mice with C57BL6/N background were treated with tamoxifen (100 mg/kg body weight, i.p., three times, once per day) to induce the reporter expression in astroglia (for simplicity we will refer to these animals as $hGFAP^{GCaMP3}$ mice) and microglia ($CX_3CR_1{}^{GCaMP3}$ mice, **Figure 1B**). The cellular specificity of the recombination in both gray (*gm*) and white matter (*wm*) of the lumbar spinal cord was confirmed by immunohistochemistry and colocalization with GFAP (**Figures 1C,D**) and Iba1 (**Figures 1C,E**) in longitudinal spinal cord slices. Astroglia displayed the typical protoplasmic and fibrous morphology in *gm* and *wm*, with high recombination efficiencies (78% in *gm* and 87% in *wm* for $GFAP^{+}$ cells). On the other hand, microglial population appeared morphologically homogeneous throughout the tissue with 99% recombination efficiency in *gm* and *wm* for $Iba1^{+}$ cells. To visualize Ca^{2+} changes, 12 weeks-old animals were sacrificed for acute slice preparation and *ex vivo* two-photon laser-scanning microscopy (2P-LSM). Alternatively, they underwent a laminectomy surgery (T13 and L1 vertebrae) in order to expose the spinal cord segments L5 and L6 for chronic *in vivo* 2P-LSM one (*d1*), two (*d2*) and 7 days (*d7*) after surgery (**Supplementary Figures 1A,B**). The absence of an excessive and abnormal cellular reaction after spinal cord surgery was monitored by immunohistochemistry of GFAP and Iba1 in both $hGFAP^{GCaMP3}$ and $CX_3CR_1{}^{GCaMP3}$ mice at each time point of investigation (**Supplementary Figure 1C**).

Astroglial Ca^{2+} Signals Appear at Higher Densities Than Microglia in Acute Slice Preparations

Acute longitudinal slice preparations enabled access to both *gm* and *wm* of the spinal cord. In this work, we recorded

TABLE 1 | Description of parameters used for Ca^{2+} characterization.

Feature	Description	Unit
Amplitude	Local maximum peak within a ROA	$\Delta F/F_0$
Area	Area covered by a ROA in domain units	μm^2
Decay time	Time interval between 90% of the peak value and signal end	s
Duration	Full Width at Half Maximum (FWHM) of the signal curve	s
Frequency	Signal frequency within a chosen ROA based on the mean value of all peak-to-peak times divided by the number of signals associated to that ROA	min^{-1}
Integrated fluorescence	Area under the signal curve in correspondence of the signal duration	$\Delta F/F_0$
Rise time	Time interval between signal start and 90% of the peak value	s
ROA density	Number of ROAs detected within a Field of View (FOV) divided by the FOV area	$10^{-3}/\mu m^2$
Signal density	Number of signals detected within a FOV divided by the FOV area	$10^{-3}/\mu m^2$
Signal start/end	Intersections of the signal curve with the horizontal line corresponding to 50% of the signal peak amplitude	
Coincidence index	Number of simultaneously active ROAs within a FOV normalized to the total number of ROAs	*c.i.*

[1]http://www.rstudio.com/

[2]https://CRAN.R-project.org/package=pheatmap

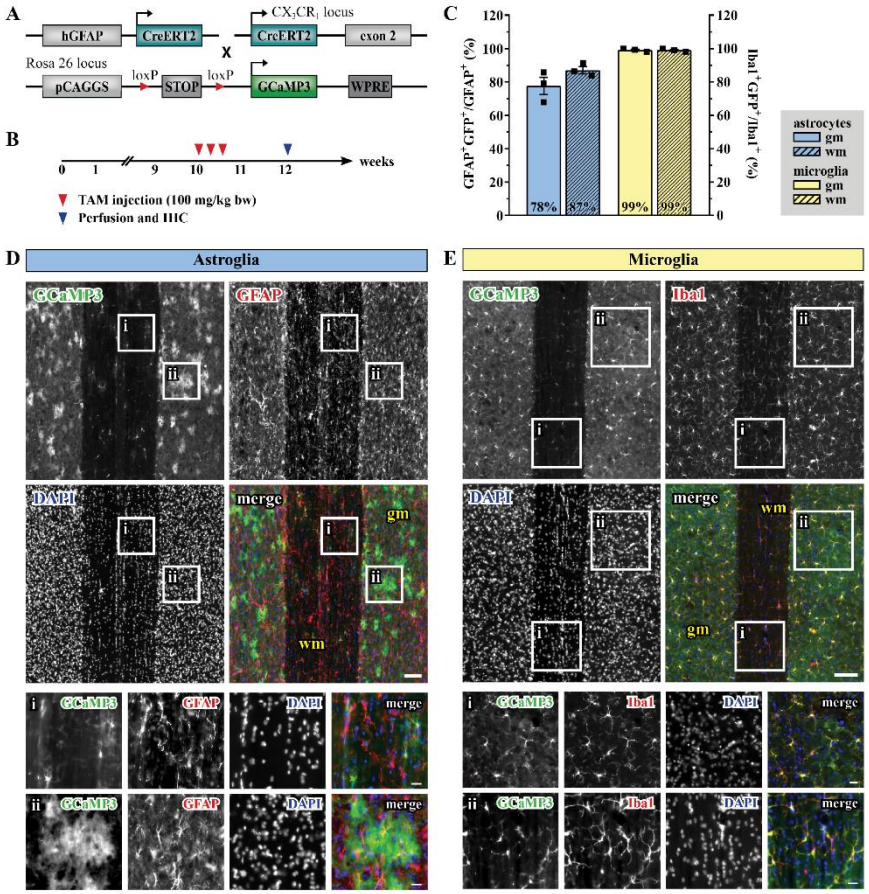

FIGURE 1 | Tamoxifen- induced GCaMP3 expression in astrocytes and microglia. **(A)** Scheme of transgenic constructs carrying CreERT2 and GCaMP3. **(B)** Experimental design for the GCaMP3 induction in 10-weeks old mice injected with TAM (tamoxifen). **(C)** Recombination efficiency for $hGFAP^{GCaMP3}$ (blue, left Y-axis) and $CX_3CR_1^{GCaMP3}$ animals (yellow, right Y-axis) in gray (*gm*; solid) and white matter (*wm*, dashed), respectively. **(D)** Evaluation of longitudinal spinal cord slices for cell-specific GCaMP3 (green) expression in astroglia (GFAP, red) and **(E)** microglia (Iba1, red) with nucleic staining (DAPI, blue). Neither $Iba1^+GCaMP3^+$ nor $GFAP^+$ $GCaMP3^+$ cells were detected in the $hGFAPCre^{ERT2}$ or CX_3CR_1-Cre^{ERT2} animals, respectively. **(Di,Ei)** *wm*, magnified view; **(Dii,Eii)** *gm*, magnified view. Scale bar, 100 μm (overviews) and 20 μm (magnified views).

glial Ca^{2+} signals from the dorsal *wm* and the dorsal horn *gm* and compared them with *in vivo* data collected in the dorsal spinal cord. Astro- and microglial Ca^{2+} data were processed and analyzed using the MATLAB-based analysis software MSparkles (**Table 1** and see section "Materials and Methods" for details), which performed automatic and unbiased detection of regions of activity (ROAs) based on the range projection of $\Delta F/F_0$ and a temporal correlation based region detection algorithm. This approach enabled the detection of stationary ROAs associated with time-dependent fluorescence fluctuations, in contrast to other approaches based on dynamic events with different occurrence, extension and location over time (Cornell-Bell et al., 1990; Jung et al., 1998; Wu et al., 2014; Semyanov et al., 2020). For simplification and a comparison at a glance we collected all numeric values in **Table 2**. Throughout this work we will focus on the parameters that enable a clearer segregation of glial

Ca^{2+} signals, namely signal and ROA density, ROA area, signal frequency and coincidence (in bold in **Table 2**).

Ex vivo astroglial Ca^{2+} imaging confirmed the morphological differences between *gm* and *wm* astrocytes observed in fixed tissue preparations and the expression of GCaMP3 in the entire cellular cytoplasm (**Figures 2A,C** and **Supplementary Videos 1**, **2**). Although similar between *wm* and *gm*, microglia exhibited morphological changes typical of their reactive phenotype with shorter and thicker processes and in some cases even an amoeboid cell body (**Figures 2B,D** and **Supplementary Videos 3**, **4**). Notably, the majority of microglia shared this phenotype irrespective of the imaging depth. Both *gm* and *wm* astrocytes displayed highly dynamic Ca^{2+} oscillations mainly restricted to the gliapil but occasionally involving the somatic compartment, whereas microglia were mostly silent or displayed changes at a lower frequency and were often restricted to single branches. In line with this, the automatic ROA detection analysis revealed different signal density ($10^{-3}/\mu m^2$) between astroglia and microglia in both *gm* ($p < 0.01$) and *wm* ($p < 0.001$) with a ∼3-fold increase in signal density in astroglia compared to microglia (**Figures 3A–C**). No difference was detected within each cell-type between *gm* and *wm*. In parallel to that, both astroglia and microglia did not display any difference in ROA density ($10^{-3}/\mu m^2$) between *gm* and *wm*, whereas in both regions astroglia showed a ∼2.5-fold increase in ROA density (*gm*: $p < 0.001$; *wm*: $p < 0.0001$; **Figure 3D**). A closer look at the signal distribution among the detected ROAs revealed that around half of the ROAs were active only once during the recording time, irrespectively of the total number of active ROAs (**Figure 3E**). Also, the signal frequency for ROAs associated with more than one signal did not differ between regions and cell types and ranged between ∼0.50 and ∼1.50 min^{-1} for astroglia and ∼0.6 and ∼2.5 min^{-1} for microglia (**Table 2**).

In terms of the signal most obvious kinetic properties, namely the amplitude at their maximum peak ($\Delta F/F_0$) and the signal duration, defined as full-width at half maximum (FWHM), most astroglial and microglial signals displayed amplitudes ranging from ∼110 to ∼120% of the baseline fluorescence level with no difference between cell-types or regions. Astroglial Ca^{2+} signals lasted longer in *gm* than in *wm* ($p < 0.05$) as well as microglial *gm* signals ($p < 0.01$, **Table 2**). Additionally, we evaluated the distribution of the signal amplitudes and durations by sorting the

TABLE 2 | Numeric values of Ca^{2+} data in terms of morphology, spatial and temporal distribution (*mean* ± *SEM*).

Astrocytes	***ex vivo***		***in vivo***		
	gm	**wm**	**wm**		
			d1	**d2**	**d7**
Amplitude ($\Delta F/F_0$)	0.14 ± 0.01	0.13 ± 0.01	0.15 ± 0.02	0.14 ± 0.01	0.16 ± 0.01
Coincidence index (c.i.)	**0.07 ± 0.01**	**0.05 ± 0.01**	**0.03 ± 0.01**	**0.04 ± 0.01**	**0.03 ± 0.01**
Decay Time (s)	3.46 ± 0.55	2.32 ± 0.33	2.91 ± 0.49	3.26 ± 0.39	3.49 ± 0.56
Duration (s)	9.06 ± 1.40	5.93 ± 0.76	7.54 ± 1.12	9.21 ± 1.47	7.88 ± 1.14
Integrated fluorescence ($\Delta F/F_0$)	1.60 ± 0.20	1.03 ± 0.14	1.47 ± 0.26	1.62 ± 0.21	1.70 ± 0.36
Relative ROA frequency (%)	**52.80 ± 6.11**	**44.79 ± 2.04**	**68.24 ± 6.13**	**67.07 ± 4.86**	**61.29 ± 8.95**
Rise Time (s)	2.44 ± 0.32	1.75 ± 0.14	2.40 ± 0.50	3.41 ± 1.04	2.07 ± 0.49
ROA area (μm^2)	**36.70 ± 5.02**	**18.61 ± 2.96**	**134.8 ± 33.16**	**102.4 ± 12.26**	**178.5 ± 49.87**
ROA density ($10^{-3}/\mu m^2$)	**3.18 ± 0.35**	**3.18 ± 0.33**	**1.83 ± 0.50**	**1.25 ± 0.21**	**0.89 ± 0.30**
Signal density ($10^{-3}/\mu m^2$)	**6.60 ± 1.42**	**7.68 ± 1.28**	**3.48 ± 1.17**	**2.47 ± 0.52**	**2.39 ± 1.07**
Signal frequency (min^{-1})	0.93 ± 0.06	1.11 ± 0.06	1.05 ± 0.13	1.40 ± 0.19	1.27 ± 0.18
Microglia	***ex vivo***		***in vivo***		
	gm	**wm**	**wm**		
			d1	**d2**	**d7**
Amplitude ($\Delta F/F_0$)	0.14 ± 0.01	0.14 ± 0.01	0.14 ± 0.00	0.13 ± 0.00	0.17 ± 0.02
Coincidence index (c.i.)	**0.04 ± 0.01**	**0.08 ± 0.01**	**0.10 ± 0.01**	**0.09 ± 0.01**	**0.10 ± 0.02**
Decay Time (s)	1.95 ± 0.19	2.33 ± 0.19	3.84 ± 0.59	2.75 ± 0.34	2.76 ± 0.41
Duration (s)	4.97 ± 0.38	6.18 ± 0.46	10.20 ± 1.39	7.29 ± 0.72	7.33 ± 0.93
Integrated fluorescence ($\Delta F/F_0$)	1.37 ± 0.19	1.41 ± 0.16	1.57 ± 0.18	1.16 ± 0.12	1.68 ± 0.38
Relative ROA frequency (%)	**56.40 ± 4.10**	**47.57 ± 3.84**	**36.82 ± 4.55**	**41.83 ± 5.17**	**29.10 ± 5.81**
Rise Time (s)	1.63 ± 0.16	2.04 ± 0.13	3.55 ± 0.57	2.32 ± 0.22	1.67 ± 0.14
ROA area (μm^2)	**15.16 ± 2.99**	**12.37 ± 2.04**	**47.52 ± 4.02**	**52.17 ± 7.97**	**122.0 ± 13.91**
ROA density ($10^{-3}/\mu m^2$)	**1.23 ± 0.30**	**1.31 ± 0.20**	**3.00 ± 0.29**	**2.78 ± 0.26**	**2.79 ± 0.27**
Signal density ($10^{-3}/\mu m^2$)	**2.15 ± 0.57**	**2.81 ± 0.49**	**9.08 ± 1.56**	**8.33 ± 1.54**	**8.70 ± 1.34**
Signal frequency (min^{-1})	1.09 ± 0.14	1.05 ± 0.04	0.95 ± 0.08	0.97 ± 0.09	1.20 ± 0.08

Highlighted values refer to parameters enabling clear data segregation.

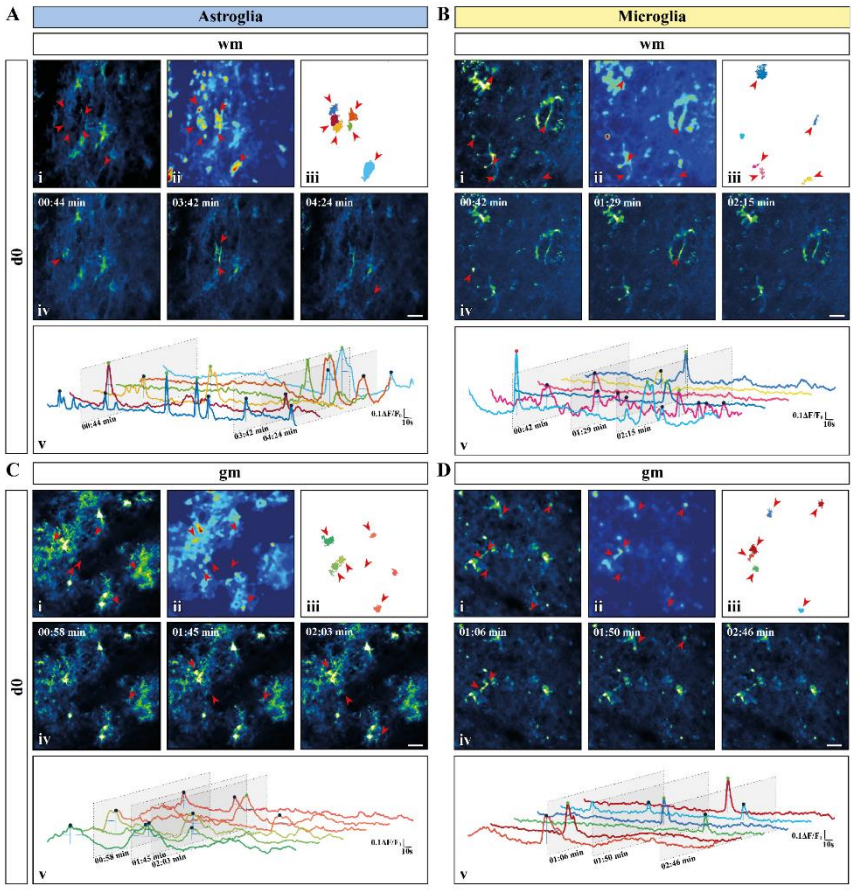

FIGURE 2 | Activity-based Ca^{2+} signaling analysis for astroglia and microglia from acute preparations. **(A–D)** Representative Ca^{2+} signaling analysis for astroglia [**(A)** white matter (*wm*); **(C)** gray matter (*gm*)] and microglia [**(B)** *wm*; **(D)** *gm*] in acute slice preparations using the custom-made MATLAB-based software MSparkles. Maximum-intensity projection of the GCaMP3 signal for representative Fields of View [FOV; scale bar, 20 μm; (i)] over the entire recording time (up to 5 min), absolute intensity projection (ii) and selected regions of activity [ROAs; (iii)] automatically detected using variations in absolute intensity. Red arrows indicate the locations of selected ROAs. Representative time frames from the selected recordings [scale bar, 20 μm; (iv)] with red arrows indicating location of the selected ROAs if active in the displayed time frame. Normalized relative fluorescence intensity traces over time ($\Delta F/F_0$) for the selected ROAs (v) with trace colors matching colors of the selected ROAs. Oblique sections indicate time points chosen for display. Automatically detected signals were pinpointed and color coded based on signal strength ($\mu + \sigma \leq \Delta F/F_0 \leq \mu + 2\sigma$, blue; $\mu + 2\sigma < \Delta F/F_0 \leq \mu + 3\sigma$, green; $\Delta F/F_0 > \mu + 3\sigma$, red) calculated on the mean value (μ) and the corresponding standard deviation (σ) over all ROAs.

signals according to their amplitude (**Supplementary Figure 2A**) or duration (**Supplementary Figure 2B**) and plotting their relative frequency. Next, we fitted the data with a lognormal distribution using a Least-Squares fitting and compared them using the extra-sum-of-squares F test. The relative frequency curve of the amplitudes of the Ca^{2+} changes recorded *ex vivo* was similar among different regions and between astroglia and microglia. With respect to the signal duration distribution, the oscillations of Ca^{2+} signals displayed higher variations between cell-types than between *gm* and *wm* ($p < 0.0001$). We also provide further analysis of the signal morphology in a two-dimensional space, namely the signal profile along the time axis, by evaluating

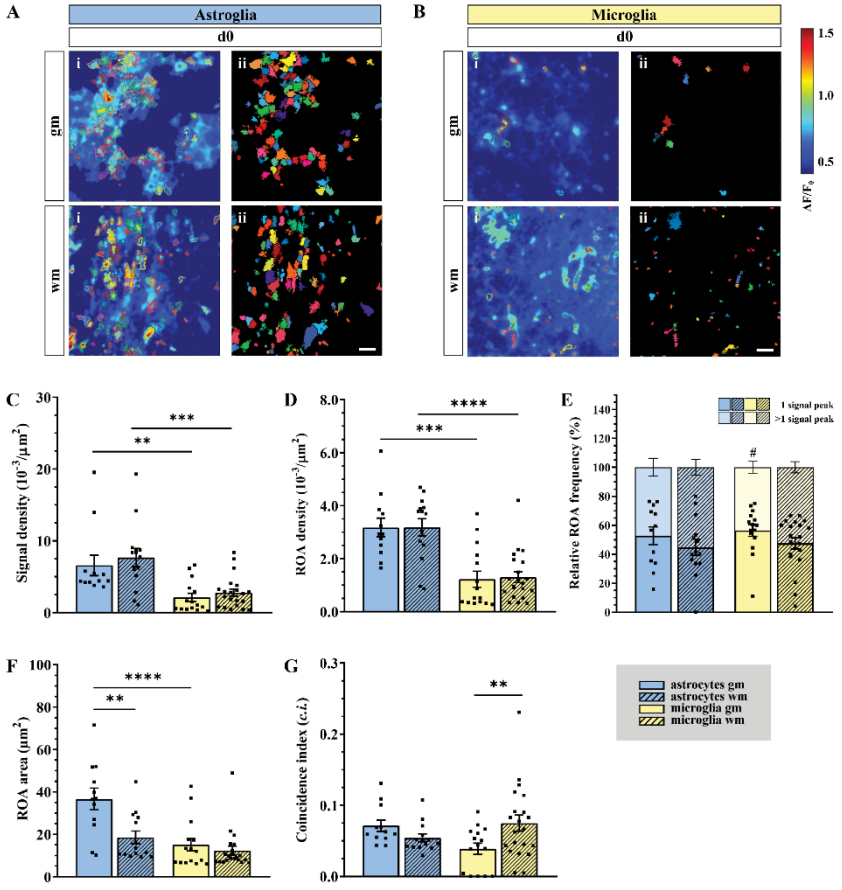

FIGURE 3 | Higher astroglial signal and ROA density in gray and white matter of acute slice preparations (*ex vivo*). **(A,B)** Automatic analysis of detected regions of activity (ROAs) based on absolute fluorescence projection along the temporal axis for astroglia [**(A)** blue] and microglia [**(B)** yellow] in *gm* and *wm* of acute slice preparations (*d0*) with absolute fluorescence projections (i) overlapped with the edges of the detected ROAs [depicted as solid areas in panel (ii)]. **(C)** Signal and **(D)** ROA density in *gm* (solid) and *wm* (dashed). **(E)** Relative frequency of ROAs active once (lower bars) or more than once (upper bars) over the recording time. **(F)** ROA area and **(G)** mean relative number of simultaneously active ROAs over the total recording time calculated as coincidence index (*c.i.*). Data represented as mean ± SEM of single FOVs. Single datasets were analyzed using a Shapiro–Wilk normality test and represented as FOV medians. **(C–G)** Data were compared using an Ordinary one-way ANOVA with Bonferroni's multiple comparisons test. For each group in panel **(E)**, the relative numbers of ROAs presenting one or more signal peaks were analyzed using a Wilcoxon matched pairs signed rank test. *N* (animals) = 4 (astroglia), 5 (microglia, *gm*), 6 (microglia, *wm*). *n* (FOVs) = 12 (astroglia, *gm*), 14 (astroglia, *wm*), 15 (microglia, *gm*), 22 (microglia, *wm*). , $^{*}p < 0.05$; $^{**}p < 0.01$; $^{***}p < 0.001$; $^{****}p < 0.0001$.

the signal integrated fluorescence ($\Delta F/F_0$) as well as the rise and decay time (s) (**Table 2**). In line with the signal duration, astroglial *gm* changes displayed a higher integrated fluorescence as well as longer rise and decay times compared to astroglial signals in the *wm*, whereas microglial integrated fluorescence did not differ between the two regions.

In terms of spatial distribution of the Ca^{2+} elevations, microglial ROAs had the same area (μm^2) in the dorsal *gm* and *wm*, whereas astroglial ROAs displayed a ~2-fold increase in their extension in the *gm* ($p < 0.01$; **Figure 3F**). In line with this, the comparison of the relative frequency distributions of the ROA areas (**Supplementary Figure 2C**) confirmed that active

astroglial ROAs in the *gm* were larger than in the *wm* ($p < 0.0001$) and microglial ROAs in the same region ($p < 0.0001$). Notably, microglia in the *gm* had a higher relative number of smaller ROAs compared to the *wm* ($p < 0.0001$). Finally, we analyzed the signals based on their coincident appearance and calculated the relative number of ROAs active at a given time point (coincidence index, *c.i.*, **Figure 3G**). We found that astroglial Ca^{2+} changes were similarly active between *gm* and *wm*, whereas microglial changes were less coincident in *gm* ($p < 0.05$).

In vivo Microglial Ca^{2+} Changes Are Characterized by a Higher Density and Coincidence but Smaller Areas

To provide a comprehensive study of astroglial and microglial Ca^{2+} events *in vivo* we used chronic 2P-LSM of the dorsal spinal cord *wm* tracts and compared them with the Ca^{2+} dynamics recorded in acute *wm* slice preparations (*ex vivo*). Following chronic spinal cord window implantation, $hGFAP^{GCaMP3}$ and $CX_3CR_1^{GCaMP3}$ mice were analyzed in slightly anesthetized conditions (1.5% isoflurane, 66% O_2 and 33% N_2O) at three different time points (*d1*, *d2,* and *d7*, **Figure 4** and **Supplementary Figure 1A**). The cytosolic GCaMP3 expression confirmed the absence of any obvious structural reactive phenotype as previously shown by immunohistochemistry (**Figures 4**, **5A** and **Supplementary Videos 5–10**). The quantification of spontaneous Ca^{2+} events revealed higher signal densities ($10^{-3}/\mu m^2$) for *wm* microglia *in vivo* (*d1*: $p < 0.001$; *d2*: $p < 0.01$; *d7*: $p < 0.01$) compared to acute slice preparations (*d0*). In contrast to that, astrocytes showed lower signal numbers *in vivo* at *d2* ($p < 0.01$) and *d7* ($p < 0.05$) compared to *ex vivo* preparations (*d0*), and for each time point compared to microglia *in vivo* ($p < 0.01$) (**Figures 5A–C**). In line with this, we found that astrocytes displayed a ∼2-fold reduction in ROA density ($10^{-3}/\mu m^2$) *in vivo* (*d1*: $p < 0.05$; *d2*: $p < 0.0001$; *d7*: $p < 0.0001$) compared to *ex vivo*. Notably, the astroglial ROA density decreased over time from acute (*d1*) to the chronic phase (*d7*) *in vivo*. Contrarily, *in vivo* microglia (*d1*: $p < 0.001$; *d2*: $p < 0.01$; *d7*: $p < 0.05$) displayed a twofold increase in ROA density compared to *ex vivo* recordings as well as to astrocytes from *d2* (*d2*: $p < 0.0001$; *d7*: $p < 0.0001$). This finding showed an opposite trend from the *ex vivo* slice preparations, where we found lower ROA density for microglia compared to astroglia (**Figure 5D**). When we looked at the relative number of ROAs (%) associated with either one or more peaks during the acquisition, we found, in contrast to their equal distribution in *ex vivo* recordings, an almost twofold higher percentage of ROAs with only one peak compared to the ROAs with more than one peak for astrocyte recordings *in vivo*. On the other hand, microglial Ca^{2+} signals displayed an opposite phenotype with a higher percentage of ROAs characterized by more than one peak (**Figure 5E**). The signal frequency (min^{-1}) of the active ROAs (>1 signal peak) did not display any difference for *in vivo* or *ex vivo* recordings or between the cell-types (**Table 2**).

No difference was detected in terms of signal amplitude as well as signal duration (**Table 2**). In line with this, the relative frequency distribution of glial signal amplitudes displayed only minor or no differences for astroglia (*d1*∼*d2*∼*d7*) and compared to microglia. In contrast to astrocytes, the signal amplitudes of microglia varied among chronic recordings ($p < 0.0001$) and compared to *ex vivo* slice recordings (*d1*: $p < 0.001$; *d2*: $p < 0.0001$; *d7*: $p < 0.0001$). Notably, the difference of microglial amplitude frequency distributions between *in vivo* and *ex vivo* conditions increased over time from *d1* to *d7* (**Supplementary Figure 3A**). The signal durations of astrocytes were longer *in vivo* than *ex vivo* but became more similar along the investigated time points (*d1*: $p < 0.0001$; *d2*: $p < 0.0001$; *d7*: $p < 0.0001$). Furthermore, microglia displayed the longest signal durations at *d1* in comparison to *d2* ($p < 0.0001$) and *d7* ($p < 0.001$) but also to acute *ex vivo* slice preparations ($p < 0.0001$) and regarding to astroglia (*d1*, $p < 0.0001$, **Supplementary Figure 3B**). As it was the case for the acute slice preparations, the integrated fluorescence of the Ca^{2+} signals as well as their rise and decay time did not display any difference either between *in vivo* and *ex vivo* recordings or between the two cell types (**Table 2**). The area (μm^2) of *in vivo* Ca^{2+} signals was more than five times larger than *ex vivo* for astrocytes (*d1*: $p < 0.01$; *d2*: $p < 0.05$; *d7*: $p < 0.0001$) and at least four times larger for microglia. In particular, we found that both astroglia and microglia displayed a larger ROA area 1 week after the window implantation (*d7*), whereas in the acute phase (*d1-d2*) only astroglial signals were associated with larger ROA areas (**Figure 5F**). The relative frequency distribution of the ROA areas also showed that *in vivo* astrocytes ($p < 0.0001$) and microglia ($p < 0.0001$) were highly different to *ex vivo* recordings. On the other hand, there were only minor differences among the astroglial datasets *in vivo* and between the early *in vivo* recordings of microglia (*d1-d2*). We found no difference between astroglia and microglia at *d7*, but the ROA area was strongly reduced in microglia compared to astrocytes at *d1* and *d2* ($p < 0.0001$, **Supplementary Figure 3C**). We then assessed the relative number of simultaneously active ROAs in the FOV space, revealing two to three times more coincidently active ROAs in *in vivo* recordings in microglia compared to astroglia (**Figure 5G**).

To finalize our comparison, we performed a cluster analysis on all parameters provided by MSparkles, aiming at identifying specific segregation patterns within the presented data (**Supplementary Figure 4**). Since we could not clearly distinguish microglia and astrocytes (**Supplementary Figure 4A**), we separated the two cell types and could find only a partial segregation of the microglial data between *ex* and *in vivo* recordings (**Supplementary Figures 4B,C**).

DISCUSSION

In this work, we determined the characteristics of physiological Ca^{2+} dynamics of astrocytes and microglia in the murine spinal cord employing *in vivo* and *ex vivo* two-photon laser-scanning microscopy (2P-LSM) of transgenic mice expressing the genetically encoded Ca^{2+} indicator GCaMP3. To compare glial Ca^{2+} dynamics, we took advantage of a custom-made MATLAB-based analysis software (MSparkles) that identifies fluorescence

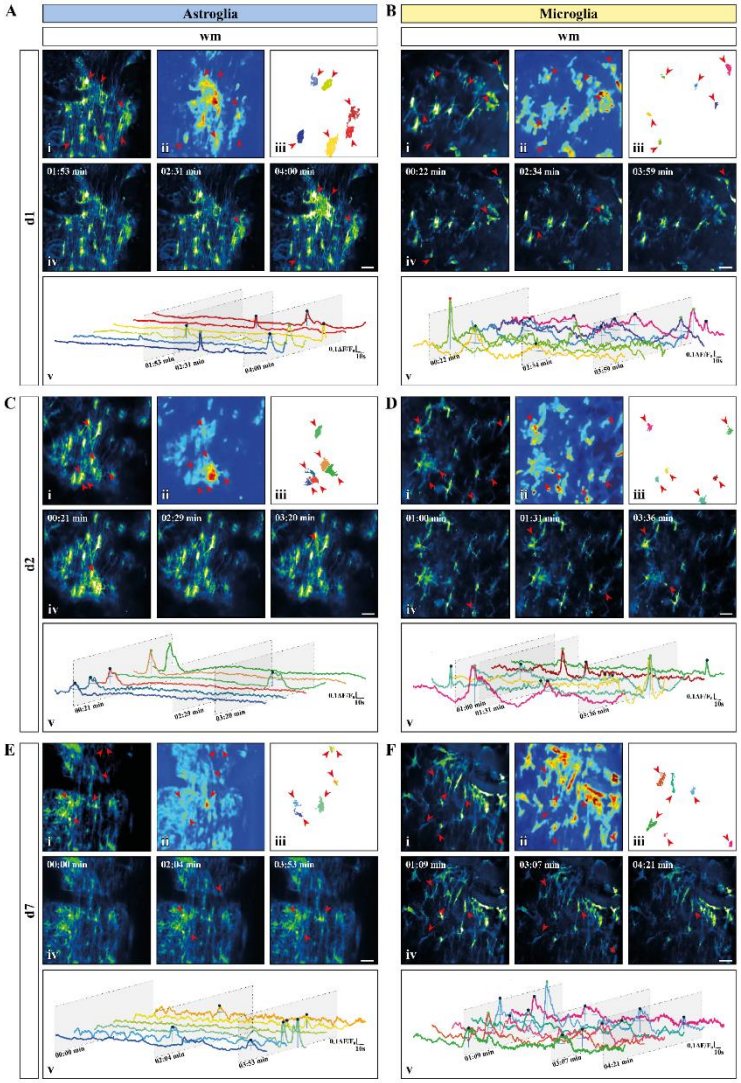

FIGURE 4 | Activity-based *in vivo* Ca^{2+} signaling analysis for astro- and microglia after chronic window implantation. **(A–F)** Representative Ca^{2+} signaling analysis for **(A,C,E)** astroglia and **(B,D,F)** microglia monitored *in vivo* [**(A,B)** day one (*d1*); **(C,D)** day two (*d2*); **(E,F)** day 7 (*d7*)] using the custom-made MATLAB-based software MSparkles. Maximum-intensity projection of GCaMP3 signals for representative FOV [scale bar, 20 μm; (i)] over the entire recording time (up to 5 min), absolute intensity projection (ii) and selected regions of activity [ROAs; (iii)] automatically detected using variations in the absolute intensity. Red arrows indicate location of the selected ROAs with representative time frames from the selected recordings [scale bar, 20 μm; (iv)]. Red arrows indicate the location of the selected ROAs if active in the displayed time frame. Normalized relative fluorescence intensity traces over time ($\Delta F/F_0$) for the selected ROAs (v) with trace colors matching the colors of the selected ROAs and oblique sections indicating the time points chosen for display. Automatically detected signals were pinpointed and color coded based on signal strength ($\mu + \sigma \leq \Delta F/F_0 \leq \mu + 2\sigma$, blue; $\mu + 2\sigma < \Delta F/F_0 \leq \mu + 3\sigma$, green; $\Delta F/F_0 > \mu + 3\sigma$, red) calculated on the mean value (μ) and the corresponding standard deviation (σ) over all ROAs.

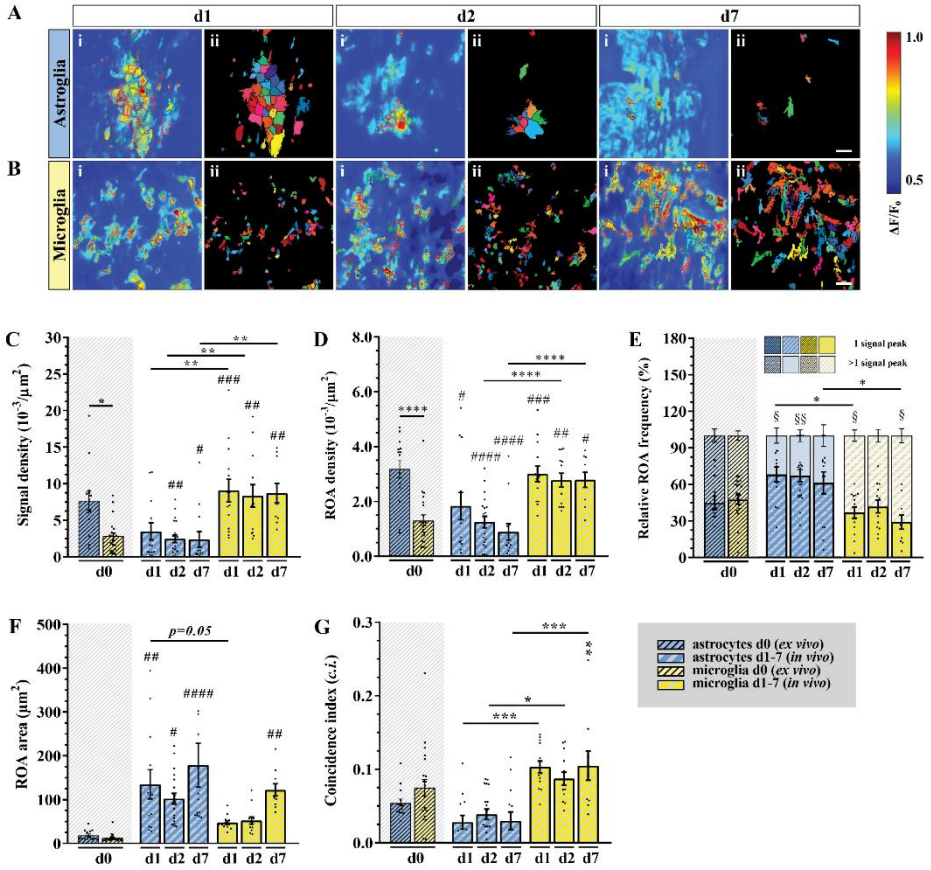

FIGURE 5 | *In vivo* microglial Ca^{2+} signals showed higher signal and ROA densities as well as smaller areas and a higher temporal coincidence. **(A,B)** Automatic detected ROAs based on absolute fluorescence projections along the temporal axis for astroglia (blue) and microglia (yellow) *in vivo* (*d1*, *d2* and *d7*, *wm*). Absolute fluorescence projections (i) were overlapped with the edges of the detected ROAs [depicted as solid areas in panel (ii)]. **(C)** Signal and **(D)** ROA density. **(E)** Relative frequency of ROAs active once (lower bars) or more than once (upper bars) over the recording time. **(F)** ROA area and **(G)** mean relative number of simultaneously active ROAs over the total recording time calculated as coincidence index (*c.i.*). *Ex vivo* (*d0*) *wm* data were placed next to the *in vivo* data for direct comparison. **(C–G)** Data were represented as mean ± SEM of single FOVs. Single datasets were analyzed using a Shapiro–Wilk normality test and represented as FOV medians. Data were compared using an Ordinary one-way ANOVA with Bonferroni's multiple comparisons test. Comparisons between *in vivo* and *ex vivo* data were displayed on top of the single bars. For each group in panel **(E)**, the relative numbers of ROAs presenting one or more signal peaks were analyzed using a Wilcoxon matched pairs signed rank test. *N* (animals) = 4 (astroglia, *d0*), 4-6-4 (astroglia, *in vivo*, *d1-d7*), 6 (microglia, *d0*), 4 (microglia, *in vivo*, *d1-d7*). *n* (FOVs) = 14 (astroglia, *d0*), 13-20-13 (astroglia, *in vivo*, *d1-d7*), 22 (microglia, *d0*), 14-13-10 (microglia, *in vivo*, *d1-d7*). *, $^{\#}$, $^{\S}p < 0.05$; **, $^{\#\#}$, $^{\S\S}p < 0.01$; ***, $^{\#\#\#}p < 0.001$; $^{****}p < 0.0001$.

changes in an unbiased and morphology independent manner and determines signal peak as well as region of activity (ROA) associated parameters. Our analysis revealed that microglia have a strongly reduced signal as well as ROA density in *ex vivo* preparations compared to astroglia (**Figures 3C,D**). Notably, this is not associated with overall differences in astro- and microglial signal frequency within each active ROA (**Figure 3E** and **Table 2**). In contrast to this, *in vivo* microglia show higher signal and ROA density than astrocytes (**Figures 5C,D**). This opposite findings between *ex vivo* and *in vivo* recordings may be due to an activation of astrocytes and microglia resulting from the excessive manipulation required for spinal cord extraction

and acute slice preparation resulting in an excessively high (astrocytes) or excessively low (microglia) Ca^{2+} activity in line with the change of microglia morphology to a more amoeboid appearance in slices. It was recently shown for the brain that astroglial Ca^{2+} dynamics differ between *ex vivo* and *in vivo* (as well as *in situ*) recordings (Müller et al., 2021) supporting our results. Astroglial ROA densities decrease *in vivo* along the imaging sessions, possibly hinting that higher ROA densities are associated with an alteration of astroglial signaling in the acute phase after laminectomy non-detectable by reactive markers. Also, glial Ca^{2+} signaling is differentially affected by anesthesia used during the *in vivo* recording. In line with our observations, previous work shows a reduced Ca^{2+} activity in astroglia both in brain and spinal cord (Thrane et al., 2012; Poskanzer and Yuste, 2016; Sekiguchi et al., 2016; Schweigmann et al., 2021) and an increased Ca^{2+} activity in microglia in the brain under anesthesia (Umpierre et al., 2020). Although microglial ROA density is higher *in vivo*, the ROA area itself is smaller than for astrocytes both *ex vivo* and *in vivo* in the early phase (*d1* and *d2*) after the window implantation (**Figures 3F**, **5F**), suggesting that activated microglial Ca^{2+} dynamics are reduced compared to physiological conditions. In line with this, our recordings showed that astroglia display concerted Ca^{2+} waves beyond the extension of single cells, whereas microglial Ca^{2+} signaling is mainly restricted to single processes in acute slices and directly after spinal cord window surgery.

In terms of 3D structural properties of the single Ca^{2+} changes (amplitude, duration, integrated fluorescence, rise and decay time), we found no substantial differences between astrocytes and microglia as well as between *ex vivo* and *in vivo* recordings (**Table 2**). We conclude that the characterization of spontaneous Ca^{2+} changes in terms of commonly assessed parameters (as amplitude and duration) or even more sophisticated geometrical descriptive parameters (such as integrated fluorescence, rise and decay time) cannot enable a successful segregation of glial Ca^{2+} dynamics even if collectively assessed as we did using a clustering analysis (**Supplementary Figure 4**). This suggests that glial cells may share some common mechanisms underlying Ca^{2+} signaling or that cell-specific pathways originate similar cytosolic Ca^{2+} elevations and that the different glial Ca^{2+} dynamics arise from the temporal and spatial control of otherwise similar signals at the cellular or network level. Indeed, it is known since decades that glial cells share some common mechanisms at the basis of intracellular Ca^{2+} mobilization (Verkhratsky and Kettenmann, 1996; Deitmer et al., 1998). Nevertheless, pharmacological as well as genetic approaches aiming at interfering with putative molecular mechanisms underlying Ca^{2+} fluctuations are required to draw any conclusion on this point.

In acute spinal cord preparations, microglia display similar Ca^{2+} signaling properties between gray (*gm*) and white matter (*wm*; **Figure 3**) whereas astroglial Ca^{2+} signals last longer (**Table 2**) and have a larger extension (**Figure 3F**) in *gm* compared to *wm*. This finding suggests that diverse Ca^{2+} dynamics might be due to the morphological heterogeneity of astroglia that can be clearly observed between *gm* and *wm* (**Figure 1**) in line with previous evidence obtained in the brain showing less coupling of *wm* fibrous astrocytes (mainly though connexin 43) compared to *gm* protoplasmic astroglia (through connexins 43 and 30) (Lee et al., 1994; Haas et al., 2006). In addition, astroglial Ca^{2+} waves in *wm*, in contrast to the neocortical *gm*, mainly propagate through ATP release (Schipke et al., 2002; Hamilton et al., 2008). Also, *gm* and *wm* astroglia receive different glutamatergic inputs given their close proximity with the neuronal synapses in the *gm* and the relatively lower level of glutamate release from neuronal axons in the *wm* (Kukley et al., 2007; Ziskin et al., 2007; Wake et al., 2011). Taken together, these data point at the existence of a regional specificity for astroglial Ca^{2+} signaling which reflects the cellular heterogeneity between *gm* and *wm* (Köhler et al., 2021). On the other hand, microglial Ca^{2+} dynamics display a substantial uniformity between *gm* and *wm*, in line with the absence of morphological regional differences.

The monitoring of astroglial and microglial Ca^{2+} dynamics for up to 7 days after laminectomy and chronic window implantation enabled the evaluation of putative specific glial responses to the manipulation required for *in vivo* imaging (**Figure 5**). In particular, microglia display a more differential phenotype between the acute phase (*d1* and *d2*) after laminectomy and the later chronic phase (*d7*) than astroglia. Microglia signals are characterized by higher duration and smaller area in the acute phase and with higher amplitude, lower duration and larger area in the chronic phase. Moreover, a closer look at the relative signal frequency distributions revealed higher similarities for astroglia in terms of amplitude as well as duration, whereas microglial signal distribution displayed a high heterogeneity along the recording time points. Notably, signal amplitude and duration distribution of astroglia and microglia become more and more similar with time. Similar findings were obtained from the analysis of the distribution of the ROA areas, thus suggesting that *in vivo* glial cell are similar in the chronic phase but differ after acute activation following the perturbation of the surrounding environment. This is in line with evidence supporting the different response kinetics of spinal cord microglia (Prewitt et al., 1997; Dibaj et al., 2010; Bellver-Landete et al., 2019) and astrocytes (Okada et al., 2006; Fan et al., 2016; Li et al., 2019, 2020) in response to external stimuli. This may also underline the differences observed between astroglia and microglia in acute slice preparations, since the experimental procedure required to collect the tissue constitutes a significant challenge to the physiology of the spinal cord. In line with this, microglial signal amplitude distribution becomes progressively more different than the signal distribution from *ex vivo* recordings along the experimental time points, suggesting a progressive restoration of the physiological status disrupted after spinal cord slice collection or window implantation. To test the nature of glial Ca^{2+} reactive phenotype, we propose to acutely challenge glial Ca^{2+} dynamics *in vivo* by means of focal application of mechanical (e.g., laser induced) as well as chemical (e.g., DAMPs such as ATP) perturbative stimuli to trigger event-based Ca^{2+} signaling.

Finally, with respect to the temporal dynamics of astro- and microglial Ca^{2+} signaling, we showed that both glial cell populations are associated with the same signal frequency but different activity (i.e., relative number of ROAs active once or more than once during the recording time) (**Figure 5E**) as well as

a different extent of coincident activity (**Figure 5G**). In particular, the relative frequency of astroglial ROAs with more than one peak *in vivo* is higher compared to microglial ROAs, while the signal frequency is not changed between the two cell types. In parallel to that, astroglia display a lower coincidence index compared to microglia. The enhanced microglial coincidence *in vivo* is likely due to their constant dynamic scanning of the surrounding environment since microglial Ca^{2+} changes were shown to precede cell motility in the brain (Umpierre et al., 2020). In addition to that, glial Ca^{2+} dynamics might be the result of a differential cell responsivity to their neuronal counterpart. This study was conceptualized minimizing the interference of the neuronal network *in vivo* by means of isoflurane anesthesia, thus avoiding the superimposition of a further level of complexity arising from motor as well as sensory stimuli. Nevertheless, the evaluation of glial Ca^{2+} dynamics in awake animals is required to fully elucidate glial heterogeneity and we strongly believe that the evaluation of event triggered Ca^{2+} signaling (like in response to the induction of reflex circuits) will enable the identification of a further layer of glial specificity in terms of Ca^{2+} dynamics.

CONCLUSION

In summary, we performed two-photon laser-scanning microscopy in acute slice preparations and chronic *in vivo* recordings of the mouse spinal cord to simultaneously characterize and compare cell-specific properties of Ca^{2+} signals in astro- and microglia. To this aim, we used specific user-defined parameters and a novel analysis tool to evaluate common and distinct features of spinal glial cells with respect to their physiological Ca^{2+} changes. Accordingly, we conclude that signal and ROA density, ROA area, signal frequency and coincidence are key parameters for the differentiation of glial Ca^{2+} dynamics and are therefore valuable candidates for understanding the highly developed function of astrocytes and microglia in the environment of the mammalian spinal cord. Acute slice preparation as well as the spinal cord surgery influence both astro- and microglial Ca^{2+} dynamics and we found that microglia, as predictable given their surveillance activity, are more susceptible to the experimental manipulation. Nevertheless, the reliable and standardized analysis of Ca^{2+} dynamics remains an open challenge to be addressed in the near future to fully elucidate the role of spinal glial cells in physiology and pathology.

DATA AVAILABILITY STATEMENT

The raw data supporting the conclusions of this article will be made available by the authors, without undue reservation.

ETHICS STATEMENT

The animal study was reviewed and approved by Saarländisches Landesamt für Gesundheit und Verbraucherschutz.

AUTHOR CONTRIBUTIONS

PR and DG equally contributed to the manuscript, conceptualized the project, performed the experiments, analyzed the data, wrote the first draft, and generated the figures. PR performed laminectomy and spinal cord window implantation and prepared the spinal cord tissue for further processing. DG obtained and handled the spinal cord acute preparations. GS developed the ROA-based automatic analysis for image processing. AW contributed to the data analysis and visualization. ED contributed to the data acquisition. FK provided the structural and financial support for the project. AS conceptualized and supervised the project, reviewed and finalized the manuscript and figures. All authors approved on the final version of the manuscript.

FUNDING

This project has received funding from the European Union's Horizon 2020 research and innovation programme under the Marie Skłodowska-Curie Grant Agreement No 722053 and the European Commission Horizon 2020-EU FET Proactive-01-2016 Neurofibres and from the Deutsche Forschungsgemeinschaft DFG (FOR 2289 and SFB 894 and 1158) and Fondation pour l'Aide à la Recherche sur la Sclérose En Plaques et Association Française contre les Myopathies (ARSEP-AFM).

ACKNOWLEDGMENTS

We would like to thank Wenhui Huang, Xianshu Bai, Bogdan Cătălin and Laura C. Caudal for intellectual input. We would also like to thank Daniel Schauenburg and colleagues for expert mouse maintenance and tamoxifen treatment and Frank Rhode for technical assistance.

SUPPLEMENTARY MATERIAL

The Supplementary Material for this article can be found online at: https://www.frontiersin.org/articles/10.3389/fnmol.2022.840948/full#supplementary-material

Supplementary Figure 1 | Chronic spinal cord window implantation induced no abnormal glial cell reactivity. **(A)** Experimental design for the evaluation of the chronic glial cell reactivity after laminectomy and spinal cord window implantation with 10-weeks old mice injected with tamoxifen (TAM) and processed 2 weeks later for either immunohistochemistry (IHC, *d0*) or laminectomy surgery for chronic spinal cord window implantation and subsequently perfusion after 1, 2, or 7 days (*d1*, *d2*, and *d7*). **(B)** Bright field overview of spinal cord tissue exposed through laminectomy and monitored for up to 7 days and relative magnification of the selected areas (i–iii). The regions in correspondence of the removed spinal vertebrae (T13 and L1, left) and the underlying spinal cord segments (L4-L6, S1; right) are indicated. Scale bar, 1 mm (overviews) and 200 μm (magnified views). **(C)** Evaluation of astroglial and microglial reactivity in mice expressing GCaMP3 in astrocytes (blue) or microglia (yellow) stained for GFAP (glial fibrillary acidic protein, red) and Iba1 (green) for astroglial and microglial reactivity, respectively. Cell nuclei were stained with DAPI (blue). Scale bar, 200 μm.

Supplementary Figure 2 | *Ex vivo* distribution of glial signal amplitudes, durations and ROA areas. **(A)** Relative frequency of signal amplitude (divided into 0.1 $\Delta F/F_0$

bins), **(B)** signal duration, divided 2 s bins) and **(C)** ROA area (divided into 5 μm^2 bins) for astroglia (blue) and microglia (yellow) in *gm* (solid) and *wm* (dashed) of acute slice preparations. Data with peak amplitudes greater than 0.7 $\Delta F/F_0$ (0.7 ± 0.5%), durations longer than 40 s (0.1 ± 0.1%) and ROA area greater than 120 μm^2 (0.6 ± 0.2%) were excluded from the representation for easier display. Data were represented as mean ± SEM, fitted with a lognormal curve using a Least-Squares fitting with no weighting method and compared using the extra-sum-of-squares F test. F ratios and relative *p-values* of single curve comparisons were schematically represented as a squared diagram and gray-scaled color-coded. Smaller insets represent magnified views of the fitting curves. *N* (animals) = 4 (astroglia), 5 (microglia, *gm*), 6 (microglia, *wm*). *n* (FOVs) = 12 (astroglia, *gm*), 14 (astroglia, *wm*), 15 (microglia, *gm*), 22 (microglia, *wm*). $^{****}p < 0.0001$.

Supplementary Figure 3 | *In vivo* distribution of glial signal amplitudes, durations and ROA areas. **(A)** Relative frequency of signal amplitude (divided into 0.15 $\Delta F/F_0$ bins), **(B)** signal duration (divided into 2 s bins) and **(C)** ROA area (divided into 25 μm^2 bins) for astroglia (blue) and microglia (yellow) *in vivo* (*d1*, *d2* and *d7*, *wm*) and *ex vivo* (*d0*, *wm*). Data with peak amplitude greater than 0.5 $\Delta F/F_0$ (3.3 ± 1.3%), duration longer than 40 s (0.4 ± 0.3%) and ROA areas larger than 400 μm^2 (5.3 ± 1.8%) were excluded from the representation for easier display. Data were represented as mean ± SEM, fitted with a lognormal curve using a Least-Squares fitting with no weighting method and compared using the extra-sum-of-squares F test. F ratios and relative *p-values* of single curve comparisons were schematically represented as a triangle diagram and gray-scaled color-coded. Non-significantly different curves were plotted as a shared curve (*d1*∼*d2*∼*d7*). Smaller insets represent magnified views of the fitting curves. *N* (animals) = 4 (astroglia, *d0*), 4-6-4 (astroglia, *in vivo*, *d1-d7*), 6 (microglia, *d0*), 4 (microglia, *in vivo*, *d1-d7*). *n* (FOVs) = 14 (astroglia, *d0*), 13-20-13 (astroglia, *in vivo*, *d1-d7*), 22 (microglia, *d0*), 14-13-10 (microglia, *in vivo*, *d1-d7*). $^{+}p < 0.05$; $^{**}p < 0.01$; $^{***}p < 0.001$; $^{****}p < 0.0001$.

Supplementary Figure 4 | Hierarchical clustering of Ca^{2+} signalling data. **(A)** Heatmap of the unsupervised hierarchical clustering of Ca^{2+} signaling data represented as medians of single FOVs and color-coded based on the row *z*-scores for both cell-types, **(B)** astroglia or **(C)** microglia. Datasets were color coded based on cell-type (astroglia, blue; microglia, yellow), experimental procedure (*ex vivo*, light blue; *in vivo*, orange) or spinal cord region (*gm*, gray; *wm*, white).

REFERENCES

Anderson, C. R., Ashwell, K. W., Collewijn, H., Conta, A., Harvey, A., Heise, C., et al. (2009). *The Spinal Cord*. London: Elsevier Ltd.

Araque, A., Parpura, V., Sanzgiri, R. P., and Haydon, P. G. (1999). Tripartite synapses: glia, the unacknowledged partner. *Trends Neurosci.* 22, 208–215. doi: 10.1016/s0166-2236(98)01349-6

Bazargani, N., and Attwell, D. (2016). Astrocyte calcium signaling: the third wave. *Nat. Neurosci.* 19, 182–189. doi: 10.1038/nn.4201

Bellver-Landete, V., Bretheau, F., Mailhot, B., Vallières, N., Lessard, M., Janelle, M. E., et al. (2019). Microglia are an essential component of the neuroprotective scar that forms after spinal cord injury. *Nat. Commun.* 10:518. doi: 10.1038/s41467-019-08446-0

Bezzi, P., Domercq, M., Brambilla, L., Galli, R., Schols, D., De Clercq, E., et al. (2001). CXCR4-activated astrocyte glutamate release *via* TNFalpha: amplification by microglia triggers neurotoxicity. *Nat. Neurosci.* 4, 702–710. doi: 10.1038/89490

Bianco, F., Fumagalli, M., Pravettoni, E., D'Ambrosi, N., Volonte, C., Matteoli, M., et al. (2005). Pathophysiological roles of extracellular nucleotides in glial cells: differential expression of purinergic receptors in resting and activated microglia. *Brain Res. Brain Res. Rev.* 48, 144–156. doi: 10.1016/j.brainresrev.2004.12.004

Biber, K., Laurie, D. J., Berthele, A., Sommer, B., Tölle, T. R., Gebicke-Härter, P. J., et al. (1999). Expression and signaling of group I metabotropic glutamate receptors in astrocytes and microglia. *J. Neurochem.* 72, 1671–1680. doi: 10.1046/j.1471-4159.1999.721671.x

Bican, O., Minagar, A., and Pruitt, A. A. (2013). The spinal cord: a review of functional neuroanatomy. *Neurol. Clin.* 31, 1–18. doi: 10.1016/j.ncl.2012.09.009

Bindocci, E., Savtchouk, I., Liaudet, N., Becker, D., Carriero, G., and Volterra, A. (2017). Three-dimensional Ca(2+) imaging advances understanding of astrocyte biology. *Science* 356:eaai8185. doi: 10.1126/science.aai8185

Brawek, B., and Garaschuk, O. (2013). Microglial calcium signaling in the adult, aged and diseased brain. *Cell Calcium* 53, 159–169. doi: 10.1016/j.ceca.2012.12.003

Brawek, B., Liang, Y., Savitska, D., Li, K., Fomin-Thunemann, N., Kovalchuk, Y., et al. (2017). A new approach for ratiometric *in vivo* calcium imaging of microglia. *Sci. Rep.* 7:6030. doi: 10.1038/s41598-017-05952-3

Brawek, B., Schwendele, B., Riester, K., Kohsaka, S., Lerdkrai, C., Liang, Y., et al. (2014). Impairment of *in vivo* calcium signaling in amyloid plaque-associated microglia. *Acta Neuropathol.* 127, 495–505. doi: 10.1007/s00401-013-1242-2

Carmignoto, G., and Haydon, P. G. (2012). Astrocyte calcium signaling and epilepsy. *Glia* 60, 1227–1233. doi: 10.1002/glia.22318

Cartarozzi, L. P., Rieder, P., Bai, X., Scheller, A., Oliveira, A. L. R., and Kirchhoff, F. (2018). *In vivo* two-photon imaging of motoneurons and adjacent glia in the ventral spinal cord. *J. Neurosci. Methods* 299, 8–15. doi: 10.1016/j.jneumeth.2018.01.005

Caudal, L. C., Gobbo, D., Scheller, A., and Kirchhoff, F. (2020). The paradox of astroglial Ca2 + signals at the interface of excitation and inhibition. *Front. Cell. Neurosci.* 14:609947. doi: 10.3389/fncel.2020.609947

Cirillo, G., De Luca, D., and Papa, M. (2012). Calcium imaging of living astrocytes in the mouse spinal cord following sensory stimulation. *Neural Plast.* 2012:425818. doi: 10.1155/2012/425818

Cornell-Bell, A. H., Finkbeiner, S. M., Cooper, M. S., and Smith, S. J. (1990). Glutamate induces calcium waves in cultured astrocytes: long-range glial signaling. *Science* 247, 470–473. doi: 10.1126/science.1967852

Cregg, J. M., DePaul, M. A., Filous, A. R., Lang, B. T., Tran, A., and Silver, J. (2014). Functional regeneration beyond the glial scar. *Exp. Neurol.* 253, 197–207. doi: 10.1016/j.expneurol.2013.12.024

Cupido, A., Catalin, B., Steffens, H., and Kirchhoff, F. (2014). "Surgical procedures to study microglial motility in the brain and in the spinal cord by *in vivo* two-photon laser-scanning microcopy," in *Confocal and Multiphoton Laser-Scanning Microscopy of Neuronal Tissue: Applications and Quantitative Image Analysis*, eds L. Bakota and R. Brandt (Berlin: Springer), 37–50. doi: 10.1007/978-1-4939-0381-8_2

David, S., and Kroner, A. (2011). Repertoire of microglial and macrophage responses after spinal cord injury. *Nat. Rev. Neurosci.* 12, 388–399. doi: 10.1038/nrn3053

Deitmer, J. W., Verkhratsky, A. J., and Lohr, C. (1998). Calcium signalling in glial cells. *Cell Calcium* 24, 405–416.

DeSai, C., Reddy, V., and Agarwal, A. (2021). *Anatomy, Back, Vertebral Column*. Treasure Island, FL: StatPearls.

Dibaj, P., Nadrigny, F., Steffens, H., Scheller, A., Hirrlinger, J., Schomburg, E. D., et al. (2010). NO mediates microglial response to acute spinal cord injury under ATP control *in vivo*. *Glia* 58, 1133–1144. doi: 10.1002/glia.20993

Eichhoff, G., Brawek, B., and Garaschuk, O. (2011). Microglial calcium signal acts as a rapid sensor of single neuron damage *in vivo*. *Biochim. Biophys. Acta* 1813, 1014–1024. doi: 10.1016/j.bbamcr.2010.10.018

Fan, H., Zhang, K., Shan, L., Kuang, F., Chen, K., Zhu, K., et al. (2016). Reactive astrocytes undergo M1 microglia/macrohpages-induced necroptosis in spinal cord injury. *Mol. Neurodegener.* 11:14. doi: 10.1186/s13024-016-0081-8

Färber, K., and Kettenmann, H. (2006). Functional role of calcium signals for microglial function. *Glia* 54, 656–665. doi: 10.1002/glia.20412

Fenrich, K. K., Weber, P., Hocine, M., Zalc, M., Rougon, G., and Debarbieux, F. (2012). Long-term *in vivo* imaging of normal and pathological mouse spinal cord with subcellular resolution using implanted glass windows. *J. Physiol.* 590, 3665–3675. doi: 10.1113/jphysiol.2012.230532

Ferrari, D., Villalba, M., Chiozzi, P., Falzoni, S., Ricciardi-Castagnoli, P., and Di Virgilio, F. (1996). Mouse microglial cells express a plasma membrane pore gated by extracellular ATP. *J. Immunol.* 156, 1531–1539.

Gaudet, A. D., and Fonken, L. K. (2018). Glial cells shape pathology and repair after spinal cord injury. *Neurotherapeutics* 15, 554–577. doi: 10.1007/s13311-018-0630-7

Glass, C. K., Saijo, K., Winner, B., Marchetto, M. C., and Gage, F. H. (2010). Mechanisms underlying inflammation in neurodegeneration. *Cell* 140, 918–934. doi: 10.1016/j.cell.2010.02.016

Haas, B., Schipke, C. G., Peters, O., Söhl, G., Willecke, K., and Kettenmann, H. (2006). Activity-dependent ATP-waves in the mouse neocortex are independent from astrocytic calcium waves. *Cereb. Cortex* 16, 237–246. doi: 10.1093/cercor/bhi101

Hamby, M. E., Coppola, G., Ao, Y., Geschwind, D. H., Khakh, B. S., and Sofroniew, M. V. (2012). Inflammatory mediators alter the astrocyte transcriptome and calcium signaling elicited by multiple G-protein-coupled receptors. *J. Neurosci.* 32, 14489–14510. doi: 10.1523/JNEUROSCI.1256-12.2012

Hamilton, N., Vayro, S., Kirchhoff, F., Verkhratsky, A., Robbins, J., Gorecki, D. C., et al. (2008). Mechanisms of ATP- and glutamate-mediated calcium signaling in white matter astrocytes. *Glia* 56, 734–749. doi: 10.1002/glia.20649

Harrow-Mortelliti, M., Reddy, V., and Jimsheleishvili, G. (2021). *Physiology, Spinal Cord*. Treasure Island, FL: StatPearls.

Hassanzadeh, S., Jalessi, M., Jameie, S. B., Khanmohammadi, M., Bagher, Z., Namjoo, Z., et al. (2021). More attention on glial cells to have better recovery after spinal cord injury. *Biochem. Biophys. Rep.* 25:100905. doi: 10.1016/j.bbrep.2020.100905

Haustein, M. D., Kracun, S., Lu, X. H., Shih, T., Jackson-Weaver, O., Tong, X., et al. (2014). Conditions and constraints for astrocyte calcium signaling in the hippocampal mossy fiber pathway. *Neuron* 82, 413–429. doi: 10.1016/j.neuron.2014.02.041

Haynes, S. E., Hollopeter, G., Yang, G., Kurpius, D., Dailey, M. E., Gan, W. B., et al. (2006). The P2Y12 receptor regulates microglial activation by extracellular nucleotides. *Nat. Neurosci.* 9, 1512–1519. doi: 10.1038/nn1805

Heo, D. K., Lim, H. M., Nam, J. H., Lee, M. G., and Kim, J. Y. (2015). Regulation of phagocytosis and cytokine secretion by store-operated calcium entry in primary isolated murine microglia. *Cell. Signal.* 27, 177–186. doi: 10.1016/j.cellsig.2014.11.003

Hirrlinger, P. G., Scheller, A., Braun, C., Hirrlinger, J., and Kirchhoff, F. (2006). Temporal control of gene recombination in astrocytes by transgenic expression of the tamoxifen-inducible DNA recombinase variant CreERT2. *Glia* 54, 11–20. doi: 10.1002/glia.20342

Hirrlinger, P. G., Scheller, A., Braun, C., Quintela-Schneider, M., Fuss, B., Hirrlinger, J., et al. (2005). Expression of reef coral fluorescent proteins in the central nervous system of transgenic mice. *Mol. Cell. Neurosci.* 30, 291–303. doi: 10.1016/j.mcn.2005.08.011

Hoffmann, A., Kann, O., Ohlemeyer, C., Hanisch, U. K., and Kettenmann, H. (2003). Elevation of basal intracellular calcium as a central element in the activation of brain macrophages (microglia): suppression of receptor-evoked calcium signaling and control of release function. *J. Neurosci.* 23, 4410–4419. doi: 10.1523/JNEUROSCI.23-11-04410.2003

Huang, W., Bai, X., Meyer, E., and Scheller, A. (2020). Acute brain injuries trigger microglia as an additional source of the proteoglycan NG2. *Acta Neuropathol. Commun.* 8:146. doi: 10.1186/s40478-020-01016-2

Ikeda, M., Tsuno, S., Sugiyama, T., Hashimoto, A., Yamoto, K., Takeuchi, K., et al. (2013). Ca(2+) spiking activity caused by the activation of store-operated Ca(2+) channels mediates TNF-α release from microglial cells under chronic purinergic stimulation. *Biochim. Biophys. Acta* 1833, 2573–2585. doi: 10.1016/j.bbamcr.2013.06.022

Jahn, H. M., Kasakow, C. V., Helfer, A., Michely, J., Verkhratsky, A., Maurer, H. H., et al. (2018). Refined protocols of tamoxifen injection for inducible DNA recombination in mouse astroglia. *Sci. Rep.* 8:5913. doi: 10.1038/s41598-018-24085-9

Jiang, R., Diaz-Castro, B., Looger, L. L., and Khakh, B. S. (2016). Dysfunctional calcium and glutamate signaling in striatal astrocytes from Huntington's disease model mice. *J. Neurosci.* 36, 3453–3470. doi: 10.1523/JNEUROSCI.3693-15.2016

Johannssen, H. C., and Helmchen, F. (2010). *In vivo* Ca2+ imaging of dorsal horn neuronal populations in mouse spinal cord. *J. Physiol.* 588, 3397–3402. doi: 10.1113/jphysiol.2010.191833

Jung, P., Cornell-Bell, A., Madden, K. S., and Moss, F. (1998). Noise-induced spiral waves in astrocyte syncytia show evidence of self-organized criticality. *J. Neurophysiol.* 79, 1098–1101. doi: 10.1152/jn.1998.79.2.1098

Kettenmann, H., Hanisch, U. K., Noda, M., and Verkhratsky, A. (2011). Physiology of microglia. *Physiol. Rev.* 91, 461–553.

Khakh, B. S., and McCarthy, K. D. (2015). Astrocyte calcium signaling: from observations to functions and the challenges therein. *Cold Spring Harb. Perspect. Biol.* 7:a020404. doi: 10.1101/cshperspect.a020404

Kofuji, P., and Araque, A. (2020). G-protein-coupled receptors in astrocyte-neuron communication. *Neuroscience* 456, 71–84. doi: 10.1016/j.neuroscience.2020.03.025

Köhler, S., Winkler, U., and Hirrlinger, J. (2021). Heterogeneity of astrocytes in grey and white matter. *Neurochem. Res.* 46, 3–14.

Kolos, E. A., and Korzhevskii, D. E. (2020). Spinal cord microglia in health and disease. *Acta Naturae* 12, 4–17. doi: 10.32607/actanaturae.10934

Kopper, T. J., and Gensel, J. C. (2018). Myelin as an inflammatory mediator: myelin interactions with complement, macrophages, and microglia in spinal cord injury. *J. Neurosci. Res.* 96, 969–977. doi: 10.1002/jnr.24114

Korvers, L., de Andrade Costa, A., Mersch, M., Matyash, V., Kettenmann, H., and Semtner, M. (2016). Spontaneous Ca^{2+} transients in mouse microglia. *Cell Calcium* 60, 396–406. doi: 10.1016/j.ceca.2016.09.004

Kuchibhotla, K. V., Lattarulo, C. R., Hyman, B. T., and Bacskai, B. J. (2009). Synchronous hyperactivity and intercellular calcium waves in astrocytes in Alzheimer mice. *Science* 323, 1211–1215. doi: 10.1126/science.1169096

Kuhn, S. A., van Landeghem, F. K., Zacharias, R., Färber, K., Rappert, A., Pavlovic, S., et al. (2004). Microglia express GABA(B) receptors to modulate interleukin release. *Mol. Cell. Neurosci.* 25, 312–322. doi: 10.1016/j.mcn.2003.10.023

Kukley, M., Capetillo-Zarate, E., and Dietrich, D. (2007). Vesicular glutamate release from axons in white matter. *Nat. Neurosci.* 10, 311–320.

Lee, S. H., Kim, W. T., Cornell-Bell, A. H., and Sontheimer, H. (1994). Astrocytes exhibit regional specificity in gap-junction coupling. *Glia* 11, 315–325. doi: 10.1002/glia.440110404

Lee, W., Reyes, R. C., Gottipati, M. K., Lewis, K., Lesort, M., Parpura, V., et al. (2013). Enhanced Ca(2+)-dependent glutamate release from astrocytes of the BACHD Huntington's disease mouse model. *Neurobiol. Dis.* 58, 192–199. doi: 10.1016/j.nbd.2013.06.002

Li, L., Ni, L., Eugenin, E. A., Heary, R. F., and Elkabes, S. (2019). Toll-like receptor 9 antagonism modulates astrocyte function and preserves proximal axons following spinal cord injury. *Brain Behav. Immun.* 80, 328–343. doi: 10.1016/j.bbi.2019.04.010

Li, X., Li, M., Tian, L., Chen, J., Liu, R., and Ning, B. (2020). Reactive astrogliosis: implications in spinal cord injury progression and therapy. *Oxid. Med. Cell. Longev.* 2020:9494352. doi: 10.1155/2020/9494352

Liddelow, S. A., Guttenplan, K. A., Clarke, L. E., Bennett, F. C., Bohlen, C. J., Schirmer, L., et al. (2017). Neurotoxic reactive astrocytes are induced by activated microglia. *Nature* 541, 481–487. doi: 10.1038/nature21029

Light, A. R., Wu, Y., Hughen, R. W., and Guthrie, P. B. (2006). Purinergic receptors activating rapid intracellular Ca increases in microglia. *Neuron Glia Biol.* 2, 125–138. doi: 10.1017/S1740925X05000323

Luisier, F., Blu, T., and Unser, M. (2011). Image denoising in mixed poisson-gaussian noise. *IEEE Trans. Image Process.* 20, 696–708. doi: 10.1109/tip.2010.2073477

Mariotti, L., Losi, G., Lia, A., Melone, M., Chiavegato, A., Gómez-Gonzalo, M., et al. (2018). Interneuron-specific signaling evokes distinctive somatostatin-mediated responses in adult cortical astrocytes. *Nat. Commun.* 9:82. doi: 10.1038/s41467-017-02642-6

Michaelis, M., Nieswandt, B., Stegner, D., Eilers, J., and Kraft, R. (2015). STIM1, STIM2, and Orai1 regulate store-operated calcium entry and purinergic activation of microglia. *Glia* 63, 652–663. doi: 10.1002/glia.22775

Mizuno, G. O., Wang, Y., Shi, G., Sun, J., Papadopoulos, S., Broussard, G. J., et al. (2018). Aberrant calcium signaling in astrocytes inhibits neuronal excitability in a human down syndrome stem cell model. *Cell Rep.* 24, 355–365. doi: 10.1016/j.celrep.2018.06.033

Möller, T. (2002). Calcium signaling in microglial cells. *Glia* 40, 184–194.

Möller, T., Nolte, C., Burger, R., Verkhratsky, A., and Kettenmann, H. (1997). Mechanisms of C5a and C3a complement fragment-induced [Ca2+]i signaling in mouse microglia. *J. Neurosci.* 17, 615–624. doi: 10.1523/JNEUROSCI.17-02-00615.1997

Müller, F. E., Cherkas, V., Stopper, G., Caudal, L. C., Stopper, L., Kirchhoff, F., et al. (2021). Elucidating regulators of astrocytic Ca2+ signaling *via* multi-threshold event detection (MTED). *Glia* 69, 2798–2811. doi: 10.1002/glia.24070

Nagai, J., Rajbhandari, A. K., Gangwani, M. R., Hachisuka, A., Coppola, G., Masmanidis, S. C., et al. (2019). Hyperactivity with disrupted attention by activation of an astrocyte synaptogenic cue. *Cell* 177, 1280–1292.e20. doi: 10.1016/j.cell.2019.03.019

Nelson, N. A., Wang, X., Cook, D., Carey, E. M., and Nimmerjahn, A. (2019). Imaging spinal cord activity in behaving animals. *Exp. Neurol.* 320:112974. doi: 10.1016/j.expneurol.2019.112974

Nett, W. J., Oloff, S. H., and McCarthy, K. D. (2002). Hippocampal astrocytes in situ exhibit calcium oscillations that occur independent of neuronal activity. *J. Neurophysiol.* 87, 528–537. doi: 10.1152/jn.00268.2001

Nishida, K., Matsumura, S., Taniguchi, W., Uta, D., Furue, H., and Ito, S. (2014). Three-dimensional distribution of sensory stimulation-evoked neuronal activity of spinal dorsal horn neurons analyzed by *in vivo* calcium imaging. *PLoS One* 9:e103321. doi: 10.1371/journal.pone.0103321

Noda, M., Nakanishi, H., Nabekura, J., and Akaike, N. (2000). AMPA-kainate subtypes of glutamate receptor in rat cerebral microglia. *J. Neurosci.* 20, 251–258. doi: 10.1523/JNEUROSCI.20-01-00251.2000

Nolte, C., Möller, T., Walter, T., and Kettenmann, H. (1996). Complement 5a controls motility of murine microglial cells *in vitro via* activation of an inhibitory G-protein and the rearrangement of the actin cytoskeleton. *Neuroscience* 73, 1091–1107. doi: 10.1016/0306-4522(96)00106-6

Okada, S., Nakamura, M., Katoh, H., Miyao, T., Shimazaki, T., Ishii, K., et al. (2006). Conditional ablation of Stat3 or Socs3 discloses a dual role for reactive astrocytes after spinal cord injury. *Nat. Med.* 12, 829–834. doi: 10.1038/nm1425

Panatier, A., and Robitaille, R. (2016). Astrocytic mGluR5 and the tripartite synapse. *Neuroscience* 323, 29–34. doi: 10.1016/j.neuroscience.2015.03.063

Parri, H. R., Gould, T. M., and Crunelli, V. (2001). Spontaneous astrocytic Ca2+ oscillations in situ drive NMDAR-mediated neuronal excitation. *Nat. Neurosci.* 4, 803–812. doi: 10.1038/90507

Paukert, M., Agarwal, A., Cha, J., Doze, V. A., Kang, J. U., and Bergles, D. E. (2014). Norepinephrine controls astroglial responsiveness to local circuit activity. *Neuron* 82, 1263–1270. doi: 10.1016/j.neuron.2014.04.038

Perea, G., Gómez, R., Mederos, S., Covelo, A., Ballesteros, J. J., Schlosser, L., et al. (2016). Activity-dependent switch of GABAergic inhibition into glutamatergic excitation in astrocyte-neuron networks. *eLife* 5:e20362. doi: 10.7554/eLife.20362

Perry, V. H., Nicoll, J. A., and Holmes, C. (2010). Microglia in neurodegenerative disease. *Nat. Rev. Neurol.* 6, 193–201.

Pologruto, T. A., Sabatini, B. L., and Svoboda, K. (2003). ScanImage: flexible software for operating laser scanning microscopes. *Biomed. Eng. Online* 2:13. doi: 10.1186/1475-925X-2-13

Poskanzer, K. E., and Yuste, R. (2016). Astrocytes regulate cortical state switching *in vivo*. *Proc. Natl. Acad. Sci. U.S.A.* 113, E2675–E2684. doi: 10.1073/pnas.1520759113

Pozner, A., Xu, B., Palumbos, S., Gee, J. M., Tvrdik, P., and Capecchi, M. R. (2015). Intracellular calcium dynamics in cortical microglia responding to focal laser injury in the PC::G5-tdT reporter mouse. *Front. Mol. Neurosci.* 8:12. doi: 10.3389/fnmol.2015.00012

Prewitt, C. M., Niesman, I. R., Kane, C. J., and Houlé, J. D. (1997). Activated macrophage/microglial cells can promote the regeneration of sensory axons into the injured spinal cord. *Exp. Neurol.* 148, 433–443. doi: 10.1006/exnr.1997.6694

Ransohoff, R. M., and El Khoury, J. (2015). Microglia in health and disease. *Cold Spring Harb. Perspect. Biol.* 8:a020560.

Rossi, D., Brambilla, L., Valori, C. F., Crugnola, A., Giaccone, G., Capobianco, R., et al. (2005). Defective tumor necrosis factor-alpha-dependent control of astrocyte glutamate release in a transgenic mouse model of Alzheimer disease. *J. Biol. Chem.* 280, 42088–42096. doi: 10.1074/jbc.M504124200

RStudio Team (2020). *RStudio: Integrated Development for R*. Boston, MA: RStudio, PBC.

Schipke, C. G., Boucsein, C., Ohlemeyer, C., Kirchhoff, F., and Kettenmann, H. (2002). Astrocyte Ca2+ waves trigger responses in microglial cells in brain slices. *FASEB J.* 16, 255–257. doi: 10.1096/fj.01-0514fje

Schweigmann, M., Caudal, L. C., Stopper, G., Scheller, A., Koch, K. P., and Kirchhoff, F. (2021). Versatile surface electrodes for combined electrophysiology and two-photon imaging of the mouse central nervous system. *Front. Cell. Neurosci.* 15:720675. doi: 10.3389/fncel.2021.720675

Sekiguchi, K. J., Shekhtmeyster, P., Merten, K., Arena, A., Cook, D., Hoffman, E., et al. (2016). Imaging large-scale cellular activity in spinal cord of freely behaving mice. *Nat. Commun.* 7:11450. doi: 10.1038/ncomms11450

Semyanov, A., Henneberger, C., and Agarwal, A. (2020). Making sense of astrocytic calcium signals - from acquisition to interpretation. *Nat. Rev. Neurosci.* 21, 551–564. doi: 10.1038/s41583-020-0361-8

Semyanov, A., and Verkhratsky, A. (2021). Astrocytic processes: from tripartite synapses to the active milieu. *Trends Neurosci.* 44, 781–792. doi: 10.1016/j.tins.2021.07.006

Shigetomi, E., Saito, K., Sano, F., and Koizumi, S. (2019). Aberrant calcium signals in reactive astrocytes: a key process in neurological disorders. *Int. J. Mol. Sci.* 20:996. doi: 10.3390/ijms20040996

Silver, J., and Miller, J. H. (2004). Regeneration beyond the glial scar. *Nat. Rev. Neurosci.* 5, 146–156.

Sofroniew, M. V., and Vinters, H. V. (2010). Astrocytes: biology and pathology. *Acta Neuropathol.* 119, 7–35. doi: 10.1007/s00401-009-0619-8

Thrane, A. S., Rangroo Thrane, V., Zeppenfeld, D., Lou, N., Xu, Q., Nagelhus, E. A., et al. (2012). General anesthesia selectively disrupts astrocyte calcium signaling in the awake mouse cortex. *Proc. Natl. Acad. Sci. U.S.A.* 109, 18974–18979. doi: 10.1073/pnas.1209448109

Toescu, E. C., Möller, T., Kettenmann, H., and Verkhratsky, A. (1998). Long-term activation of capacitative Ca2+ entry in mouse microglial cells. *Neuroscience* 86, 925–935. doi: 10.1016/s0306-4522(98)00123-7

Umpierre, A. D., Bystrom, L. L., Ying, Y., Liu, Y. U., Worrell, G., and Wu, L. J. (2020). Microglial calcium signaling is attuned to neuronal activity in awake mice. *eLife* 9:e56502. doi: 10.7554/eLife.56502

Verkhratsky, A. (2006). Glial calcium signaling in physiology and pathophysiology. *Acta Pharmacol. Sin.* 27, 773–780. doi: 10.1111/j.1745-7254.2006.00396.x

Verkhratsky, A., and Kettenmann, H. (1996). Calcium signalling in glial cells. *Trends Neurosci.* 19, 346–352.

Verkhratsky, A., Orkand, R. K., and Kettenmann, H. (1998). Glial calcium: homeostasis and signaling function. *Physiol. Rev.* 78, 99–141. doi: 10.1152/physrev.1998.78.1.99

Visentin, S., Renzi, M., Frank, C., Greco, A., and Levi, G. (1999). Two different ionotropic receptors are activated by ATP in rat microglia. *J. Physiol.* 519(Pt 3), 723–736. doi: 10.1111/j.1469-7793.1999.0723n.x

Wake, H., Lee, P. R., and Fields, R. D. (2011). Control of local protein synthesis and initial events in myelination by action potentials. *Science* 333, 1647–1651. doi: 10.1126/science.1206998

Wu, Y. W., Tang, X., Arizono, M., Bannai, H., Shih, P. Y., Dembitskaya, Y., et al. (2014). Spatiotemporal calcium dynamics in single astrocytes and its modulation by neuronal activity. *Cell Calcium* 55, 119–129. doi: 10.1016/j.ceca.2013.12.006

Yona, S., Kim, K. W., Wolf, Y., Mildner, A., Varol, D., Breker, M., et al. (2013). Fate mapping reveals origins and dynamics of monocytes and tissue macrophages under homeostasis. *Immunity* 38, 79–91. doi: 10.1016/j.immuni.2012.12.001

Ziskin, J. L., Nishiyama, A., Rubio, M., Fukaya, M., and Bergles, D. E. (2007). Vesicular release of glutamate from unmyelinated axons in white matter. *Nat. Neurosci.* 10, 321–330.

Conflict of Interest: The authors declare that the research was conducted in the absence of any commercial or financial relationships that could be construed as a potential conflict of interest.

Publisher's Note: All claims expressed in this article are solely those of the authors and do not necessarily represent those of their affiliated organizations, or those of the publisher, the editors and the reviewers. Any product that may be evaluated in this article, or claim that may be made by its manufacturer, is not guaranteed or endorsed by the publisher.

10 REFERENCES

Akerboom J, Rivera JD, Guilbe MM, Malavé EC, Hernandez HH, Tian L, Hires SA, Marvin JS, Looger LL, Schreiter ER (2009) Crystal structures of the GCaMP calcium sensor reveal the mechanism of fluorescence signal change and aid rational design. J Biol Chem 284:6455-6464.

Arai K, Lo EH (2009) An oligovascular niche: cerebral endothelial cells promote the survival and proliferation of oligodendrocyte precursor cells. J Neurosci 29:4351-4355.

Araque A, Navarrete M (2010) Glial cells in neuronal network function. Philos Trans R Soc Lond B Biol Sci 365:2375-2381.

Bagur R, Hajnóczky G (2017) Intracellular Ca. Mol Cell 66:780-788.

Bai X, Kirchhoff F, Scheller A (2021) Oligodendroglial GABAergic Signaling: More Than Inhibition! Neurosci Bull 37:1039-1050.

Baraban M, Koudelka S, Lyons DA (2018) Ca. Nat Neurosci 21:19-23.

Bayraktar OA, Fuentealba LC, Alvarez-Buylla A, Rowitch DH (2014) Astrocyte development and heterogeneity. Cold Spring Harb Perspect Biol 7:a020362.

Bazargani N, Attwell D (2016) Astrocyte calcium signaling: the third wave. Nat Neurosci 19:182-189.

Beal MF (1992) Mechanisms of excitotoxicity in neurologic diseases. FASEB J 6:3338-3344.

Bechler ME, Byrne L, Ffrench-Constant C (2015) CNS Myelin Sheath Lengths Are an Intrinsic Property of Oligodendrocytes. Curr Biol 25:2411-2416.

Beecham AH et al. (2013) Analysis of immune-related loci identifies 48 new susceptibility variants for multiple sclerosis. Nat Genet 45:1353-1360.

Berger T, Walz W, Schnitzer J, Kettenmann H (1992) GABA- and glutamate-activated currents in glial cells of the mouse corpus callosum slice. J Neurosci Res 31:21-27.

Berghoff SA, Düking T, Spieth L, Winchenbach J, Stumpf SK, Gerndt N, Kusch K, Ruhwedel T, Möbius W, Saher G (2017) Blood-brain barrier hyperpermeability precedes demyelination in the cuprizone model. Acta Neuropathol Commun 5:94.

Bergles DE, Richardson WD (2015) Oligodendrocyte Development and Plasticity. Cold Spring Harb Perspect Biol 8.

Bergles DE, Richardson WD (2016) Oligodendrocyte Development and Plasticity. Cold Spring Harb Perspect Biol 8:a020453.

Bergles DE, Roberts JD, Somogyi P, Jahr CE (2000) Glutamatergic synapses on oligodendrocyte precursor cells in the hippocampus. Nature 405:187-191.

Berridge MJ (2016) The Inositol Trisphosphate/Calcium Signaling Pathway in Health and Disease. Physiol Rev 96:1261-1296.

Berry K, Wang J, Lu QR (2020) Epigenetic regulation of oligodendrocyte myelination in developmental disorders and neurodegenerative diseases. F1000Res 9.

Blakemore WF (1974) Pattern of remyelination in the CNS. Nature 249:577-578.

Boshans LL, Sherafat A, Nishiyama A (2020) The effects of developmental and current niches on oligodendrocyte precursor dynamics and fate. Neurosci Lett 715:134593.

Bradl M, Lassmann H (2010) Oligodendrocytes: biology and pathology. Acta Neuropathol 119:37-53.

Browne P, Chandraratna D, Angood C, Tremlett H, Baker C, Taylor BV, Thompson AJ (2014) Atlas of Multiple Sclerosis 2013: A growing global problem with widespread inequity. Neurology 83:1022-1024.

Bénardais K, Kotsiari A, Skuljec J, Koutsoudaki PN, Gudi V, Singh V, Vulinović F, Skripuletz T, Stangel M (2013) Cuprizone [bis(cyclohexylidenehydrazide)] is selectively toxic for mature oligodendrocytes. Neurotox Res 24:244-250.

Calver AR, Medhurst AD, Robbins MJ, Charles KJ, Evans ML, Harrison DC, Stammers M, Hughes SA, Hervieu G, Couve A, Moss SJ, Middlemiss DN, Pangalos MN (2000) The expression of GABA(B1) and GABA(B2) receptor subunits in the cNS differs from that in peripheral tissues. Neuroscience 100:155-170.

Carlton WW (1966) Response of mice to the chelating agents sodium diethyldithiocarbamate, alpha-benzoinoxime, and biscyclohexanone oxaldihydrazone. Toxicol Appl Pharmacol 8:512-521.

Carozzi VA, Canta A, Oggioni N, Ceresa C, Marmiroli P, Konvalinka J, Zoia C, Bossi M, Ferrarese C, Tredici G, Cavaletti G (2008) Expression and distribution of 'high affinity' glutamate transporters GLT1, GLAST, EAAC1 and of GCPII in the rat peripheral nervous system. J Anat 213:539-546.

Cartarozzi LP, Rieder P, Bai X, Scheller A, Oliveira ALR, Kirchhoff F (2018) In vivo two-photon imaging of motoneurons and adjacent glia in the ventral spinal cord. J Neurosci Methods 299:8-15.
Casaccia-Bonnefil P, Tikoo R, Kiyokawa H, Friedrich V, Chao MV, Koff A (1997) Oligodendrocyte precursor differentiation is perturbed in the absence of the cyclin-dependent kinase inhibitor p27Kip1. Genes Dev 11:2335-2346.
Cerella C, Diederich M, Ghibelli L (2010) The dual role of calcium as messenger and stressor in cell damage, death, and survival. Int J Cell Biol 2010:546163.
Chang A, Tourtellotte WW, Rudick R, Trapp BD (2002) Premyelinating oligodendrocytes in chronic lesions of multiple sclerosis. N Engl J Med 346:165-173.
Charles AC (1994) Glia-neuron intercellular calcium signaling. Dev Neurosci 16:196-206.
Charles AC, Merrill JE, Dirksen ER, Sanderson MJ (1991) Intercellular signaling in glial cells: calcium waves and oscillations in response to mechanical stimulation and glutamate. Neuron 6:983-992.
Cirillo G, De Luca D, Papa M (2012) Calcium imaging of living astrocytes in the mouse spinal cord following sensory stimulation. Neural Plast 2012:425818.
Clapham DE (2007) Calcium signaling. Cell 131:1047-1058.
Clayton BLL, Tesar PJ (2021) Oligodendrocyte progenitor cell fate and function in development and disease. Curr Opin Cell Biol 73:35-40.
Cupido A, Catalin B, Steffens H, Kirchhoff F (2014) Surgical procedures to study microglial motility in the brain and in the spinal cord by in vivo two-photon laser-scanning microcopy. In: Confocal and Multiphoton Laser-Scanning Microscopy of Neuronal Tissue: Applications and Quantitative Image Analysis (Bakota L, Brandt R, eds), pp 37-50: Springer.
Dawson MR, Polito A, Levine JM, Reynolds R (2003) NG2-expressing glial progenitor cells: an abundant and widespread population of cycling cells in the adult rat CNS. Mol Cell Neurosci 24:476-488.
De Biase LM, Kang SH, Baxi EG, Fukaya M, Pucak ML, Mishina M, Calabresi PA, Bergles DE (2011) NMDA receptor signaling in oligodendrocyte progenitors is not required for oligodendrogenesis and myelination. J Neurosci 31:12650-12662.
Deitmer JW, Verkhratsky AJ, Lohr C (1998) Calcium signalling in glial cells. Cell Calcium 24:405-416.
Delumeau JC, Marin P, Cordier J, Glowinski J, Premont J (1991) Synergistic effects in the alpha 1- and beta 1-adrenergic regulations of intracellular calcium levels in striatal astrocytes. Cell Mol Neurobiol 11:263-276.
Di Benedetto G, Burgaletto C, Bellanca CM, Munafò A, Bernardini R, Cantarella G (2022) Role of Microglia and Astrocytes in Alzheimer's Disease: From Neuroinflammation to Ca. Cells 11.
Dibaj P, Steffens H, Nadrigny F, Neusch C, Kirchhoff F, Schomburg ED (2010) Long-lasting post-mortem activity of spinal microglia in situ in mice. J Neurosci Res 88:2431-2440.
Dimou L, Gallo V (2015) NG2-glia and their functions in the central nervous system. Glia 63:1429-1451.
Dimou L, Simons M (2017) Diversity of oligodendrocytes and their progenitors. Curr Opin Neurobiol 47:73-79.
Dobson R, Giovannoni G (2019) Multiple sclerosis - a review. Eur J Neurol 26:27-40.
Duncan ID, Radcliff AB (2016) Inherited and acquired disorders of myelin: The underlying myelin pathology. Exp Neurol 283:452-475.
Duncan ID, Radcliff AB, Heidari M, Kidd G, August BK, Wierenga LA (2018) The adult oligodendrocyte can participate in remyelination. Proc Natl Acad Sci U S A 115:E11807-E11816.
Eichhoff G, Brawek B, Garaschuk O (2011) Microglial calcium signal acts as a rapid sensor of single neuron damage in vivo. Biochim Biophys Acta 1813:1014-1024.
Emery B (2010) Regulation of oligodendrocyte differentiation and myelination. Science 330:779-782.
Emery B, Lu QR (2015) Transcriptional and Epigenetic Regulation of Oligodendrocyte Development and Myelination in the Central Nervous System. Cold Spring Harb Perspect Biol 7:a020461.
Enders M, Heider T, Ludwig A, Kuerten S (2020) Strategies for Neuroprotection in Multiple Sclerosis and the Role of Calcium. Int J Mol Sci 21.
Ermak G, Davies KJ (2002) Calcium and oxidative stress: from cell signaling to cell death. Mol Immunol 38:713-721.
Fancy SP, Zhao C, Franklin RJ (2004) Increased expression of Nkx2.2 and Olig2 identifies reactive oligodendrocyte progenitor cells responding to demyelination in the adult CNS. Mol Cell Neurosci 27:247-254.

Fang LP, Liu Q, Meyer E, Welle A, Huang W, Scheller A, Kirchhoff F, Bai X (2022a) A subset of OPCs do not express Olig2 during development which can be increased in the adult by brain injuries and complex motor learning. Glia.
Fang LP, Zhao N, Caudal LC, Chang HF, Zhao R, Lin CH, Hainz N, Meier C, Bettler B, Huang W, Scheller A, Kirchhoff F, Bai X (2022b) Impaired bidirectional communication between interneurons and oligodendrocyte precursor cells affects social cognitive behavior. Nat Commun 13:1394.
Feil S, Valtcheva N, Feil R (2009) Inducible Cre mice. Methods Mol Biol 530:343-363.
Fenrich KK, Weber P, Hocine M, Zalc M, Rougon G, Debarbieux F (2012) Long-term in vivo imaging of normal and pathological mouse spinal cord with subcellular resolution using implanted glass windows. J Physiol 590:3665-3675.
Finkbeiner SM (1993) Glial calcium. Glia 9:83-104.
Fischbach F, Nedelcu J, Leopold P, Zhan J, Clarner T, Nellessen L, Beißel C, van Heuvel Y, Goswami A, Weis J, Denecke B, Schmitz C, Hochstrasser T, Nyamoya S, Victor M, Beyer C, Kipp M (2019) Cuprizone-induced graded oligodendrocyte vulnerability is regulated by the transcription factor DNA damage-inducible transcript 3. Glia 67:263-276.
Foerster S, Hill MFE, Franklin RJM (2019) Diversity in the oligodendrocyte lineage: Plasticity or heterogeneity? Glia 67:1797-1805.
Fogarty M, Richardson WD, Kessaris N (2005) A subset of oligodendrocytes generated from radial glia in the dorsal spinal cord. Development 132:1951-1959.
Franco L, Bodrato N, Moreschi I, Usai C, Bruzzone S, Scarf ì S, Zocchi E, De Flora A (2006) Cyclic ADP-ribose is a second messenger in the lipopolysaccharide-stimulated activation of murine N9 microglial cell line. J Neurochem 99:165-176.
Franklin RJM, Ffrench-Constant C (2017) Regenerating CNS myelin - from mechanisms to experimental medicines. Nat Rev Neurosci 18:753-769.
Fujii Y, Maekawa S, Morita M (2017) Astrocyte calcium waves propagate proximally by gap junction and distally by extracellular diffusion of ATP released from volume-regulated anion channels. Sci Rep 7:13115.
Gallo V, Mangin JM, Kukley M, Dietrich D (2008) Synapses on NG2-expressing progenitors in the brain: multiple functions? J Physiol 586:3767-3781.
Galloway DA, Moore CS (2016) miRNAs As Emerging Regulators of Oligodendrocyte Development and Differentiation. Front Cell Dev Biol 4:59.
Gilbert P, Kettenmann H, Schachner M (1984) gamma-Aminobutyric acid directly depolarizes cultured oligodendrocytes. J Neurosci 4:561-569.
Guerra-Gomes S, Sousa N, Pinto L, Oliveira JF (2017) Functional Roles of Astrocyte Calcium Elevations: From Synapses to Behavior. Front Cell Neurosci 11:427.
Guerrero BL, Sicotte NL (2020) Microglia in Multiple Sclerosis: Friend or Foe? Front Immunol 11:374.
Gómez-Gonzalo M, Navarrete M, Perea G, Covelo A, Martín-Fernández M, Shigemoto R, Luján R, Araque A (2015) Endocannabinoids Induce Lateral Long-Term Potentiation of Transmitter Release by Stimulation of Gliotransmission. Cereb Cortex 25:3699-3712.
Haller C, Casanova E, Müller M, Vacher CM, Vigot R, Doll T, Barbieri S, Gassmann M, Bettler B (2004) Floxed allele for conditional inactivation of the GABAB(1) gene. Genesis 40:125-130.
Hamilton N, Vayro S, Wigley R, Butt AM (2010) Axons and astrocytes release ATP and glutamate to evoke calcium signals in NG2-glia. Glia 58:66-79.
Hammond TR, Gadea A, Dupree J, Kerninon C, Nait-Oumesmar B, Aguirre A, Gallo V (2014) Astrocyte-derived endothelin-1 inhibits remyelination through notch activation. Neuron 81:588-602.
Handel AE, Williamson AJ, Disanto G, Dobson R, Giovannoni G, Ramagopalan SV (2011) Smoking and multiple sclerosis: an updated meta-analysis. PLoS One 6:e16149.
Harirchian MH, Fatehi F, Sarraf P, Honarvar NM, Bitarafan S (2018) Worldwide prevalence of familial multiple sclerosis: A systematic review and meta-analysis. Mult Scler Relat Disord 20:43-47.
Healy LM, Stratton JA, Kuhlmann T, Antel J (2022) The role of glial cells in multiple sclerosis disease progression. Nat Rev Neurol 18:237-248.
Herder V, Hansmann F, Stangel M, Skripuletz T, Baumgärtner W, Beineke A (2011) Lack of cuprizone-induced demyelination in the murine spinal cord despite oligodendroglial alterations substantiates the concept of site-specific susceptibilities of the central nervous system. Neuropathol Appl Neurobiol 37:676-684.
Hesp ZC, Goldstein EZ, Goldstein EA, Miranda CJ, Kaspar BK, McTigue DM (2015) Chronic oligodendrogenesis and remyelination after spinal cord injury in mice and rats. J Neurosci 35:1274-1290.

Hiremath MM, Saito Y, Knapp GW, Ting JP, Suzuki K, Matsushima GK (1998) Microglial/macrophage accumulation during cuprizone-induced demyelination in C57BL/6 mice. J Neuroimmunol 92:38-49.
Hirrlinger PG, Scheller A, Braun C, Hirrlinger J, Kirchhoff F (2006) Temporal control of gene recombination in astrocytes by transgenic expression of the tamoxifen-inducible DNA recombinase variant CreERT2. Glia 54:11-20.
Horvat A, Zorec R, Vardjan N (2016) Adrenergic stimulation of single rat astrocytes results in distinct temporal changes in intracellular Ca(2+) and cAMP-dependent PKA responses. Cell Calcium 59:156-163.
Huang W, Bai X, Meyer E, Scheller A (2020) Acute brain injuries trigger microglia as an additional source of the proteoglycan NG2. Acta Neuropathol Commun 8:146.
Huang W, Bai X, Stopper L, Catalin B, Cartarozzi LP, Scheller A, Kirchhoff F (2018) During Development NG2 Glial Cells of the Spinal Cord are Restricted to the Oligodendrocyte Lineage, but Generate Astrocytes upon Acute Injury. Neuroscience 385:154-165.
Huang W, Zhao N, Bai X, Karram K, Trotter J, Goebbels S, Scheller A, Kirchhoff F (2014) Novel NG2-CreERT2 knock-in mice demonstrate heterogeneous differentiation potential of NG2 glia during development. Glia 62:896-913.
Jahn HM, Kasakow CV, Helfer A, Michely J, Verkhratsky A, Maurer HH, Scheller A, Kirchhoff F (2018) Refined protocols of tamoxifen injection for inducible DNA recombination in mouse astroglia. Sci Rep 8:5913.
Juurlink BH, Thorburne SK, Hertz L (1998) Peroxide-scavenging deficit underlies oligodendrocyte susceptibility to oxidative stress. Glia 22:371-378.
Jäkel S, Agirre E, Mendanha Falcão A, van Bruggen D, Lee KW, Knuesel I, Malhotra D, Ffrench-Constant C, Williams A, Castelo-Branco G (2019) Altered human oligodendrocyte heterogeneity in multiple sclerosis. Nature 566:543-547.
Karussis D (2014) The diagnosis of multiple sclerosis and the various related demyelinating syndromes: a critical review. J Autoimmun 48-49:134-142.
Kipp M, Clarner T, Dang J, Copray S, Beyer C (2009) The cuprizone animal model: new insights into an old story. Acta Neuropathol 118:723-736.
Koch-Henriksen N, Sørensen PS (2010) The changing demographic pattern of multiple sclerosis epidemiology. Lancet Neurol 9:520-532.
Krasnow AM, Ford MC, Valdivia LE, Wilson SW, Attwell D (2018) Regulation of developing myelin sheath elongation by oligodendrocyte calcium transients in vivo. Nat Neurosci 21:24-28.
Krauspe BM, Dreher W, Beyer C, Baumgartner W, Denecke B, Janssen K, Langhans CD, Clarner T, Kipp M (2015) Short-term cuprizone feeding verifies N-acetylaspartate quantification as a marker of neurodegeneration. J Mol Neurosci 55:733-748.
Kuhlmann T, Ludwin S, Prat A, Antel J, Brück W, Lassmann H (2017) An updated histological classification system for multiple sclerosis lesions. Acta Neuropathol 133:13-24.
Kuhlmann T, Miron V, Cui Q, Cuo Q, Wegner C, Antel J, Brück W (2008) Differentiation block of oligodendroglial progenitor cells as a cause for remyelination failure in chronic multiple sclerosis. Brain 131:1749-1758.
Kuhn S, Gritti L, Crooks D, Dombrowski Y (2019) Oligodendrocytes in Development, Myelin Generation and Beyond. Cells 8.
Kukley M, Capetillo-Zarate E, Dietrich D (2007) Vesicular glutamate release from axons in white matter. Nat Neurosci 10:311-320.
Kurtzke JF (2013) Epidemiology in multiple sclerosis: a pilgrim's progress. Brain 136:2904-2917.
Káradóttir R, Attwell D (2007) Neurotransmitter receptors in the life and death of oligodendrocytes. Neuroscience 145:1426-1438.
Lassmann H (2018) Multiple Sclerosis Pathology. Cold Spring Harb Perspect Med 8.
Lassmann H (2019) The changing concepts in the neuropathology of acquired demyelinating central nervous system disorders. Curr Opin Neurol 32:313-319.
Levine JM, Reynolds R (1999) Activation and proliferation of endogenous oligodendrocyte precursor cells during ethidium bromide-induced demyelination. Exp Neurol 160:333-347.
Lia A, Henriques VJ, Zonta M, Chiavegato A, Carmignoto G, Gómez-Gonzalo M, Losi G (2021) Calcium Signals in Astrocyte Microdomains, a Decade of Great Advances. Front Cell Neurosci 15:673433.
Lim D, Semyanov A, Genazzani A, Verkhratsky A (2021) Calcium signaling in neuroglia. In: International Review of Cell and Molecular Biology

Inter-Organellar Ca2+ Signaling in Health and Disease - Part A (Galluzzi SMal, ed), pp 1-53: Zoe Kruze.

Lin SC, Bergles DE (2004) Synaptic signaling between GABAergic interneurons and oligodendrocyte precursor cells in the hippocampus. Nat Neurosci 7:24-32.
Love S (2006) Demyelinating diseases. J Clin Pathol 59:1151-1159.
Lubetzki C, Stankoff B (2014) Demyelination in multiple sclerosis. Handb Clin Neurol 122:89-99.
Luisier F, Blu T, Unser M (2011) Image denoising in mixed Poisson-Gaussian noise. IEEE Trans Image Process 20:696-708.
Luyt K, Slade TP, Dorward JJ, Durant CF, Wu Y, Shigemoto R, Mundell SJ, Váradi A, Molnár E (2007) Developing oligodendrocytes express functional GABA(B) receptors that stimulate cell proliferation and migration. J Neurochem 100:822-840.
Ma Z, Wei L, Du X, Hou S, Chen F, Jiao Q, Liu A, Liu S, Wang J, Shen H (2021) Two-photon calcium imaging of neuronal and astrocytic responses: the influence of electrical stimulus parameters and calcium signaling mechanisms. J Neural Eng 18.
Mariotti L, Losi G, Sessolo M, Marcon I, Carmignoto G (2016) The inhibitory neurotransmitter GABA evokes long-lasting Ca(2+) oscillations in cortical astrocytes. Glia 64:363-373.
Marisca R, Hoche T, Agirre E, Hoodless LJ, Barkey W, Auer F, Castelo-Branco G, Czopka T (2020) Functionally distinct subgroups of oligodendrocyte precursor cells integrate neural activity and execute myelin formation. Nat Neurosci 23:363-374.
Mattson MP (2007) Calcium and neurodegeneration. Aging Cell 6:337-350.
Matute C, Sánchez-Gómez MV, Martínez-Millán L, Miledi R (1997) Glutamate receptor-mediated toxicity in optic nerve oligodendrocytes. Proc Natl Acad Sci U S A 94:8830-8835.
Matute C, Torre I, Pérez-Cerdá F, Pérez-Samartín A, Alberdi E, Etxebarria E, Arranz AM, Ravid R, Rodríguez-Antigüedad A, Sánchez-Gómez M, Domercq M (2007) P2X(7) receptor blockade prevents ATP excitotoxicity in oligodendrocytes and ameliorates experimental autoimmune encephalomyelitis. J Neurosci 27:9525-9533.
McKenzie IA, Ohayon D, Li H, de Faria JP, Emery B, Tohyama K, Richardson WD (2014) Motor skill learning requires active central myelination. Science 346:318-322.
McMurran CE, Zhao C, Franklin RJM (2019) Toxin-Based Models to Investigate Demyelination and Remyelination. Methods Mol Biol 1936:377-396.
McTigue DM, Tripathi RB (2008) The life, death, and replacement of oligodendrocytes in the adult CNS. J Neurochem 107:1-19.
Meyer E, Rieder P, Gobbo D, Candido G, Scheller A, de Oliveira RMW, Kirchhoff F (2022) Cannabidiol Exerts a Neuroprotective and Glia-Balancing Effect in the Subacute Phase of Stroke. International Journal of Molecular Sciences 23:12886.
Miller RH (2018) Calcium control of myelin sheath growth. Nat Neurosci 21:2-3.
Miron VE, Boyd A, Zhao JW, Yuen TJ, Ruckh JM, Shadrach JL, van Wijngaarden P, Wagers AJ, Williams A, Franklin RJ, ffrench-Constant C (2013) M2 microglia and macrophages drive oligodendrocyte differentiation during CNS remyelination. Nat Neurosci 16:1211-1218.
Mizoguchi Y, Monji A (2017) Microglial Intracellular Ca. Front Cell Neurosci 11:69.
Moore S, Meschkat M, Ruhwedel T, Trevisiol A, Tzvetanova ID, Battefeld A, Kusch K, Kole MHP, Strenzke N, Möbius W, de Hoz L, Nave KA (2020) A role of oligodendrocytes in information processing. Nat Commun 11:5497.
Nakai J, Ohkura M, Imoto K (2001) A high signal-to-noise Ca(2+) probe composed of a single green fluorescent protein. Nat Biotechnol 19:137-141.
Napier MD, Poole C, Satten GA, Ashley-Koch A, Marrie RA, Williamson DM (2016) Heavy metals, organic solvents, and multiple sclerosis: An exploratory look at gene-environment interactions. Arch Environ Occup Health 71:26-34.
Nuriya M, Takeuchi M, Yasui M (2017) Background norepinephrine primes astrocytic calcium responses to subsequent norepinephrine stimuli in the cerebral cortex. Biochem Biophys Res Commun 483:732-738.
Orton SM, Herrera BM, Yee IM, Valdar W, Ramagopalan SV, Sadovnick AD, Ebers GC, Group CCS (2006) Sex ratio of multiple sclerosis in Canada: a longitudinal study. Lancet Neurol 5:932-936.
Paez PM, Lyons DA (2020) Calcium Signaling in the Oligodendrocyte Lineage: Regulators and Consequences. Annu Rev Neurosci 43:163-186.
Palacios N, Alonso A, Brønnum-Hansen H, Ascherio A (2011) Smoking and increased risk of multiple sclerosis: parallel trends in the sex ratio reinforce the evidence. Ann Epidemiol 21:536-542.
Papouin T, Dunphy JM, Tolman M, Dineley KT, Haydon PG (2017) Septal Cholinergic Neuromodulation Tunes the Astrocyte-Dependent Gating of Hippocampal NMDA Receptors to Wakefulness. Neuron 94:840-854.e847.
Parolisi R, Boda E (2018) NG2 Glia: Novel Roles beyond Re-/Myelination. Neuroglia 1:151-175.

Paukert M, Agarwal A, Cha J, Doze VA, Kang JU, Bergles DE (2014) Norepinephrine controls astroglial responsiveness to local circuit activity. Neuron 82:1263-1270.
Pchitskaya E, Popugaeva E, Bezprozvanny I (2018) Calcium signaling and molecular mechanisms underlying neurodegenerative diseases. Cell Calcium 70:87-94.
Perea G, Araque A (2007) Astrocytes potentiate transmitter release at single hippocampal synapses. Science 317:1083-1086.
Perea G, Sur M, Araque A (2014) Neuron-glia networks: integral gear of brain function. Front Cell Neurosci 8:378.
Perea G, Gómez R, Mederos S, Covelo A, Ballesteros JJ, Schlosser L, Hernández-Vivanco A, Martín-Fernández M, Quintana R, Rayan A, Díez A, Fuenzalida M, Agarwal A, Bergles DE, Bettler B, Manahan-Vaughan D, Martín ED, Kirchhoff F, Araque A (2016) Activity-dependent switch of GABAergic inhibition into glutamatergic excitation in astrocyte-neuron networks. Elife 5.
Pitt D, Werner P, Raine CS (2000) Glutamate excitotoxicity in a model of multiple sclerosis. Nat Med 6:67-70.
Pologruto TA, Sabatini BL, Svoboda K (2003) ScanImage: flexible software for operating laser scanning microscopes. Biomed Eng Online 2:13.
Pozner A, Xu B, Palumbos S, Gee JM, Tvrdik P, Capecchi MR (2015) Intracellular calcium dynamics in cortical microglia responding to focal laser injury in the PC::G5-tdT reporter mouse. Front Mol Neurosci 8:12.
Praet J, Guglielmetti C, Berneman Z, Van der Linden A, Ponsaerts P (2014) Cellular and molecular neuropathology of the cuprizone mouse model: clinical relevance for multiple sclerosis. Neurosci Biobehav Rev 47:485-505.
Raasakka A, Jones NC, Hoffmann SV, Kursula P (2019) Ionic strength and calcium regulate membrane interactions of myelin basic protein and the cytoplasmic domain of myelin protein zero. Biochem Biophys Res Commun 511:7-12.
Ramagopalan SV, Dobson R, Meier UC, Giovannoni G (2010) Multiple sclerosis: risk factors, prodromes, and potential causal pathways. Lancet Neurol 9:727-739.
Rawji KS, Gonzalez Martinez GA, Sharma A, Franklin RJM (2020) The Role of Astrocytes in Remyelination. Trends Neurosci 43:596-607.
Richardson WD, Kessaris N, Pringle N (2006) Oligodendrocyte wars. Nat Rev Neurosci 7:11-18.
Rieder P, Gobbo D, Stopper G, Welle A, Damo E, Kirchhoff F, Scheller A (2022) Astrocytes and Microglia Exhibit Cell-Specific Ca. Front Mol Neurosci 15:840948.
Salmaso N, Jablonska B, Scafidi J, Vaccarino FM, Gallo V (2014) Neurobiology of premature brain injury. Nat Neurosci 17:341-346.
Sampaio-Baptista C, Johansen-Berg H (2017) White Matter Plasticity in the Adult Brain. Neuron 96:1239-1251.
Santiago González DA, Cheli VT, Zamora NN, Lama TN, Spreuer V, Murphy GG, Paez PM (2017) Conditional Deletion of the L-Type Calcium Channel Cav1.2 in NG2-Positive Cells Impairs Remyelination in Mice. J Neurosci 37:10038-10051.
Sattler R, Tymianski M (2000) Molecular mechanisms of calcium-dependent excitotoxicity. J Mol Med (Berl) 78:3-13.
Saxena A, Bauer J, Scheikl T, Zappulla J, Audebert M, Desbois S, Waisman A, Lassmann H, Liblau RS, Mars LT (2008) Cutting edge: Multiple sclerosis-like lesions induced by effector CD8 T cells recognizing a sequestered antigen on oligodendrocytes. J Immunol 181:1617-1621.
Schweigmann M, Caudal LC, Stopper G, Scheller A, Koch KP, Kirchhoff F (2021) Versatile Surface Electrodes for Combined Electrophysiology and Two-Photon Imaging of the Mouse Central Nervous System. Frontiers in Cellular Neuroscience 15.
Seidman RA, Khattab H, Polanco JJ, Broome JE, Sim FJ (2022) Oscillatory calcium release and sustained store-operated oscillatory calcium signaling prevents differentiation of human oligodendrocyte progenitor cells. Sci Rep 12:6160.
Serrano A, Haddjeri N, Lacaille JC, Robitaille R (2006) GABAergic network activation of glial cells underlies hippocampal heterosynaptic depression. J Neurosci 26:5370-5382.
Serrano-Regal MP, Bayón-Cordero L, Chara Ventura JC, Ochoa-Bueno BI, Tepavcevic V, Matute C, Sánchez-Gómez MV (2022) GABA. Glia 70:2426-2440.
Serrano-Regal MP, Luengas-Escuza I, Bayón-Cordero L, Ibarra-Aizpurua N, Alberdi E, Pérez-Samartín A, Matute C, Sánchez-Gómez MV (2019) Oligodendrocyte Differentiation and Myelination Is Potentiated via GABA. Neuroscience.
Shekhtmeyster P, Duarte D, Carey EM, Ngo A, Gao G, Olmstead JA, Nelson NA, Nimmerjahn A (2023) Trans-segmental imaging in the spinal cord of behaving mice. Nat Biotechnol.

Sherafat A, Pfeiffer F, Nishiyama A (2021) Shaping of Regional Differences in Oligodendrocyte Dynamics by Regional Heterogeneity of the Pericellular Microenvironment. Front Cell Neurosci 15:721376.
Sherwood MW, Arizono M, Hisatsune C, Bannai H, Ebisui E, Sherwood JL, Panatier A, Oliet SH, Mikoshiba K (2017) Astrocytic IP. Glia 65:502-513.
Sintzel MB, Rametta M, Reder AT (2018) Vitamin D and Multiple Sclerosis: A Comprehensive Review. Neurol Ther 7:59-85.
Stadelmann C, Timmler S, Barrantes-Freer A, Simons M (2019) Myelin in the Central Nervous System: Structure, Function, and Pathology. Physiol Rev 99:1381-1431.
Steelman AJ, Thompson JP, Li J (2012) Demyelination and remyelination in anatomically distinct regions of the corpus callosum following cuprizone intoxication. Neurosci Res 72:32-42.
Steinhäuser C, Jabs R, Kettenmann H (1994) Properties of GABA and glutamate responses in identified glial cells of the mouse hippocampal slice. Hippocampus 4:19-35.
Stopper G, Caudal LC, Rieder P, Gobbo D, Felix L, Everaerts K, Bai X, Stopper L, Rose CR, Scheller A, Kirchhoff F (2022) Novel algorithms for improved detection and analysis of fluorescent signal fluctuations. bioRxiv:2022.2008.2003.502593.
Sun W, Matthews EA, Nicolas V, Schoch S, Dietrich D (2016) NG2 glial cells integrate synaptic input in global and dendritic calcium signals. Elife 5.
Szoke K, Härtel K, Grass D, Hirrlinger PG, Hirrlinger J, Hülsmann S (2006) Glycine transporter 1 expression in the ventral respiratory group is restricted to protoplasmic astrocytes. Brain Res 1119:182-189.
Szydlowska K, Tymianski M (2010) Calcium, ischemia and excitotoxicity. Cell Calcium 47:122-129.
Taheri M, Handy G, Borisyuk A, White JA (2017) Diversity of Evoked Astrocyte Ca. Front Syst Neurosci 11:79.
Tanaka Y, Tozuka Y, Takata T, Shimazu N, Matsumura N, Ohta A, Hisatsune T (2009) Excitatory GABAergic activation of cortical dividing glial cells. Cereb Cortex 19:2181-2195.
Thrane AS, Thrane VR, Zeppenfeld D, Lou N, Xu Q, Nagelhus EA, Nedergaard M (2012) General anesthesia selectively disrupts astrocyte calcium signaling in the awake mouse cortex. Proceedings of the National Academy of Sciences of the United States of America 109:18974-18979.
Toomey LM, Papini M, Lins B, Wright AJ, Warnock A, McGonigle T, Hellewell SC, Bartlett CA, Anyaegbu C, Fitzgerald M (2021) Cuprizone feed formulation influences the extent of demyelinating disease pathology. Sci Rep 11:22594.
Traka M, Podojil JR, McCarthy DP, Miller SD, Popko B (2016) Oligodendrocyte death results in immune-mediated CNS demyelination. Nat Neurosci 19:65-74.
Umpierre AD, Bystrom LL, Ying Y, Liu YU, Worrell G, Wu LJ (2020) Microglial calcium signaling is attuned to neuronal activity in awake mice. Elife 9.
Verkhratsky A, Kettenmann H (1996) Calcium signalling in glial cells. Trends Neurosci 19:346-352.
Verkhratsky A, Parpura V (2014) Calcium signalling and calcium channels: evolution and general principles. Eur J Pharmacol 739:1-3.
Vernadakis A (1996) Glia-neuron intercommunications and synaptic plasticity. Prog Neurobiol 49:185-214.
Von Blankenfeld G, Trotter J, Kettenmann H (1991) Expression and Developmental Regulation of a GABAA Receptor in Cultured Murine Cells of the Oligodendrocyte Lineage. Eur J Neurosci 3:310-316.
Weil MT, Möbius W, Winkler A, Ruhwedel T, Wrzos C, Romanelli E, Bennett JL, Enz L, Goebels N, Nave KA, Kerschensteiner M, Schaeren-Wiemers N, Stadelmann C, Simons M (2016) Loss of Myelin Basic Protein Function Triggers Myelin Breakdown in Models of Demyelinating Diseases. Cell Rep 16:314-322.
Wheeler NA, Fuss B (2016) Extracellular cues influencing oligodendrocyte differentiation and (re)myelination. Exp Neurol.
Yeung MSY, Djelloul M, Steiner E, Bernard S, Salehpour M, Possnert G, Brundin L, Frisén J (2019) Dynamics of oligodendrocyte generation in multiple sclerosis. Nature 566:538-542.
Yona S, Kim KW, Wolf Y, Mildner A, Varol D, Breker M, Strauss-Ayali D, Viukov S, Guilliams M, Misharin A, Hume DA, Perlman H, Malissen B, Zelzer E, Jung S (2013) Fate mapping reveals origins and dynamics of monocytes and tissue macrophages under homeostasis. Immunity 38:79-91.
Zhan J, Mann T, Joost S, Behrangi N, Frank M, Kipp M (2020) The Cuprizone Model: Dos and Do Nots. Cells 9.

Zhang Y, Chen K, Sloan SA, Bennett ML, Scholze AR, O'Keeffe S, Phatnani HP, Guarnieri P, Caneda C, Ruderisch N, Deng S, Liddelow SA, Zhang C, Daneman R, Maniatis T, Barres BA, Wu JQ (2014) An RNA-sequencing transcriptome and splicing database of glia, neurons, and vascular cells of the cerebral cortex. J Neurosci 34:11929-11947.

Zirngibl M, Assinck P, Sizov A, Caprariello AV, Plemel JR (2022) Oligodendrocyte death and myelin loss in the cuprizone model: an updated overview of the intrinsic and extrinsic causes of cuprizone demyelination. Mol Neurodegener 17:34.

Ziskin JL, Nishiyama A, Rubio M, Fukaya M, Bergles DE (2007) Vesicular release of glutamate from unmyelinated axons in white matter. Nat Neurosci 10:321-330.

Zonouzi M, Scafidi J, Li P, McEllin B, Edwards J, Dupree JL, Harvey L, Sun D, Hübner CA, Cull-Candy SG, Farrant M, Gallo V (2015) GABAergic regulation of cerebellar NG2 cell development is altered in perinatal white matter injury. Nat Neurosci 18:674-682.

11 ACKNOWLEDGEMENTS

First and foremost, I would like to thank Prof. Frank Kirchhoff and Prof. Frank Schmitz for being reviewers of my thesis. Particular thanks to Frank Kirchhoff for your encouragement over all the years since my master thesis, during which I was allowed to pursue this exciting scientific question in your laboratory, and so many wonderful experiences with you and your team, also during fascinating meetings all over the world. Besides scientific discussions, there was always time for political and personal exchanges and support or legendary dancing at summer parties.

My sincere and heartfelt thanks go to Anja Scheller, who supported me over the years and always had an open ear for me and my problems, who was not only a supervisor, but what also became friendship. When you share the office for years, you either become friends or enemies and I can say that colleagues became friends, thank you Davide Gobbo for all the help, laughs and tears during the time in the lab and outside; some would say we only exist in a twin pack.

What would you be without a good team and that is what you have in the Department of Molecular Physiology in Homburg. So Wenhui Huang “Fei” makes the "boyz office" complete and you can come to him with any question, he always has a suitable answer ready, thank you very much. Thank you, Xianshu Bai “Cai” for your support, good mood and that one can always ask you for advice. Many thanks also to Emeline Buttigieg for being the second person in the team mainly fighting spinal cord research and her always open ear and friendship. My thanks also go to Lipao Fang, Qilin Guo and Qing Liu, without whom everyday life in the lab would be so gray and empty and who are always ready to help.

Of course, it is also important to thank the former colleagues and friends from the lab for their support and great times together. Thank you, my dear Erika Meyer, Laura C. Caudal, Michael Schweigmann, Gebhard Stopper, Carmen Kasakow, Laura Stopper, Luciana Politti Cartarozzi and Bogdan Cătălin; especially to Luciana and Bogdan, who introduced me to spinal cord surgeries and the two-photon microscopy.

Finally, many thanks to Ute Legler for her help in the fight with the administration and Daniel Schauenburg and his team for their great work in the animal house.

„Die Wissenschaft, richtig verstanden, heilt den Menschen von seinem Stolz; denn sie zeigt ihm seine Grenzen.“

- Albert Schweitzer

12 CURRICULUM VITAE AND LIST OF PUBLICATIONS

AUS DATENSCHUTZRECHTLICHEN GRÜNDEN WIRD DER LEBENSLAUF IN DER ELEKTRONISCHEN FASSUNG DER DISSERTATION NICHT VERÖFFENTLICHT.

PUBLICATIONS

Meyer E., **Rieder P.**, Gobbo D., Cândido G., Scheller A., de Oliveira R.M., Kirchhoff F.; Cannabidiol Exerts a Neuroprotective and Glia-Balancing Effect in the Subacute Phase of Stroke; Int J Mol Sci; 2022 Oct 25; 23(21):12886; doi: 10.3390/ijms232112886.

Stopper G., Caudal L.C., **Rieder P.**, Gobbo D., Felix L., Everaerts K., Bai X., Stopper L., Rose C.R., Scheller A. and Kirchhoff F.; Novel algorithms for improved detection and analysis of fluorescent signal fluctuations; bio$R_x$iv; 2022; https://doi.org/10.1101/2022.08.03.502593.

Rieder P.*, Gobbo D.*, Stopper G., Welle A., Damo E., Kirchhoff F. and Scheller A. (2022); Astrocytes and Microglia Exhibit Cell-Specific Ca^{2+} Signaling Dynamics in the Murine Spinal Cord; Front Mol Neurosci; 2022 Mar 30; 15:840948; doi: 10.3389/fnmol.2022.840948; eCollection 2022.

Damo E., **Rieder P.**, Coban I., Silva R.L., Kirchhoff F., Simonetti M., Agarwal A.; Glial cells as target for antidepressants in neuropathic pain; Neuroforum; 2022; https://doi.org/10.1515/nf-2021-0036.

Cartarozzi L.P., **Rieder P.**, Bai X., Scheller A., de Oliveira A.L.R., Kirchhoff F.; *In vivo* two-photon imaging of motoneurons and adjacent glia in the ventral spinal cord; J Neurosci Methods; 2018 Apr 1; 299:8-15; doi: 10.1016/j.jneumeth.2018.01.005; Epub 2018 Feb 3.

* *contributed equally*

SCHOOLS, PRESENTATIONS AND POSTERS

2019	International Astrocyte School, Bertinoro, Italy
2022	4th DAAD-CAPES Workshop, oral presentation, University of Campinas, Campinas, Brazil
2021	Closing conference FOR2289, oral presentation, Heidelberg, Germany
2019	CAPES-DAAD-COFECUB Symposium, oral presentation, University of Sao Paulo, Ribeirao Preto, Brazil
2022	3rd FALAN Congress, poster, Belem, Brazil
2021	XV European Meeting on Glial Cells in Health and Disease, poster, Marseille, France
2019	XIV European Meeting on Glial Cells in Health and Disease, poster, Porto, Portugal
2018	11th FENS Forum of Neuroscience, poster, Berlin, Germany
2017	12th Göttingen Meeting of the German Neuroscience Society, poster, Göttingen, Germany